NATIONAL TECHNICAL UNIVERSITY OF ATHENS
SCHOOL OF APPLIED SCIENCES
Department of Physics

Measurement of the ^{242}Pu(n,f) reaction cross-section at the CERN n_TOF facility

Ph.D. THESIS

A. Tsinganis

ATHENS, July 2014

"Mais sais-tu au moins ce que c'est que la matière?"
"Très bien", lui répondit l'homme. "Par example cette pierre est grise, est d'une telle forme, a ses trois dimensions, elle est pesante et divisible."
"Eh bien!" dit le Sirien, "cette chose qui te paraît être divisible, pesante, et grise, me diras-tu bien ce que c'est? Tu vois quelques attributs; mais le fond de la chose, le connais-tu?"
"Non", dit l'autre.
"Tu ne sais donc point ce que c'est que la matière."

Voltaire, "Micromégas" (1752)

'But do you at least know what matter is?'
'Certainly,' replied the man. 'For example this stone is grey, has such and such a form, has its three dimensions, it is heavy and divisible.'
'Well!' said the Sirian, 'this thing that appears to you to be divisible, heavy, and grey, will you tell me what it is? You see some attributes, but the essence of the thing, do you know what it is?'
'No,' said the other.
'So you know not what matter is.'

Acknowledgements

In his short story *'Micromégas'*, an excerpt of which is found on the previous page, Voltaire imagined two travellers from Sirius and Saturn arriving on Earth. At first, they find it to be uninhabited; their gigantic size makes it impossible for them to see the little creatures that live here. Once they overcome this obstacle by fashioning a crude microscope, they encounter a group of philosophers and scientists sailing on a ship. Surprised as they are that such small creatures are capable of speech and thought, they begin a philosophical discussion with them, a discussion touching upon the infinitely large and infinitely small, on the perception of time-scales and space, in what can be counted among the first examples of the science-fiction genre.

Voltaire, who was of these parts during his exile from Paris – his 'château' in Ferney (nowadays Ferney-Voltaire), near Geneva, lies within the great circle traced by the Large Hadron Collider under the gentle countryside of the Swiss-French border and is only about 6 kilometres away from the n_TOF Experimental Area – probably could not imagine that a 'Micromegas detector' would one day allow us to probe the interior of matter on the remarkably small scale of the atomic nucleus.

It is thanks to Voltaire and many like him – philosophers, thinkers, writers and scientists, from Copernicus and Galileo to Newton and the may others that followed – that the free pursuit of science (at least within the limits of research budgets) is taken for granted today. The impetus they provided saw humankind set out to explore the world, in the more encompassing sense of the Greek 'κόσμος'; not just this 'pale blue dot' we live and die on, but the farthest reaches of the universe and the even more inscrutable sub-atomic world.

A few centuries later, several people contributed to this particular thesis in somewhat more concrete ways. For this they are listed here, on the same pages with some of the great minds of the past.

I am indebted to **Enrico Chiaveri** and **Vasilis Vlachoudis** for making it possible for me to spend more than three years at CERN. It was Vasilis who first suggested the possibility and Enrico, as Spokesperson of the n_TOF Collaboration, who gave the final approval. It would not have been the same without the opportunity to experience the 'life' of a facility such as n_TOF over two years of operation and during the design and construction of Experimental Area II. More on these two gentlemen later.

It is not an exaggeration to say that this thesis would not be finished yet without the invaluable assistance of my colleague and friend at n_TOF, **Carlos Guerrero**. His good spirits and his expertise – especially on the quirks and peculiarities of ROOT – are only matched by his willingness to assist his colleagues despite the formidable demands on his own time.

Eric Berthoumieux was always an island of tranquillity amid the noise, but also an essential component of the n_TOF machine; take him out, and the machine stops. Working with him was not only a genuine pleasure, but it also gave me the opportunity to learn how the facility works behind the control room monitors. I express my deepest appreciation to him for his assistance in the preparation and execution of this experiment and our many useful discussions.

A non-negligible part of my time during this work was dedicated to Monte-Carlo simulations (and there is a whole chapter in this thesis to prove it). In this, **Vasilis**' availability and his guidance were invaluable. I am also able to report that a very small part of his outstanding programming skills rubbed off on me during our work together. Beyond his technical wizardry, which is complemented by a strong physics background, discussions with him on any topic whatsoever are thoroughly enjoyable and always stimulating.

Having shunned retirement to remain at the helm of the n_TOF Collaboration and successfully champion the construction of the new experimental area, **Enrico**'s unlimited drive and enthusiasm are admirable and contagious. Apart from the various n_TOF meetings around Europe, I was given the opportunity, thanks to the support which he always gladly provided, to present this work at two major conferences: the Nuclear Data conference in New York and the International Nuclear Physics Conference in Florence.

Nicola Colonna freely shared his experience and offered valuable advice at various stages of this work. Our meetings, discussions and occasional arguments (often on the n_TOF neutron beam simulations) were always helpful in understanding and clearing up some finer point. The eagerness and patience with which he approaches his role as an educator is unmatched, as is his ability to cut through convoluted arguments and highlight the essential aspects of a problem.

Marco Calviani was also on hand to offer occasional advice on the data analysis and discussions with **Arjan Plompen**, **Franz-Josef Hambsch** and **Arnd Junghans** during various ERINDA and ANDES meetings were always useful and motivating. **Nikolas Patronis'** critical reading of this thesis at the final stages was very helpful in adapting the presentation of this work to an external non-specialist audience.

Christina Weiss and I, as 'resident' n_TOF Ph.D. students for the last three years, shared many an hour in the experimental area with Carlos and Eric. We often found ourselves in improbable positions while setting up different experiments squeezed between detectors or stretching to the ceiling trying to fix some support. As she continues to work at n_TOF in the next few years, I wish her to discover a whole new world of acrobatic exercises while attempting to mount experimental setups along the vertical axis.

I should not forget **Francesco Cerutti**, with whom I did not directly collaborate on my thesis but only on a separate project a few years back. I must nevertheless thank him for his indirect encouragement and for his eternal good spirits and inimitable sense of humour which he skilfully employed to manipulate me into participating in the CERN Annual Relay Race – twice. I can only wish there had been more opportunities to work together (not necessarily including long discussions on the treatment of low-energy neutrons in FLUKA).

Plutarch's work *'Parallel lives'* contains paired biographies of 'noble Greeks and Romans'. Without any such aspirations of greatness, the 'parallel lives' of myself and **Maria Diakaki** have taken us along nearly identical paths for over ten years. Despite spending the past three of those years in different countries, we nevertheless found ourselves once again working together on theoretical cross-section calculations. In all likelihood, our next steps will take us in different directions, but I am sure we will always remember these years fondly.

Apart from those already mentioned above, I would also like to acknowledge other members of the n_TOF collaboration with whom I had the pleasure of working and socialising in the past few years: **Frank Gunsing**, **Thomas Papaevangelou**, **Francesca Belloni**, **Ignacio Duran**, **Daniel Cano-Ott**, **Peter Schillebeeckx**, **Massimo Barbagallo**, **Cristian Massimi**, **Federica Mingrone**, **Alvaro Hernandez**, **Javier Praena**, **Marta Sabaté**, **Ida Bergstrom** and many others.

To quote the Beatles – who may not inhabit the same exalted circles as the great men and women previously mentioned, but nonetheless –, all this work was done 'with a little help from my friends', even as we find ourselves scattered across Europe. Our sparse meetings and occasional Skype calls were always highlights. Not to be forgotten, friends close-by; in particular **Nikos**, for the many weekends spent together happily working on our theses (and for the various threats he made in case I did not explicitly mention him in these acknowledgements).

Finally, I must reserve a position of honour for my supervisors, Professors **Rosa Zanni-Vlastou** and **Michael Kokkoris**. Since I started working with them as an undergraduate student, I have been the recipient of their trust and appreciation. Never people to discourage initiative, they allowed me to take serious responsibilities even at those early stages. Their skill in creating a sense of loyalty – indeed, a sense of *family* – within their group is admirable, as is their perseverance in maintaining the highest standards for their work and their students even under less than ideal circumstances. Their advice and guidance will be forever remembered and appreciated, and I take great joy in the fact that, after ceasing to be my supervisors, they will remain my friends.

Many years ago, I discovered a dusted copy of my father's Ph.D. (or M.Sc.) thesis while rummaging through our library. There was little I could understand, so it is no surprise that it was a completely banal phrase from the acknowledgements page that caught my attention. It approximately read: 'I would like to thank Miss So-and-so for the fine work of typing the manuscript'. It is an immense relief that no such acknowledgement is necessary here, not least because it allows me to unequivocally state that no living being, human or otherwise – except perhaps myself –, was hurt during the preparation of this thesis.

Somewhere near Ferney-Voltaire,
June 2014

Abstract

The accurate knowledge of relevant nuclear data, such as the neutron-induced fission cross sections of various plutonium isotopes and other minor actinides, is crucial for the design of advanced nuclear systems as well as the development of comprehensive theoretical models of the fission process. The ^{242}Pu(n,f) cross section was measured at the CERN n_TOF facility taking advantage of the wide energy range and the high instantaneous flux of the neutron beam. In this work, results for the ^{242}Pu(n,f) measurement are presented along with a detailed description of the experimental setup, Monte-Carlo simulations and the analysis procedure, and a theoretical cross section calculation performed with the EMPIRE code.

Contents

Preface

This thesis presents the work performed during the 2011-2013 period on the measurement of the ^{242}Pu fission cross-section at the CERN n_TOF facility. The experimental part of this work was carried out within the framework of the ANDES [1] (*Accurate Nuclear Data for Nuclear Energy Sustainability*) project (EURATOM contract FP7-249671) and received support from the ERINDA [2] (*European Research Infrastructures for Nuclear Data*) project (EURATOM contract FP7-269499) for transnational access to experimental facilities. Apart from the ERINDA and ANDES progress meetings, preliminary results were presented at the International Conference on Nuclear Data for Science and Technology (New York, 2013) and the International Nuclear Physics Conference (Florence, 2013).

An overview of the motivation of this measurement, in the context of future nuclear reactor design, nuclear waste transmutation and basic nuclear physics research, as well as the role of plutonium in nuclear energy production and relevant nuclear data needs are given in the introduction.

The n_TOF facility is presented in Chapter 1, focusing on the aspects relevant to the measurement, such as the neutron production and the neutron beam-line. The experimental setup for this particular measurement, including samples, detectors and associated electronics and data acquisition systems is also described in this chapter.

Chapter 2 covers the extensive simulation work that was carried out, both pertaining to the detailed study of the characteristics of the n_TOF neutron beam, such as the fluence, the spatial profile and the resolution function and to the understanding of the behaviour of the Micromegas detectors used in the experiment, which was studied by simulating fission events and reconstructing the corresponding detector signals.

The entire data analysis sequence is described in detail in Chapter 3, along with the results obtained. Particular attention is given to the fission event selection and to the software developed to recover high neutron-energy data affected by the baseline oscillations occurring after the prompt γ-flash.

After an overview of the relevant theoretical background of nuclear fission, Chapter 4 covers the theoretical calculations performed with the EMPIRE nuclear reaction code and their results.

Introduction

Nuclear energy and the global energy problem

The continuous growth of the human population (Figure 1) [3], coupled with the increase in per capita energy consumption (Figure 2), especially in developing countries [4], as living standards improve, is leading to an ever more rapid increase in global energy demands. The serious environmental concerns posed by continuing reliance on fossil fuels are well known and have been highlighted once again in the recent IPCC (Intergovernmental Panel on Climate Change) assessment report [5]. Global efforts to reduce greenhouse gas emissions have yielded mixed results, but whatever gains have been made locally, most notably in Central and Northern Europe, have been offset by increased emissions from developing countries with large populations, such as China and India. The recent global financial crisis has also been detrimental to these efforts by diverting investments and public attention towards mitigating the immediate consequences of the crisis in developed countries, despite the fact that it has been shown that investment in alternative energy sources can yield considerable economic and employment benefits in the medium and long term, in addition to the obvious environmental gains both in terms of environmental protection, as well as in the reduction of the frequency and intensity of extreme weather phenomena associated with high economic costs.

In the short and medium term, the growth of the global energy demand could be met with a more efficient use of existing energy sources by balancing a phased reduction of fossil fuel consumption with increased contributions from ‘clean’ or ‘carbon-free’ energy technologies. At present, over 80% of the total primary energy supply comes from fossil fuels (oil, coal and natural gas), which also account for roughly 70% of the electricity production [6]. The rest of the electricity production is largely covered by hydro-electric (16%) and nuclear power (12%), while the contribution from other renewable energy sources, such as wind, solar, tide, geothermal energy etc. is very low (less than 5%). It is reasonable to assume that with sustained investment in research on renewable sources of energy, these will eventually contribute a larger share. It seems unlikely, however, that they will be able to cover the entire energy demand in the foreseeable future, especially when it comes to providing power for increasingly large urban agglomerations with populations of several millions or even tens of millions (67% of the population is expected to reside in urban areas by 2050, against 52% in 2011) [7], rather than smaller-scale local implementations, such as those found in countries whose population landscape, with distributed settlements of smaller size, lends itself to this kind of approach. Nuclear energy will therefore likely remain an important component in the global energy mix and the nuclear output may even have to be increased to meet

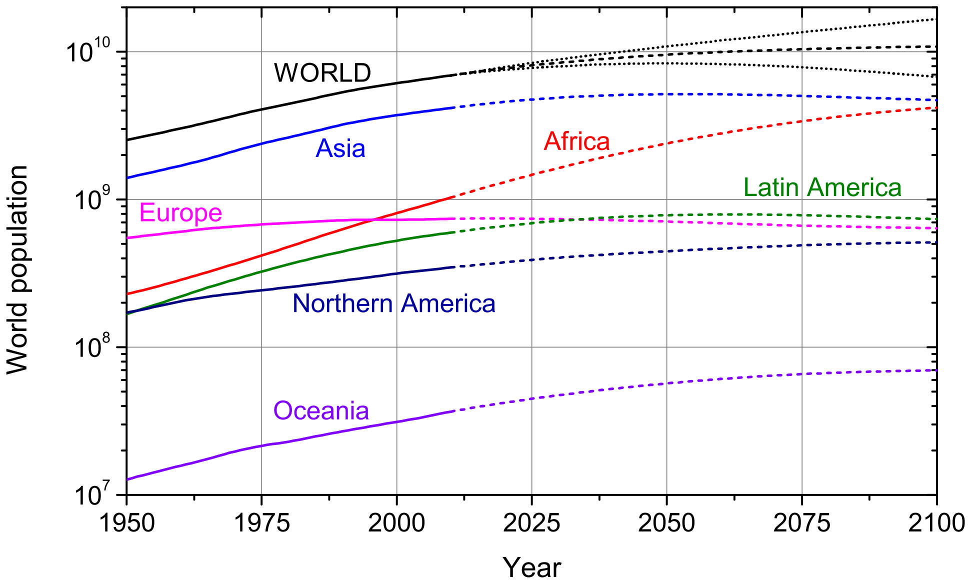

Figure 1: *Total and regional population data from 1950 to 2010. For each region, a projection of population evolution until 2100 based on a medium fertility rate estimate is also shown. For the total population, projections for the low and high end of estimated fertility rates are also included. [3]*

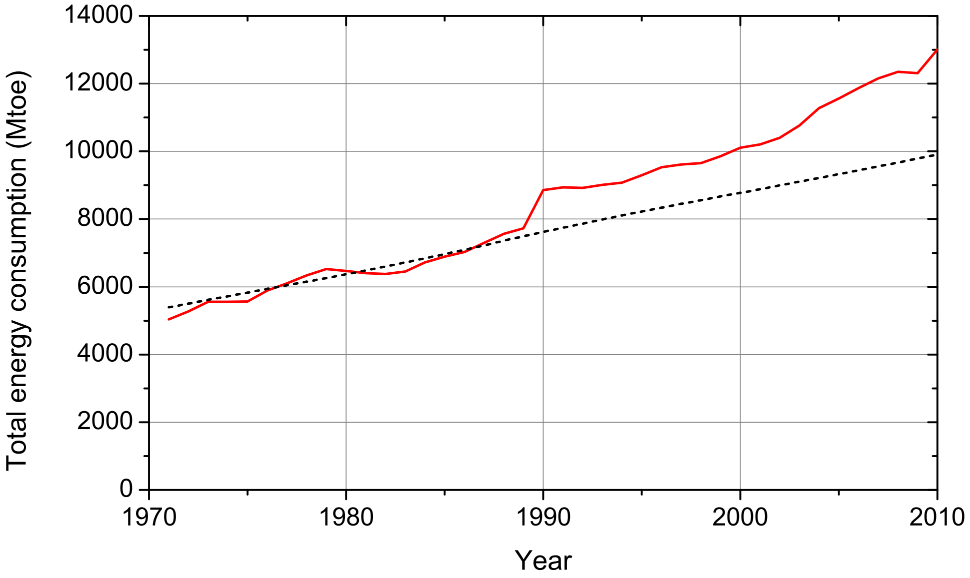

Figure 2: *Total energy consumption in Mt of oil equivalent (Mtoe) from 1971 to 2010. The dashed line shows what would have been the evolution with the per capita consumption remaining at the average of the 70s and 80s, accounting for population growth. The increase after 1990 and especially after 2000, largely driven by increased consumption in China, is evident. [4]*

the challenges of the coming decades.

There are, nevertheless, three chief concerns associated with the use of nuclear energy. These are: (i) the safety issues posed by current nuclear power plants, (ii) the long-term management of large volumes of radioactive waste and, finally, (iii) the proliferation of nuclear material and its potential use for military applications or terrorist activities. Quite naturally, highest among the concerns in the general public is the safety aspect of nuclear power plants and the fear of serious accidents with wide-spread health consequences. These concerns were exacerbated recently with the 2011 accident in Fukushima, Japan, which led countries such as Germany and Switzerland to announce a phase-out of nuclear energy in the next 10-20 years. With perhaps less urgency, but still high among environmental concerns is the question of the management and long-term storage of nuclear waste. Nuclear waste convoys have frequently been the target of protests, especially in Germany and planning of waste storage repositories are regularly met with strong opposition from neighbouring communities. The question of the proliferation of nuclear material is less prominent among public concerns, but is treated very seriously at an international level. Most recently, the high-level negotiations on the Iranian nuclear programme brought high visibility to this matter, along with ever-present concerns on undeclared nuclear activities in North Korea.

A comprehensive discussion of the social, economic and political implications of nuclear power and its public perception is well beyond the scope of this thesis. All three issues mentioned above, however, could be effectively addressed with the advanced nuclear reactor technologies presently under development.

Present and future of nuclear reactors

Of the more than 400 nuclear power plants operating today, a considerable fraction are Generation II reactors, constructed during the 1970s and 80s (Generation I reactors are the prototype reactors of the 1950s and 60s). Some Generation III reactors, featuring enhanced safety, efficiency and economics are already available, while so-called Generation III+ systems, still based on conventional designs, should be ready for near-term deployment. Despite license extensions, many of the presently operating nuclear power plants will reach the end of their life and be decommissioned around 2030. These considerations have prompted research into innovative nuclear reactor designs to replace ageing reactors and be ready for deployment by the same time, while also addressing the concerns previously mentioned.

Conventional reactors rely on the so-called ‘once through’ process. This term reflects the fact that fuel elements are only used in the reactor once before being extracted, usually after around a year or less, and stored. This process is manifestly inefficient in terms of the long-term management of uranium resources, since only a small fraction of the ^{235}U present in the fuel (which, in turn, represents only about 0.7% of natural uranium) is burned. It further results in the generation of large quantities of nuclear waste. This waste includes large quantities of fission fragments, such as ^{99}Tc, ^{93}Zr, ^{135}Cs, ^{107}Pd and ^{129}I. Fission fragments constitute the dominant contribution to the radiotoxicity of nuclear waste for the first few hundred years, before falling off considerably after several centuries. Isotopes of several transuranic elements are also present in large quantities

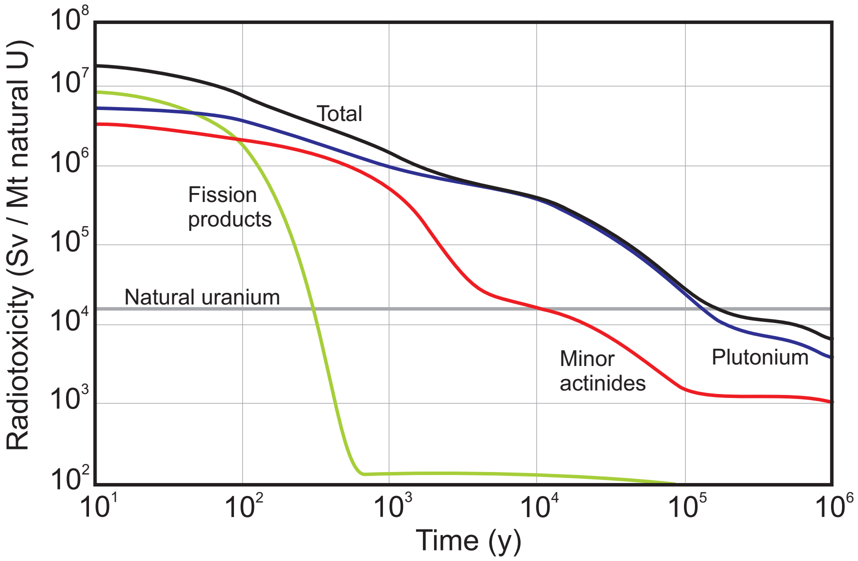

Figure 3: *Evolution of spent fuel radiotoxicity.*

in nuclear waste. They are produced inside the reactor through a sequence of neutron capture reactions and β-decays starting mainly from the ^{238}U present in the fuel and include plutonium and neptunium, americium and curium isotopes, also known as *minor actinides*. Actinides are responsible for the long-term radiotoxicity of nuclear waste which remains important for over one hundred thousand years (Figure 3). This poses an obvious problem, since no engineering solution can be expected to survive such time-scales, and makes it necessary to discover underground repositories that are not only geologically stable and will prevent release of radioactive material into the environment, but have sufficient combined capacity to accommodate the significant quantities of waste being produced by conventional reactors.

Unfortunately, all these isotopes build up in conventional thermal reactors since their rate of production is higher than their rate of transmutation. This is not only due to their long half-lives, but also to the fact that the fission cross-sections of several actinides is very low at low neutron energies and presents a threshold at a few hundred keV, as shown in Figure 4. It follows that the incineration of these isotopes, which constitute a considerable fraction of the high-radiotoxicity component of nuclear waste, requires a fast neutron spectrum to match the fission cross-sections.

It is clear, therefore, that waste transmutation by neutron-induced reactions is a most promising approach towards the reduction of the radiotoxicity of nuclear waste, both by removing plutonium and minor actinides through fission, as well as long-lived fission products through neutron capture, while also utilising the energy content of transuranic elements.

In this spirit, various solutions are being explored to replace conventional reactors. The Generation-IV International Forum (GIF) [8] was set up in 2000 to evaluate different reactor concepts and select those deemed more promising. The proposed solutions were required to meet the following broad criteria: (i) *Safety and reliability:* Generation-IV systems will minimise the probability of reactor core damage and operate safely and reliably, eliminating the need for off-site emergency response; (ii) *Sustainability:* the energy production must meet emissions standards and make sustainable use of fuel resources, while minimising waste and long-term waste management needs; (iii) *Eco-*

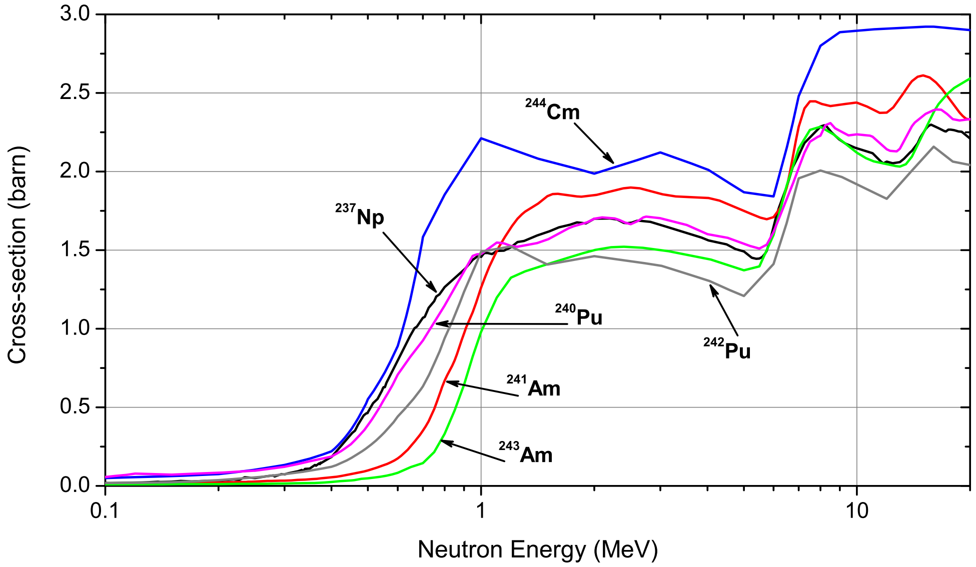

Figure 4: *Fission cross-sections of several long-lived isotopes present in nuclear waste. The fission threshold at a few hundred keV means that it is only practical to recycle these isotopes in nuclear systems with a fast neutron spectrum.*

nomics: the costs and financial risk of these systems will be comparable to or lower than other energy sources; (iv) *Non-proliferation and security:* Generation-IV systems should be inherently unattractive as sources of nuclear material for military applications and provide increased physical security against attacks.

With these guidelines in mind, six reactor technologies were selected for further study. These include: the Gas-cooled Fast Reactor (GFR), the Lead-cooled Fast Reactor (LFR), the Molten Salt Reactor (MSR), the Supercritical Water-cooled Reactor (SCWR), the Sodium-cooled Fast Reactor (SFR) and the Very High Temperature Reactor (VHTR). These include both thermal reactors with improved burn-up and thermal efficiency and fast reactors in which minor actinides could be burned and waste from present reactor could be used as fuel. Further details on each design can be found in the Generation IV 'Technology Roadmap' [9, 10].

Furthermore, some of these designs can be used to produce hydrogen, either electrolytically or thermochemically in high-temperature reactors. This could be very important if the use of hydrogen in the transport sector becomes more common. At present, transport relies almost exclusively on fossil fuels. Thus, nuclear power could further contribute to the reduction of greenhouse emissions over the next decades.

Given the different characteristics of Generation-IV reactor types and the goals they are required to meet, it is unlikely that a single design will be in a position to satisfy all requirements. For example, reducing the inventory of minor actinides accumulated in thermal reactors will require the operation of fast reactors for waste transmutation. A combination of different designs might therefore be the most efficient and sustainable solution.

Accelerator-Driven Systems (ADS) are another option presently being considered. They are sub-critical reactors coupled with an accelerator (LINAC or cyclotron) delivering continuous proton or deuteron beams (~1 GeV) on a heavy target (such as lead, which can also be used as reactor coolant) and producing neutrons by spallation that are subsequently injected into the reactor. ADS are inherently safe, since the external supply of neutrons necessary to sustain the chain reaction can be instantly cut off, eliminating the risk of criticality accidents. The fast neutron spectrum of ADS makes them suitable for incineration and transmutation of long-lived waste products. The possibility to tune the accelerator beam to provide a fast neutron spectrum that is well-matched with the fission cross-sections of minor actinides can help to maximise the transmutation rate of these isotopes in the reactor. The waste of conventional reactors could be used as fuel for ADS, with part of the electricity produced used to power the accelerator.

Apart from different reactor designs, the amount of known and estimated uranium resources, which could become a limiting factor for the long-term use of nuclear energy, make it essential to investigate alternative fuel cycles. Thorium, for example, exists in much larger quantities than uranium in nature, almost exclusively in the form of its most stable isotope ^{232}Th ($T_{1/2} = 1.40{\times}10^{10}$ y). Although it is not itself fissile, if combined with a fissile isotope, such as ^{235}U or ^{239}Pu, to maintain a chain reaction, neutron capture will lead to ^{233}Th which, through two consecutive β-decays, leads to the production of the fissile isotope ^{233}U, thus increasing the available fissile fuel resources. Due to the higher thermal neutron capture cross-section of ^{232}Th compared to ^{238}U, the production of ^{233}U in a thermal reactor is much more efficient than the production of ^{239}Pu in uranium based reactors. Furthermore, a significantly lower amount of long-lived actinides is produced as waste. Finally, the Th/U fuel cycle is inherently proliferation resistant, since the isotopes involved are not utilised for weapons production.

The need for accurate nuclear data

Feasibility, design and sensitivity studies on new generation reactors require high-accuracy cross-section data for a variety of neutron-induced reactions from thermal energies to several tens of MeV. The NEA (Nuclear Energy Agency) 'Nuclear Data High Priority Request List' [11] lists data requests from different fields, including but not limited to advanced reactor design, such as nuclear medicine, radio-protection etc., while the OECD/NEA WPEC Subgroup 26 Final Report [12] summarises the needs and target accuracies for nuclear data relevant for advanced nuclear systems. Capture and fission cross-section of isotopes involved in the Th/U fuel cycle, long-lived Pu, Np, Am and Cm isotopes, long-lived fission fragments relevant for transmutation projects or isotopes considered as structural material for advanced reactors are included. Improved knowledge of these cross-sections is not only important for the design of advanced systems, but also for the operation of existing reactors, since safety margins can be more accurately defined, allowing for a more efficient use of available fuel resources.

Wide collections of experimental neutron cross-section data are available in the EXFOR database [13, 14]. Experimental data are thoroughly examined and combined with nuclear model calculations to produce evaluated cross-section libraries, such as ENDF (Evaluated Nuclear Data File) [15, 16], JEFF (Joint Evaluated Fission and Fusion File) [17], JENDL (Japanese Evaluated Nuclear Data Library) [18], BROND (Russian Evaluated Neutron Reaction Data Library) [19] and CENDL (Chinese Evaluated Nuclear Data Library) [20]. Evaluated libraries also contain information on the accuracy of the provided cross-sections, which depends on the reliability and the uncertainties of the experimental results. The present knowledge of relevant cross-sections still falls

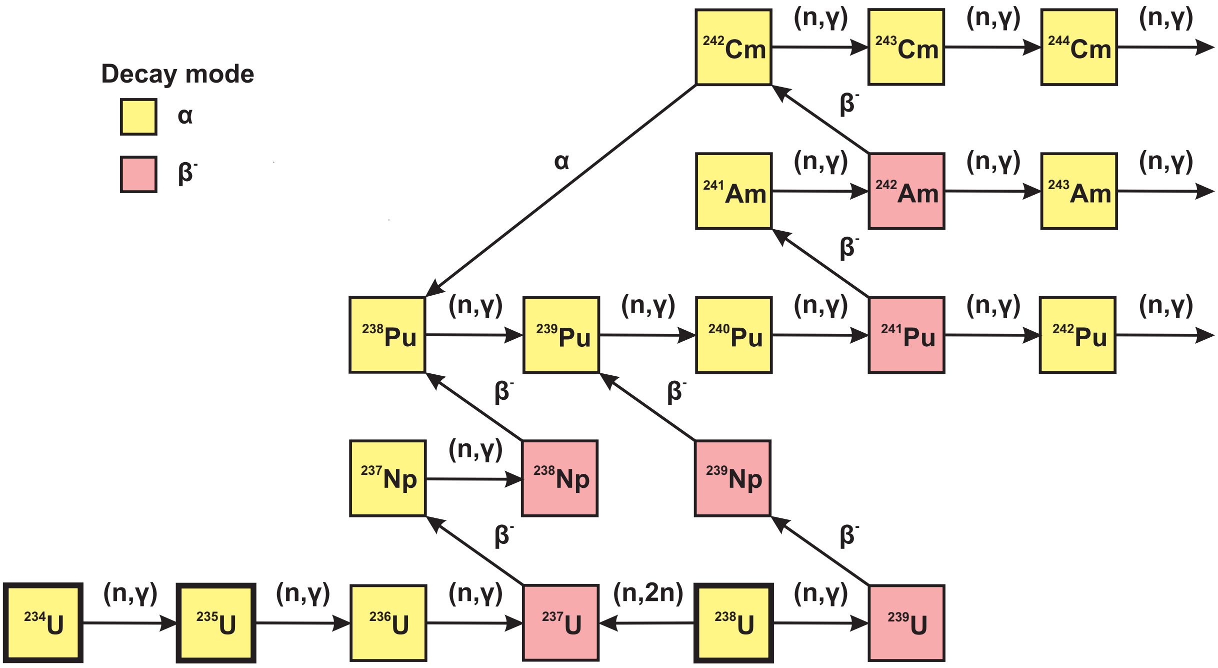

Figure 5: *Production of plutonium isotopes in a nuclear reactor, starting from the uranium fuel that contains* ^{234}*U,* ^{235}*U and* ^{238}*U, the only naturally occurring uranium isotopes. Neutron capture and successive* β*-decays in* ^{238}*U lead to the production of* ^{239}*Pu and the heavier plutonium isotopes through consecutive neutron capture reactions. The paths to the production of* ^{238}*Pu are also shown.*

short of the requirements for the design and operation of advanced nuclear systems, highlighting the need for further reduction of uncertainties.

Plutonium in nuclear reactors

Plutonium is created in conventional nuclear reactors as a by-product. Since nuclear fuel consists of 96% ^{238}U, the most common plutonium isotope produced in the reactor core is ^{239}Pu through neutron capture in ^{238}U and successive β-decays (see figure 5). The fission cross-section of ^{239}Pu is very similar to ^{235}U. It is therefore also fissile and has roughly the same energy yield as ^{235}U. More than half of the plutonium created in the reactor is 'burned', contributing about one third of the total energy output of a fuel load in a conventional Light Water Reactor. Through successive neutron capture reactions, higher mass isotopes of plutonium are built up in the reactor, starting with ^{240}Pu. Since it is not fissile and it has a half-life of 6561 years, ^{240}Pu builds up in the reactor, as does ^{242}Pu ($T_{1/2} = 3.75 \times 10^5$ y). As shown in figure 5, ^{238}Pu is also produced in the reactor. The decay heat of ^{238}Pu – that has a comparatively short half-life (87.7 y) –, ^{240}Pu and ^{242}Pu contributes to the output of the reactor.

Approximately 28 kg of plutonium are produced in a conventional thermal reactor per TWhe (Tera-Watt hour electrical) [21], or about 245 kg per year. Plutonium constitutes roughly 1.5% of the spent fuel removed at the end of the cycle. More than half is ^{239}Pu, along with about 25% ^{240}Pu, 15% ^{241}Pu, 5% of ^{242}Pu and 2% of ^{238}Pu. This significant quantity of plutonium could be used as fuel to take advantage of its energy content, rather than be treated as waste. Mixed Oxide (MOX) fuel is already produced by mixing recovered plutonium oxide with depleted uranium oxide and is used in several reactors, most notably in France. Obviously, since a large fraction of the extracted plutonium is in the form of non-fissile, but fissionable isotopes, this could happen more efficiently in a fast reactor.

Nuclear fission and basic nuclear physics

Despite the fact that over 70 years have passed since the discovery of fission (see Chapter 4), it has still not been possible to formulate a comprehensive model of the phenomenon that accurately describes all its aspects and has satisfactory predictive capabilities. The complexity of fission, with the interplay both of collective effects in the nucleus and single-particle interactions, is the main difficulty that needs to be overcome, as is often the case in theoretical nuclear physics. Indeed, as will be shown in Sections 4.1.2 and 4.1.3, a combination of a macroscopic and microscopic view of the nucleus seems to be the only reasonable approach to the problem. To this day, however, theoretical calculations cannot be relied upon to accurately predict unknown fission cross-sections. Besides possible future applications in the field of nuclear energy, data on fission cross-sections – especially neutron-induced fission – are therefore essential for the development of nuclear models and fundamental research in nuclear physics.

Neutron-induced fission cross-section measurements, however, are not always straightforward. They often involve highly-radioactive samples that induce high backgrounds in the detectors, apart from making their handling more complicated. Furthermore, most traditional neutron sources produce neutrons in limited energy ranges or with low energy resolution making the study of the cross-sections over a very wide energy range difficult to achieve. White neutron sources, where neutrons are produced as secondary particles through spallation or other high-energy interactions in a high-Z material and their energy determined with the time-of-flight technique generally offer a wider neutron spectrum and better energy resolution, although this is often at the expense of the neutron flux.

For these reasons, measuring these cross-section at different facilities, using different detection systems and reference reactions is essential to achieve an accurate knowledge of these quantities and eliminating systematic uncertainties. Within the previously mentioned ANDES project, the measurement of the ^{240,242}Pu(n,f) cross-sections was planned at three different facilities, with different detectors and reference reactions. The outcome of the ANDES project [22] highlighted the experimental difficulties involved in such measurements [23].

The n_TOF facility at CERN was one of the facilities cited above, and this thesis describes the measurement performed there.

Chapter 1

Experimental setup

The experimental work presented in this thesis was carried out at the CERN n_TOF facility, which is described in its most relevant aspects, such as the production of neutrons and the neutron beam-line, in the first part of this chapter. The fission measurement was carried out with Micromegas detectors. The second part of this chapter covers their principle of operation and main characteristics, along with a description of the samples utilised in the experiment and the associated electronics and data acquisition system.

1.1 The n_TOF facility

Between 1996 and 1997, an experimental campaign took place at CERN within the research programme on the Energy Amplifier [24, 25], a sub-critical fast neutron system driven by a proton accelerator. Among the main goals of the TARC (Transmutation by Adiabatic Resonance Crossing) experiment [26,27] was to demonstrate the feasibility of using Adiabatic Resonance Crossing (ARC) [28] as a means to destroy long-lived fission fragments in Accelerator Driven Systems (ADS), such as the Energy Amplifier. The experience accumulated, particularly with regard to the improved understanding of the physics and performance of a source of spallation neutrons based on a high-energy proton beam and a high-Z target, led to the proposal for the *n_TOF (**N**eutron **T**ime-**O**f-**F**light)* facility at CERN [29–32] with the aim of measuring neutron cross-sections over a wide energy range, from thermal to GeV, with a very high energy resolution and high instantaneous neutron flux. The facility, which comprises an approximately 185 m neutron flight-path, was finally commissioned and became operational in 2001.

The experimental programme at n_TOF has focused mainly on the study of radiative neutron capture reactions, which are of great interest to nuclear astrophysics, and neutron-induced fission reactions, which are of relevance to the development of new systems for nuclear energy production and the treatment of existing nuclear waste. The characteristics of the facility, coupled with a wide array of detection systems, allow measurements of low-mass and/or radioactive samples of interest in these fields and others, such as basic nuclear physics and nuclear medicine. The commissioning in the second half of 2014 of a new 20 m flight-path will allow n_TOF to expand its measurement capabilities to even more exotic and rare isotopes in a new experimental area much closer to the neutron source, taking advantage of the increased neutron

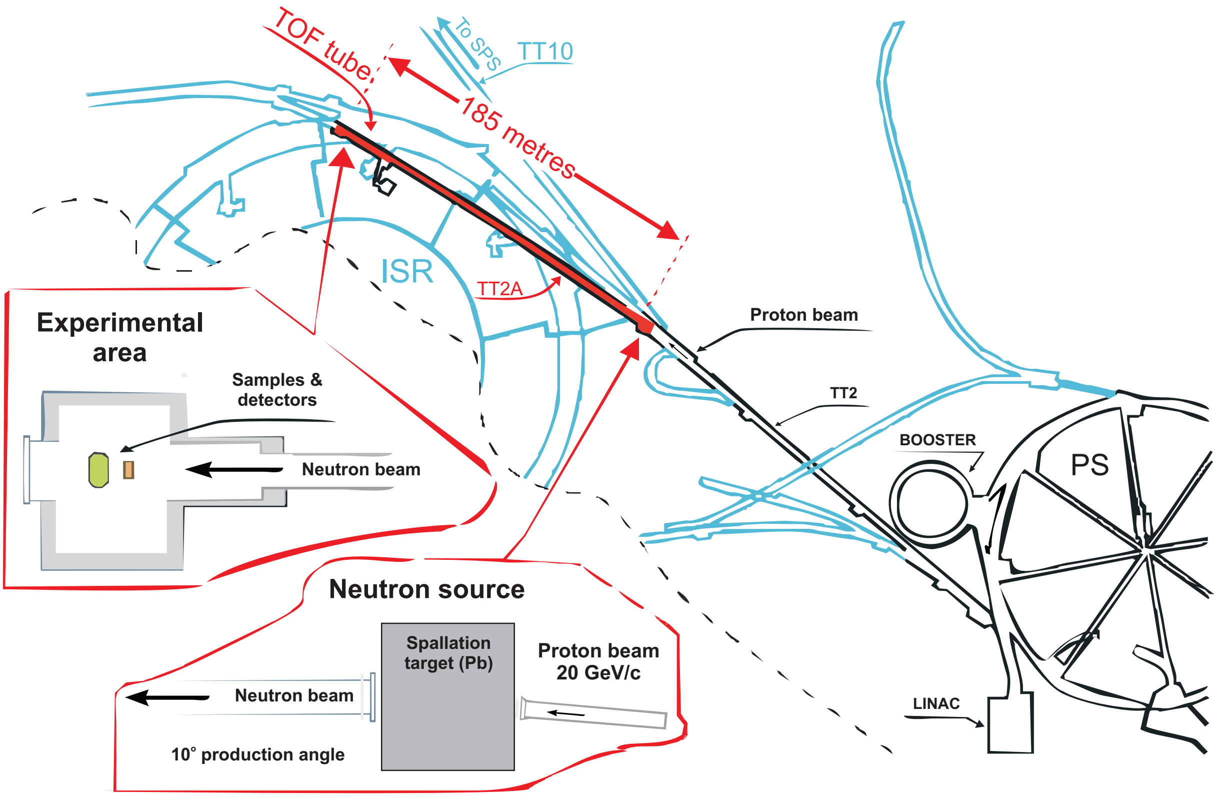

Figure 1.1: *A partial schematic view of the CERN accelerator complex, from the first stages of proton acceleration in the LINAC (Linear Accelerator), to the PS (Proton-Synchrotron) accelerator, from which n_TOF receives its beam. The position and general layout of the target and experimental area is also shown.*

fluence [33].

1.1.1 Neutron production and moderation

Neutrons at n_TOF are spallation products created by a bunched proton beam impinging on a lead target. The 20 GeV/c protons are delivered by CERN's PS (Proton-Synchrotron) accelerator in bunches with a nominal intensity of $\sim 7 \times 10^{12}$ protons (*'TOF'* or *dedicated* pulses), along with additional bunches with a lower intensity of $\sim 3 \times 10^{12}$ protons (*'EASTC'* or *parasitic* pulses). The proton bunches have a width of 7 ns (r.m.s.), which becomes significant when analysing high-energy-neutron data, as will be shown later. The frequency of the bunches does not exceed 0.8 Hz (1.2 s between consecutive bunches) and varies depending on beam requests by other experiments running simultaneously at CERN, while also respecting the defined limit for power delivered on target. This, in turn, ensures that there is no overlap between consecutive neutron bunches. Since the particle shower initiated by the proton beam in the lead target is strongly forward-peaked, the proton beam is delivered on the target at an angle of 10° with respect to the neutron beam line axis in order to prevent the bulk of these secondary particles (protons, photons, muons, pions etc.) from entering the neutron beam tube and reaching the experimental area. The general layout of the facility is shown in figure 1.1.

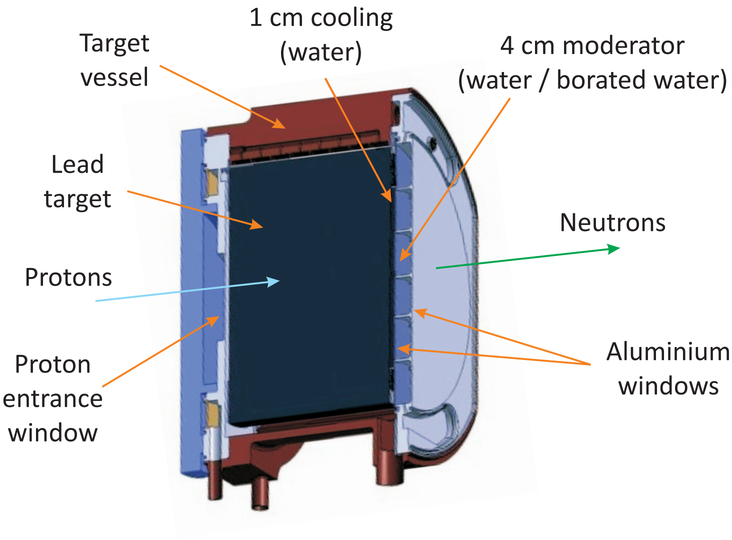

Figure 1.2: *A cross-section of the n_TOF target. The direction of the proton and neutron beam is indicated, as well as the cooling and moderator layers. The corresponding aluminium windows after the target are also visible.*

The target itself is a lead cylinder 40 cm in length and 60 cm in diameter. A 1 cm-thick layer of water surrounds the target and is constantly circulated in order to cool it down. Along the direction of the beam, this layer is immediately followed by a second, 4 cm-thick layer which is occupied either by demineralised water or borated water, with the addition of a 1.28% mass fraction of boric acid (H_3BO_3, enriched in ^{10}B). Figure 1.2 shows a cross-section of the n_TOF target and the cooling and moderation layers.

Apart from the need to dissipate the heat produced inside the target due to the energy deposition by the proton beam, the water present around the target, particularly in the beam direction, serves to moderate the neutrons produced in the spallation process. The initial spallation neutron spectrum is generally a hard one, dominated by the evaporation of excited target nuclei; moderation is therefore required to widen the spectrum and cover energies down to the thermal point. For this reason, a second moderator layer is added to the one that also serves as a coolant. The two choices of moderator (water or borated water) strongly affect both the low energy neutron spectrum and the in-beam photon background. In particular, the presence of ^{10}B, which has a very large neutron capture cross-section at low energies, greatly increases the probability of the capture of low energy neutrons, thus suppressing the thermal peak in the neutron spectrum, while at the same time reducing the probability of ^{1}H(n,γ) reactions in the water, which lead to a strong production of 2.2 MeV γ-rays that constitute an undesirable background to the measurements, especially those performed with photon-sensitive detectors.

Figure 1.3 shows the n_TOF neutron beam fluence, as measured with the two moderator setups and expressed in isolethargic units (see Appendix A). The question of the in-beam photon background and how it is affected by the choice of moderator is discussed in greater detail in Section 2.2.6.

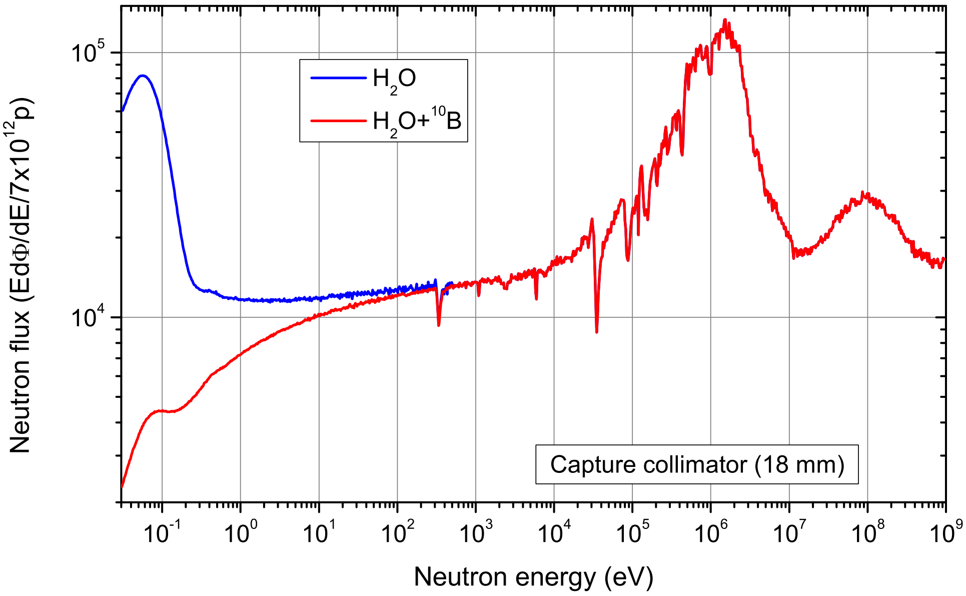

Figure 1.3: *The experimentally determined n_TOF neutron beam fluence for the two different choices of moderator. The strong suppression of the thermal peak when using borated water is evident. Above about 1 keV the neutron spectrum remains practically unchanged.*

1.1.2 The n_TOF beam-line and Experimental Area I

Once neutrons enter the vacuum tube, they begin the approximately 185 m long path to the experimental area. The beam-line consists of several sections of stainless steel tubes with progressively reduced diameters, starting with 80 cm and continuing to 60, 40 and 20 cm, and is kept at a pressure of approximately 10^{-2} mbar. The layout of the entire beam-line, showing the position of the most important elements, is illustrated in figure 1.4.

A dipole magnet, located at roughly 145 m along the beam-line, is in place to deflect the charged particles travelling with the neutrons inside the vacuum tube, thus preventing them from reaching the experimental area. Additional layers of shielding made of concrete and iron and covering the entire cross-section of the tunnel are in place to stop other (charged) particles originating from the target and travelling outside the beam tube. In particular, the thick iron shielding located near the sweeping magnet was added to significantly reduce the flux of muons that were found to induce a considerable neutron background in the experimental area through μ^- capture [34, 35].

Two collimators are installed in the beam-line. The first collimator, located at around 137 m, has an inner diameter of 11 cm and is composed of a 1 m-thick layer of iron, followed by a concrete layer of the same thickness. The second collimator shapes the neutron beam right before it enters the experimental area, at around 175 m. Two different configurations are available for the second collimator. For capture cross-section measurements, where a narrow, well defined beam is required, the inner diameter of the collimator is 1.8 cm and is composed of a 2.35 m layer of iron followed by a 50 cm layer of borated polyethylene (5% ^{10}B). For fission measurements, which generally employ very thin and, therefore, wider targets, an inner diameter of 8 cm is used, while the collimator is composed of 50 cm of borated polyethylene, 1.25 m of iron and another 75 cm of borated polyethylene. Although a fission cross-section measurement,

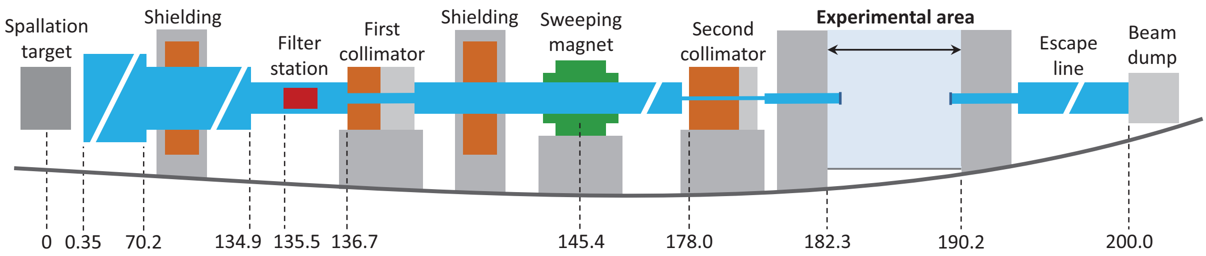

Figure 1.4: *Schematic view of the n_TOF neutron beam-line. The position of specific elements is given in metres from the spallation target. The beam-line was installed in an existing tunnel, hence the peculiar inclination of the tunnel and the need for a false floor in the experimental area. (Drawing not to scale.)*

the foreseen duration of the present experiment made it necessary to carry it out in parallel with several other capture measurements. It was therefore performed using the 'capture' setup, taking advantage of the fact that the samples were in fact only 3 cm in diameter, as described in Section 1.2.2.

The experimental area (designated as Experimental Area I, or EAR-1, since a second area is to be commissioned in the near future) is located about 185 m downstream of the spallation target and has a length of approximately 8 m. The configuration of vacuum tubes, detectors and associated electronics can be adapted to the needs of each measurement. Since 2009, the experimental area meets the requirements to operate as a Type A Work Sector [36], meaning unsealed radioactive samples can be handled, as was the case for the plutonium samples used in this work.

After exiting the experimental area, the neutron tube proceeds for a few additional metres up to the beam dump, which is located at around 200 m from the spallation target. The dump is roughly cubical with an approximately 50 cm edge and consists of a polyethylene block with cadmium foils and additional polyethylene slabs on each side and is so designed in order to minimise neutron backscattering towards the experimental area. The bulk of the data acquisition system (digitisers etc.) is also located in this area.

Figure 1.5 shows the layout of the last 30 m of the n_TOF beam-line and the access route to enter the experimental area as extracted from technical drawings of the facility.

1.1.3 Neutron energy and the time-of-flight technique

Since neutrons obviously cannot be accelerated to a specific desired energy, determining their energy is not as straightforward as in the case of charged particle beams. At n_TOF, where the neutron spectrum covers over 10 orders of magnitude in energy, the energy of the neutrons is determined by means of the *time-of-flight technique*. In general, time-of-flight measurements make use of the time a particle employs to cover a known distance after its creation to determine its energy. The technique obviously entails the use of a pulsed beam to allow for the correlation between a detected event and a specific beam bunch, thus determining the time of creation of the particle. At n_TOF, the time-of-flight technique is used to calculate the energy of a neutron that caused a particular detected event, based on the measured time-of-flight (*Tof*) of the neutron, specifically

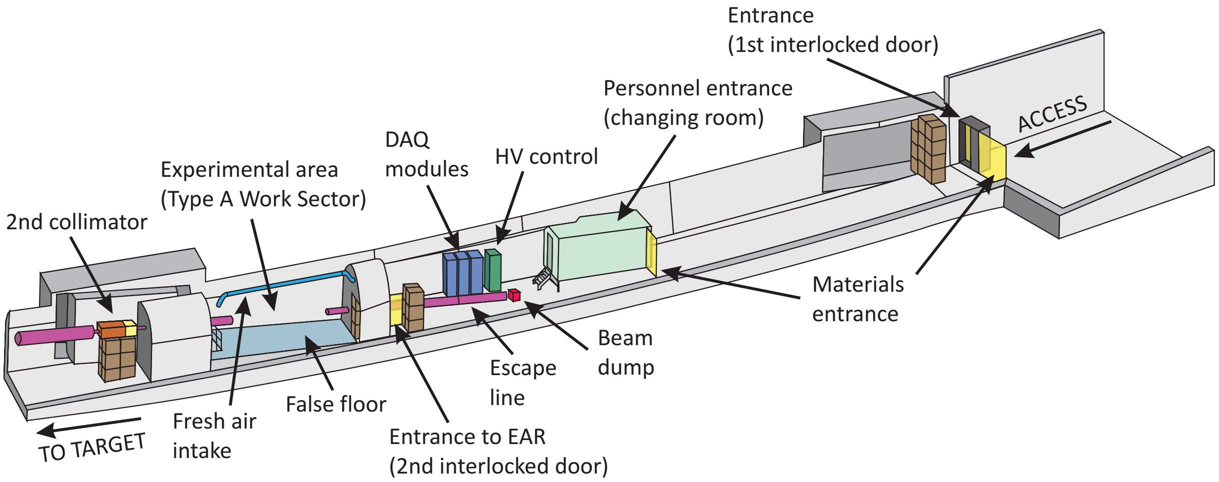

Figure 1.5: *A more detailed view of the n_TOF facility showing the last part of the n_TOF beamline, from the second collimator to the beam dump, as well as the access route. The experimental area is accessed through two doors interlocked with the beam. The detection systems and vacuum tubes inside the EAR are configurable to suit the needs of each measurement.*

the time between the production of the neutron inside the spallation target and the time of detection of the event. Put simply, this relation can be expressed in classical terms as:

$$E_n = \frac{1}{2}mv^2 = \frac{1}{2}m\left(\frac{L}{t}\right)^2 \tag{1.1}$$

In reality, however, the relation between energy and time-of-flight is not unambiguous, because the geometrical distance between the target and experimental area is not the only relevant quantity, as assumed in the simplified expression above. The unknown path (and the corresponding time) travelled by the neutron inside the materials it encounters, such as the target, the various windows, the moderator and air between the moderator window and vacuum tube will delay the neutron and increase the measured time-of-flight, thus leading to an underestimation of its energy. The length of this path is called the *moderation length* of the neutron. While the moderation length and the corresponding moderation time are experimental unknowns, it is possible to obtain the moderation time of each neutron from simulations as the time elapsed between the primary proton hitting the spallation target and the corresponding neutron reaching the scoring plane at the entrance of the vacuum tube (see Section 2.2). Given the energy and moderation time t_{mod} of each neutron, we can calculate an *effective moderation length* λ (which is obviously not the *real* distance travelled by the neutron in the material, hence the term 'effective') as the product of the moderation time and the neutron speed (appropriately derived from the energy):

$$\lambda(E_n) = v \cdot t_{mod} \tag{1.2}$$

In addition to the neutron moderation, the time-spread of the proton bunch (7 ns r.m.s.) also induces an uncertainty in the timing of detected events. Although it can be treated separately, it can be conveniently included in the moderation time used to calculate the effective moderation length.

With the information on the behaviour of λ throughout the entire neutron energy range at hand, two different methods are used to extract the neutron energy from the measured time-of-flight. One is to treat the moderation process as an equivalent time offset calculated from the $\lambda(E_n)$ curve (as opposed to an equivalent moderation length), and the other is to use the $\lambda(E_n)$ data in an iterative process.

The first method is described in detail in Lorusso et al. [37]. A brief summary is given here, using values from the present setup.

Starting with eq. 1.1, the neutron energy can be given classically as:

$$E_n = \frac{1}{2}m\left(\frac{L_{eff}}{t}\right)^2 \tag{1.3}$$

where L_{eff} is the effective flight path, which can be expressed as the sum of the geometrical length L_{geom} and the moderation length as:

$$L_{eff} = L_{geom} + \lambda(E_n) \tag{1.4}$$

A fit of the effective moderation length data is performed in the range 10 eV-10 keV, where its behaviour can be assumed to follow $E_n^{-1/2}$, finally giving:

$$\lambda = a\sqrt{E_n} \tag{1.5}$$

where a is the fitting parameter. Combining equations 1.3 and 1.5 we can estimate the t_0 offset that is equivalent to a moderation length λ:

$$E_n = \frac{1}{2}m\left(\frac{L+\lambda}{t-t_0}\right)^2 \Leftrightarrow \sqrt{\frac{2E_n}{m}} = \frac{L+\lambda}{t-t_0} \Leftrightarrow \sqrt{\frac{2E_n}{m}}t - \sqrt{\frac{2E_n}{m}}t_0 = L+\lambda \Rightarrow \lambda = -\sqrt{\frac{2E_n}{m}}t_0 \tag{1.6}$$

Comparing equations 1.5 and 1.6, the t_0 value can be determined. It should be noted that, in reality, t_0 is also a function of energy, like the moderation length. Nevertheless, the treatment of t_0 as a constant is valid within the energy range in which these calculations were made, namely where the moderation length can be expressed analytically as $\propto E_n^{-1/2}$. In addition to this, the dips in the moderation length curve are not accounted for with this fit, thus leading to less reliable results at those particular energies.

Outside this energy region, and especially at higher neutron energies, the problem cannot be expressed in simple analytical terms and an iterative procedure must be adopted, as mentioned earlier. Starting again from equation 1.1, a first approximation of the neutron energy can be obtained by using the measured time-of-flight and the geometrical distance L_{geom}:

$$E_0 = \frac{1}{2}m\left(\frac{L_{geom}}{t}\right)^2 \tag{1.7}$$

The effective flight path L_{eff} can again be expressed as the sum of the geometrical distance L_{geom} and the moderation length λ (eq. 1.4). Therefore, each consecutive approximation of the energy (given the $\lambda(E_n)$ relation) is given by:

$$E_k = \frac{1}{2} m \left(\frac{L_{geom} + \lambda(E_{k-1})}{t} \right)^2 \tag{1.8}$$

or, using the corresponding relativistic formulae for the (kinetic) energy:

$$\begin{aligned} E_k &= (\gamma_k - 1) mc^2 \\ \gamma_k &= \frac{1}{\sqrt{1 - \beta_k^2}} \\ \beta_k &= \frac{L_{geom} + \lambda(E_{k-1})}{tc} \end{aligned} \tag{1.9}$$

This algorithm converges very quickly; 2-3 iterations are typically sufficient.

1.2 The fission measurements setup

1.2.1 The Micromegas detector

The measurements for this work were performed with the use of *Micromegas* (***Micro**-**ME**sh **GA**seous **S**tructure*) detectors [38, 39]. The Micromegas belongs to the relatively new category of *Micro-Pattern Gas Detectors* (MPGD) [40–43], which has known significant development over the past two decades. MPGDs are a family of gas proportional counters that feature very narrow anode-cathode gaps and high granularity along with excellent time resolution. These characteristics make them ideal choices for particle tracking applications and for experiments where handling high count-rates is critical.

The most notable design variation of the Micromegas compared to a more traditional parallel plate avalanche chamber, which features a single gas volume between the anode and cathode, is the separation of the gas volume into two regions: a *drift region* whose width can vary from a few hundreds of μm to a few cm and an *amplification region*, typically of a few tens of μm (see figure 1.6). The two regions are separated by a *micromesh*. The micromesh is a thin (~5 μm) conductive layer with 35 μm diameter holes on its surface at a distance of 50 μm from each other, although these values may slightly vary.

An ionising particle entering the detector deposits energy mainly in the drift region, which is much larger, ionising atoms of the gas and creating electron-ion pairs. A weak electrical field of the order of 1 kV/cm is applied to this region which causes the electrons to drift towards the micromesh but is not strong enough to allow the formation of avalanches. In the amplification region, where a much higher field of around 50 kV/cm is present, avalanches form leading to a multiplication of the electrons. The amplification that takes place in the amplification region significantly improves the signal-to-noise ratio of the detector. Finally, the charge is collected in the anode and the induced signal is read-out.

The electrical field in both the drift and amplification gaps is homogeneous. The large ratio between the field in the two regions, however, causes the electrical field lines to be highly compressed and exhibit a funnel-like shape near the micromesh holes [44,45], as

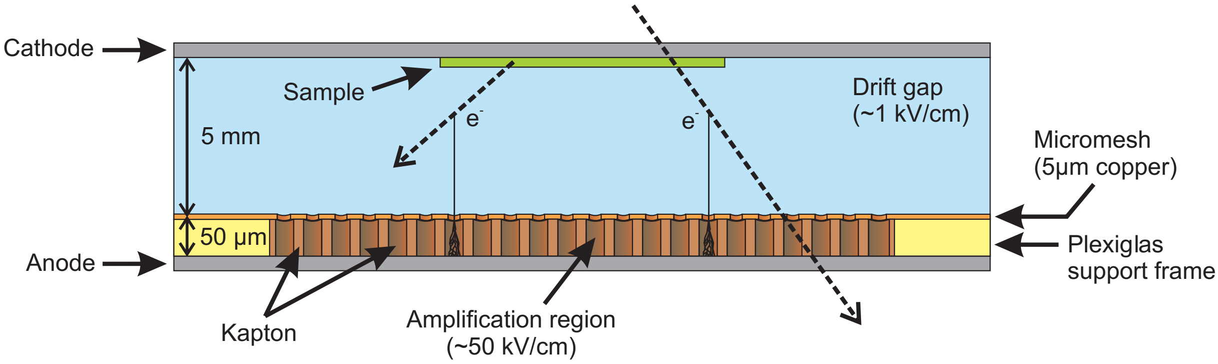

Figure 1.6: *An illustration of the basic principle of operation of a Micromegas detector. An ionising particle either entering the detector or emitted from a sample ionises the gas. The ionisation electrons drift towards the micromesh and are multiplied inside the amplification region before being finally collected in the anode. Indicative values are given for the electrical field strength values and dimensions of the two regions. (Drawing not to scale.)*

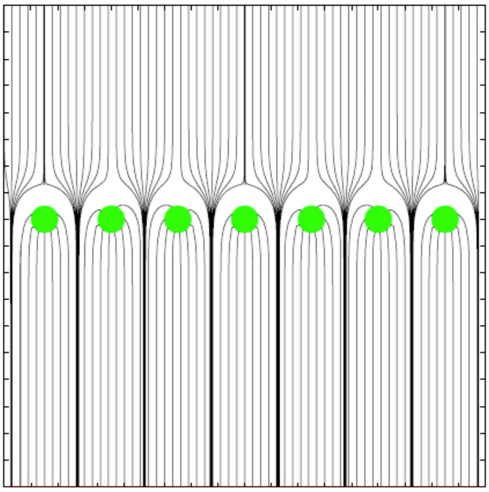

Figure 1.7: *A simulation of the electrical field near the micromesh [45]. Field lines in the drift region (top half) focus electrons towards the centre of the holes. Positive ions in the amplification region (bottom half) are carried towards the micromesh and captured.*

shown in figure 1.7. The intensity of this effect is proportional to the ratio between the field strengths in the two regions and causes the micromesh to be largely transparent to the drifting electrons for ratios greater than 5-20, depending on the characteristics of the specific micromesh. At the same time, this field configuration also ensures that the bulk of the positive ions created during the avalanche process in the amplification region are quickly collected by the micromesh and are not allowed to enter the drift region, since most or all of the electrical field lines in this region terminate on the micromesh.

Different variants based on the Micromegas concept have been produced over the last several years to cover different applications. With the segmentation of the anode into strips or pads, for example, a spatial resolution of 10-20 µm can be obtained. Such configurations are employed extensively in high-energy particle physics experiments. With the appropriate choice of gain, Micromegas detectors can also be efficiently used as photon detectors with a very satisfactory energy resolution.

For neutron measurements, it is of particular importance to minimise the amount of

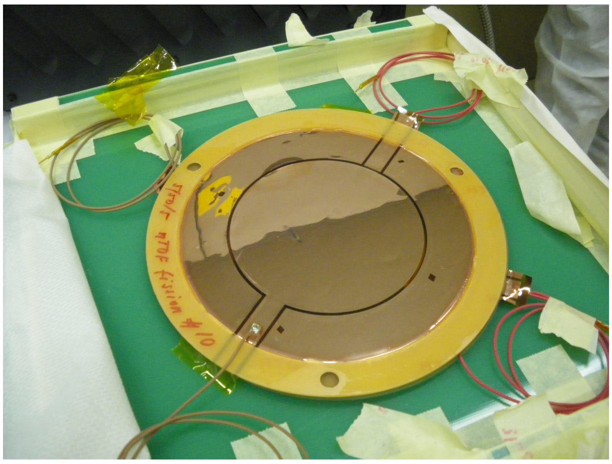

Figure 1.8: Photograph of one of the microbulk detectors used in the experiment before being mounted inside the detector chamber.

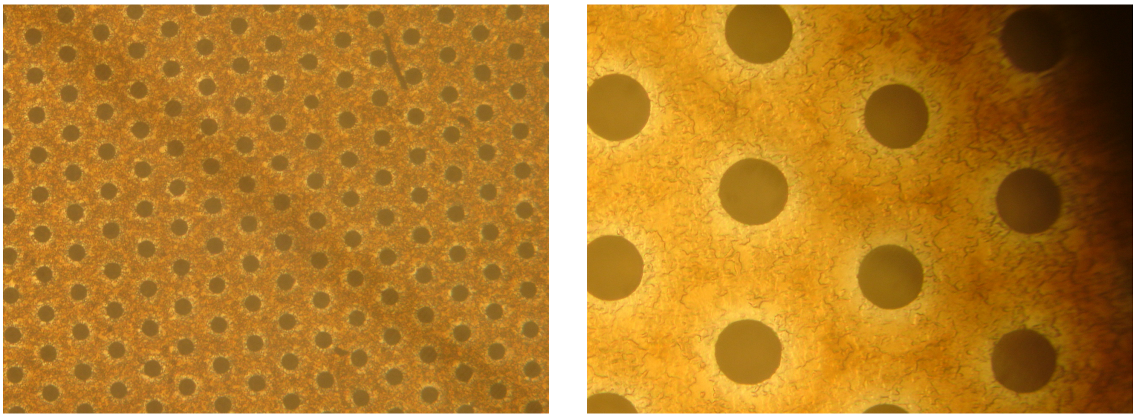

Figure 1.9: Two photographs of a micromesh obtained with an electronic microscope at different levels of magnification. The holes have a diameter of 35 μm and are placed at a distance of 50 μm from each other. (Courtesy: A. Teixeira, CERN)

material present in the beam in order to avoid the creation of background neutrons that disturb the neutron flux and lead to the production of additional secondary particles, mainly γ-rays which are an undesirable background especially for capture measurements. With the minimisation of these effects in mind, the *microbulk* design [46, 47] was developed. This design was utilised in the present experiment as well as in other measurements performed at n_TOF, including monitoring of the neutron fluence. Microbulk detectors are composed of very thin layers of material thus minimising neutron scattering. A photograph of such a detector is shown in figure 1.8, while a more detailed view of the micromesh of a microbulk detector can be seen in figure 1.9.

A stainless steel chamber capable of holding up to 10 sample-detector modules was constructed and used to house the plutonium samples and the reference ^{235}U sample. An internal support frame is in place to mount the sample holders and detectors. The cylindrical chamber is placed along the beam-line and its axis is aligned to the neutron beam. The entrance and exit windows are made of 25 μm-thick kapton and have a diameter of 15 cm, well above the neutron beam diameter for either collimator configuration. Appropriate air-tight connectors are installed to apply the necessary high-voltages and to read the output signals. A schematic of the chamber and its internal

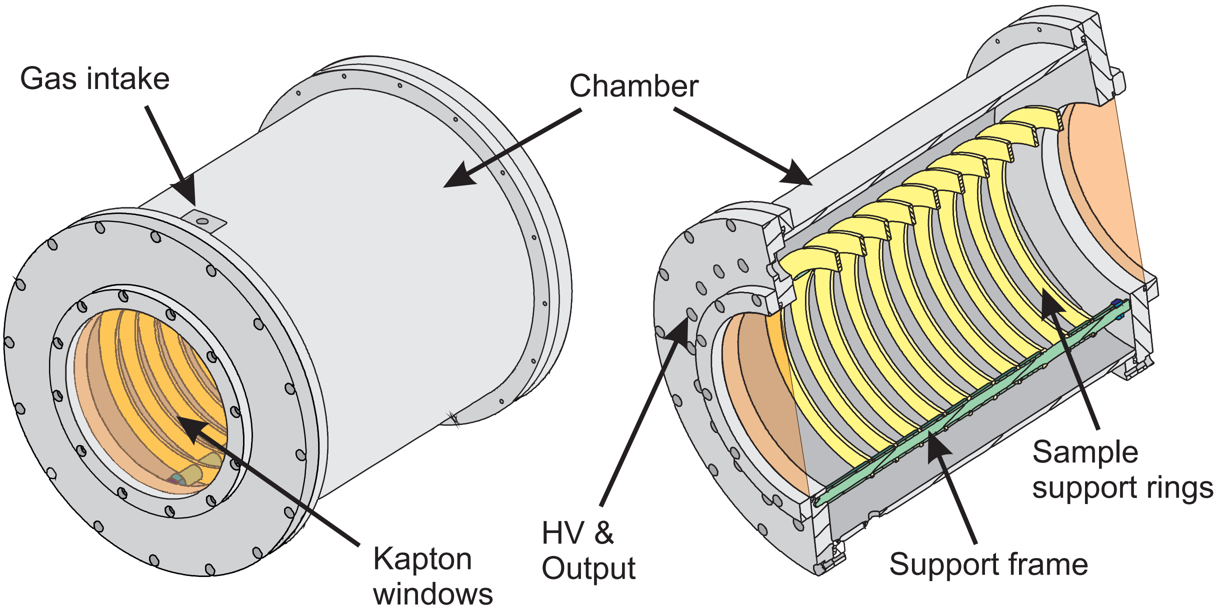

Figure 1.10: *An exterior (left) and interior (right) schematic view of the detector chamber. Samples and detectors are mounted on a support frame. The entrance and exit windows are made of kapton (25 µm) and are 15 cm in diameter.*

structure is shown in figure 1.10.

The detectors used in this experiment had an amplification gap of 50 µm. The high-voltage values were optimised over the first few days of the experiment in order to minimize the number of sparks and subsequent trips. This was important to avoid damage to the detectors and electronics and, furthermore, given the very long duration of the experiment, which ran on a 24-hour basis for several months, it was advisable to reduce the number of interventions required by shifters due to loss of voltage to the detectors as much as possible. Finally, a drift voltage of 500 V and a micromesh voltage of 250 V were applied to the detectors, leading to electrical field values of 0.5 kV/cm for the drift region and 50 kV/cm for the amplification region (a ratio of 100-to-1).

The detector was operated with an $Ar{:}CF_4{:}isoC_4H_{10}$ gas mixture (88:10:2). Isobutane has a Lower Flammability Limit (LFL)[1] of 1.8% in air (25 °C, 1 bar) [48], which is why its concentration is kept relatively low. The gas was constantly circulated and the outflow was filtered to prevent and detect any exit of radioactive products. The characteristics of the gas with respect to the electron drift velocity are discussed in more detail in Section 2.3.2.

1.2.2 Samples and sample holders

Eight plutonium oxide (PuO_2) samples ($4 \times {}^{240}PuO_2$, $4 \times {}^{242}PuO_2$) were used [49], for a total mass of 3.6 mg of ^{242}Pu (~128 µg/cm^2 per sample, 99.97% purity) and 3.1 mg of ^{240}Pu (~109 µg/cm^2 per sample, 99.89% purity). The material was electro-deposited on an aluminium backing 0.25 mm thick and 5 cm in diameter, while the deposit itself

---

[1] The Lower Flammability Limit (LFL) is the lowest concentration (in %vol.) at which a flammable gas in air can ignite in the presence of an ignition source at a given temperature and pressure (usually 25 °C at atmospheric pressure).

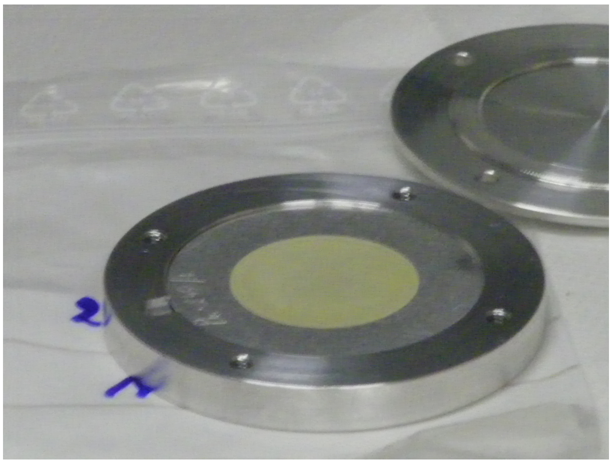

Figure 1.11: *A photograph of one of the plutonium samples used in the experiment. The 3 cm diameter yellowish PuO_2 deposit is visible on the 5 cm diameter aluminium backing. The sample is still in its individual container.*

had a diameter of 3 cm. Various contaminants were present in the plutonium samples, mainly in the form of other plutonium isotopes, such as ^{238}Pu, ^{239}Pu, ^{241}Pu and ^{244}Pu. While these impurities are present in very small amounts, the high fission cross-sections of fissile contaminants compared to the isotopes of interest dominate in the low neutron energy region (although the spontaneous fission background of ^{242}Pu was eventually found to exceed even this contribution, as will be discussed in Chapter 3).

Additionally, a ^{235}U sample (UF_4) with a mass of 18 mg deposited on a 0.2 mm-thick aluminium backing was used as reference. Since this sample had a diameter of 7 cm, its active area was reduced with a thin aluminium mask to match the diameter of the plutonium samples. The active mass was therefore reduced to 3.3 mg of ^{235}U (~469 μg/cm^2). All the samples were prepared at IRMM, Geel, Belgium and their characteristics are presented in table 1.1. One of the plutonium samples is shown in figure 1.11.

In order to mount the samples, which have a 5 cm diameter backing (8.4 cm for the ^{235}U sample), on the interior frame of the detector chamber, which is designed for the 18 cm diameter detectors, appropriate sample holders needed to be designed and manufactured. Furthermore, radio-protection requirements specifically precluded any use of glue or adhesive tape in contact with the sample backing. To meet these requirements, the samples were held in place by mechanical pressure only, which was applied by two thin aluminium foils with a hole of the appropriate diameter at the centre that were kept in contact with each other by two two-sided adhesive tape rings, as shown in figure 1.12. On the outer part, the two foils were fixed between two aluminium rings which adapt the whole module to the detector chamber inner frame, as shown in figure 1.13. The entire procedure was conducted in a Class-A laboratory under constant Radio-Protection supervision consisting of continuous air monitoring and surface measurements of sample containers, tools, working surfaces and protective gloves. The reverse procedure was followed under the same conditions for the dismounting and repackaging of the samples after the end of the experiment.

Table 1.1: *Main characteristics and stated impurities of the* ^{240,242}*Pu and* ^{235}*U samples utilised in the experiment, as reported in the IRMM target information sheets.*

Sample	**Mass (mg)**	**Areal density (mg/cm^2)**	**Activity (MBq)**	**Composition (%)**	
^{235}U $^{(a)}$	3.317	0.4692	$0.5409\cdot10^{-3}$	$<$ 0.001	^{233}U
				0.036	^{234}U
				99.94	^{235}**U**
				0.011	^{236}U
				0.013	^{238}U
^{240}Pu	0.716	0.1017	6.016	0.0733(29)	^{238}Pu
				0.0144(18)	^{239}Pu
				99.8915(18)	^{240}**Pu**
				0.00041(31)	^{241}Pu
				0.02027(41)	^{242}Pu
				0.000046(88)	^{244}Pu
^{240}Pu	0.776	0.1102	6.519	*same as above*	
^{240}Pu	0.809	0.1148	6.793	*same as above*	
^{240}Pu	0.763	0.1083	6.410	*same as above*	
TOTAL (^{240}Pu)	**3.064**	**0.435**	**25.738**		
^{242}Pu	0.862	0.1223	0.1263	0.002719(51)	^{238}Pu
				0.00435(18)	^{239}Pu
				0.01924(13)	^{240}Pu
				0.00814(31)	^{241}Pu
				99.96518(45)	^{242}**Pu**
				0.00036(13)	^{244}Pu
^{242}Pu	0.917	0.1301	0.1343	*same as above*	
^{242}Pu	0.917	0.1302	0.1344	*same as above*	
^{242}Pu	0.920	0.1305	0.1348	*same as above*	
TOTAL (^{242}Pu)	**3.616**	**0.5131**	**0.5298**		

$^{(a)}$ Data for the active area of the sample, as explained in the text.

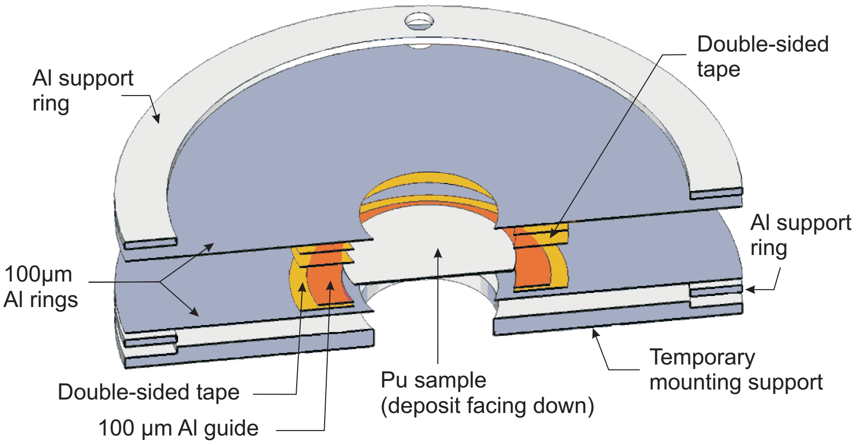

Figure 1.12: *A schematic view of a sample holder with all its components [50]. The sample is sandwiched between two thin aluminium foils that are kept together at the centre by double-sided adhesive tape, which is not in contact with the sample itself. These foils are then connected to two aluminium rings that are compatible with the internal support frame of the detector chamber.*

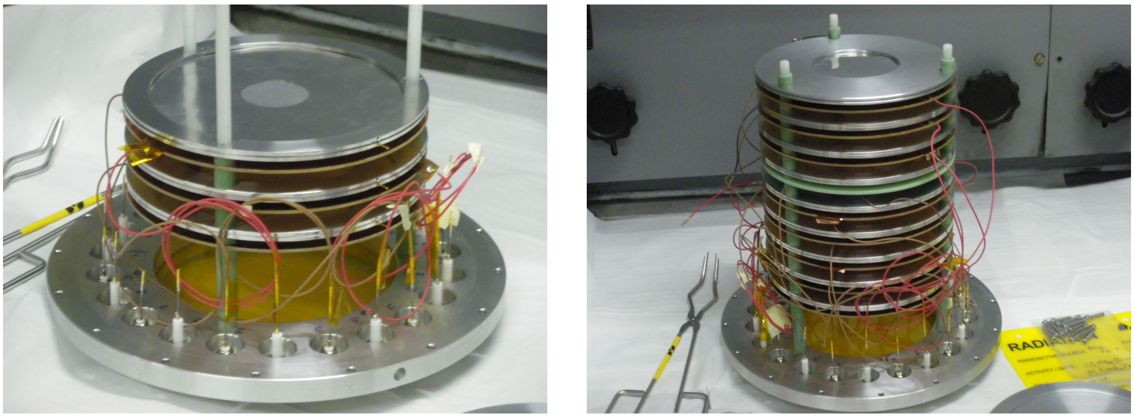

Figure 1.13: *Two photographs showing different stages of the mounting of samples and detectors into the chamber. A sample holder with the plutonium sample in its centre (facing down) is shown in place in the left panel.*

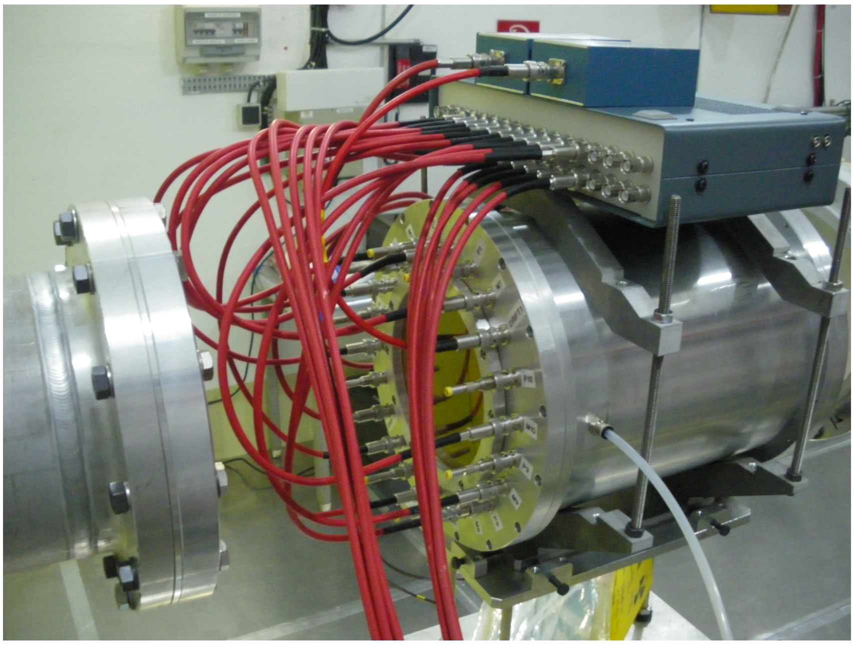

Figure 1.14: *A photograph of the setup installed in the experimental area. The preamplifier module is placed on top of the detector chamber along with the two high-voltage filters. The high-voltage cables for the meshes, entering from the bottom of the pictures, are connected to the preamplifier box and distributed from there to the detectors through the connectors available on the chamber. The gas intake tube is visible entering from the bottom right. The neutron beam arrives from the right side of the picture. Although not obvious in this picture, all cables are well outside the neutron beam.*

1.2.3 Electronics and data acquisition

Existing electronics from previous fission measurements were used for fast signal shaping. A 16-channel preamplifier module, constructed at INFN-Bari, was placed next to the detector chamber. The mesh voltages were applied and the detector signals read through this module, while the drift voltage was applied directly to the detectors through two high-voltage filters, each serving half of the detectors. Based on the experience accumulated during off-beam tests of the detectors prior to the measurement, additional electronic protection was added to the pre-amplifier channels to prevent breakage in case of sparks. Furthermore, the shielding of the preamplifier module was improved to mitigate the baseline oscillation observed following the prompt γ-*flash*, which is discussed in Chapter 3. A view of the experimental setup is shown in figure 1.14.

The analogue detector signals were input from the preamplifier module into the standard n_TOF Data Acquisition System [51] based on 8-bit *Acqiris* (now *Agilent* [52]) flash-ADCs. The use of fast electronics is essential for measurements such as those performed at n_TOF, where fast timing is a critical element in order to resolve short times-of-flight and high counting rates in detectors. By using fADCs, the analogue waveform of the detector signals can be sampled at a chosen sampling rate up to 1 GHz. Depending on the requirements and characteristics of each measurement, the choice of sampling rate is made depending on two factors: a) the width of the signals (the sampling rate must be high enough to adequately describe the shape of the signal) and b) on the energy

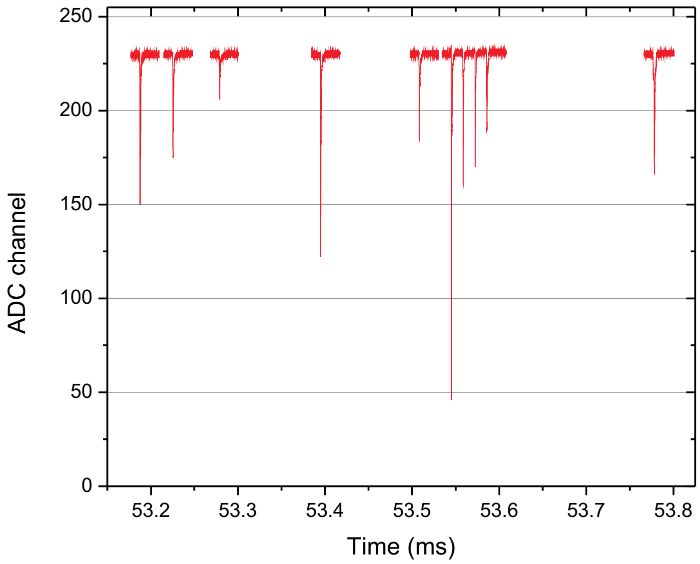

Figure 1.15: *A short section (few hundred µs) of a raw data 'movie' obtained after the digitisation of the analogue signal of a detector. The pre- and post-samples stored before and after each signal are evident, as is the effect of the zero-suppression algorithm.*

range of interest; due to the 8 MB memory limit of the buffer, a higher sampling rate means acquisition lasts for a shorter time during which lower energy neutrons have not yet arrived in the experimental area. For these reasons, a sampling rate of 100 MHz (one sample per 10 ns) was chosen for this measurement, which allowed to have an ~80 ms recording window (or 'movie') that corresponds to a lower energy limit of ~30 meV and was sufficient to adequately describe the detector signals that had a rise-time of approximately 50 ns and a FWHM of 120-150 ns.

Beam-off data is collected using an artificial trigger that opens an acquisition window of the same duration as for the beam-on data (80 ms) once per second. In this manner, α-particle or spontaneous fission events detected in the beam-off runs can be assigned an equivalent 'time-of-flight' to study their time distribution relative to events detected in the beam-on data.

In order to minimise the volume of data that need to be transferred and recorded, a zero-suppression algorithm is employed to avoid recording long sequences of noise where no useful signals are present. Each time a signal amplitude threshold that has been set for each detector is exceeded, the data is recorded up to the next threshold crossing of the falling signal with the addition of a fixed number of samples before and after the threshold crossings (512 pre-samples and 2048 post-samples) in order to ensure that the full signal waveform is obtained. In case more signals arrive within an acquisition window initiated by a previous signal, the window is extended until the last signal is recorded. The pre-trigger and post-acquisition window samples are later used in the analysis to determine the signal baseline and study the noise level, as described in Section 3.1. A fragment of a raw data 'movie' is shown in figure 1.15.

After the digitisation of the analogue detector output, the raw data are temporarily saved on a local disk. Complementary information on each recorded signal is also stored, such as the detector number, the event number (one 'event' corresponds to one proton bunch), the type of proton pulse (dedicated or parasitic) and the proton pulse intensity. Once the files reach a specified size they are transferred to *CASTOR (**C**ERN **A**dvanced **STOR**age manager)* [53], the CERN central data storage system. There they remain on another temporary disk pool, before being transferred on tape for long-term storage.

Chapter 2

Monte-Carlo simulations

This chapter covers the extensive simulation work performed on two important aspects of the experiment, namely the n_TOF neutron beam and the Micromegas detectors, and is subdivided accordingly. Results from these simulations were useful for several experiments performed at n_TOF and increased the understanding of certain characteristics of the facility, while the simulation of the detector response was essential for the data analysis of the present work. Only the technical aspect of the simulations is presented here, from the setup to the extraction of results; the utilisation of these results in the analysis is discussed later in the appropriate sections of this thesis.

2.1 The FLUKA and MCNPX codes

The simulations were performed with the FLUKA [54, 55] and MCNPX [56] particle transport codes. The choice of using both FLUKA (development version) and MCNPX (version 2.6) was made in order to take advantage of each code's strengths in studies where a variety of particle interactions, spanning several orders of magnitude in energy, need to be followed. In particular, FLUKA boasts very accurate and well-benchmarked high-energy hadron interaction models, appropriate for simulating the proton beam interaction with the spallation target. Nevertheless, the transport of neutrons below 20 MeV (and down to the lowest threshold of 0.01 meV) is performed by a multi-group algorithm and an associated grouped cross-section library. The above mentioned energy range is subdivided into 260 groups of approximately equal logarithmic width where inelastic reactions are not simulated explicitly, but treated as transfer probabilities between energy groups, forming a so-called *downscattering matrix*. While this approach is very CPU-efficient and generally reliable for a variety of applications, it can lead to unphysical artefacts when studying thin and/or low density bodies or when the resonance structure of the studied material is relevant to the problem (e.g. in shielding applications) [57]. This implies a limitation, for instance, in extracting accurate information on the resonance absorption dips present in the n_TOF neutron energy spectrum. It is in this context that MCNPX becomes useful, since it employs point-wise neutron cross-sections down to thermal energies.

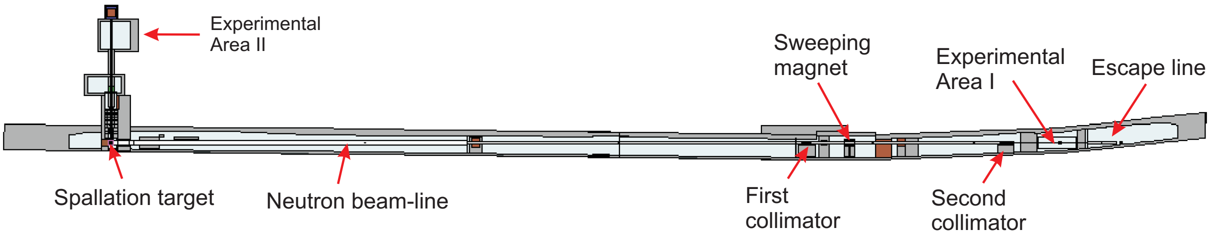

Figure 2.1: *Full geometry of the n_TOF facility, as implemented in FLUKA.*

2.2 The n_TOF neutron beam

During the 2011-13 period, a concerted effort was made within the n_TOF collaboration to bring together all available information on key aspects of the facility. In particular, the most important goals set were to produce an evaluated neutron flux, to study the spatial profile of the neutron beam and to determine the facility's *resolution function*, which is critical in achieving a reliable *Tof*-to-energy calibration. Additionally, the in-beam photon background and charged particle production in the second collimator were also studied. This work entailed extensive Monte-Carlo simulations covering all the aspects mentioned above, results of which were combined with experimental data, where available. The validation of simulations with experimental data allows to extract further information that is not experimentally accessible, as is the case, e.g. for the neutron moderation length (see section 2.2.5). An overview of this work can be found in Guerrero et al. [31], while additional experimental details on the evaluation of the neutron flux are given in Barbagallo et al. [58] and details on the spatial profile extraction can be found in Belloni et al. [59].

2.2.1 Simulated geometry and primary particle source

Since the start-up of the n_TOF facility in 2001, the geometry of the facility has been implemented in FLUKA in considerable detail, as illustrated in figure 2.1. The changes made during the upgrade period (2004-2008), particularly the new spallation target assembly, are reflected in the simulated geometry. The geometry was checked against the technical drawings of relevant components (spallation target, proton, neutron and vacuum windows, cooling and moderator layers etc.) and civil engineering layouts of the facility (tunnels, target area, shielding etc.) taking advantage of the built-in feature of FLAIR [60], the FLUKA Graphical User Interface (see figure 2.2). Furthermore, the composition of the materials and especially the aluminium alloys which constitute the various windows and beam-line components were defined in the highest possible detail taking into account the available specifications and their chemical and isotopic composition. The geometry was automatically exported to MCNP format through FLAIR. Apart from the obvious gains in time, since such a complicated geometry did not need to be rebuilt in a different code, this automated translation allows the two codes to run on an identical geometry at least down to the point of the material cross-sections called, where differences can and do exist.

As can be seen in figure 2.1, the full geometry of the facility is included, from the spallation target to the experimental area, some 185 m away. What was of particular importance for this study, however, was the geometry of the spallation target assembly,

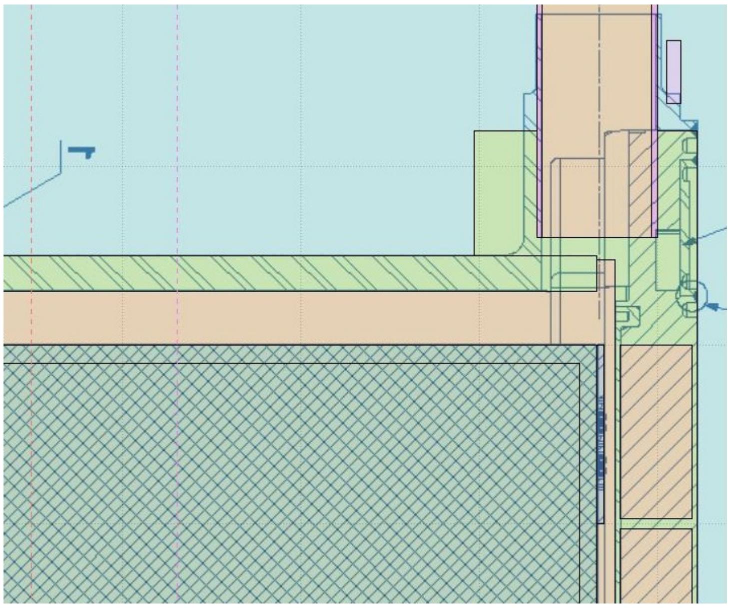

Figure 2.2: *A screenshot from FLAIR with an example of the built-in feature that allows to overlay the simulated geometry and a technical drawing of the same components or area. In this case, a small section of the spallation target assembly and the moderator window are visible.*

including the lead target itself, the water of the cooling and moderation circuits and the windows that contain these layers (figure 2.3). Indeed, for the purposes of studying the characteristics of the neutron beam – and other particles produced in or near the target that travel towards the experimental area – it is necessary to simulate only the lead target and the area immediately surrounding it.

The primary beam of 20 GeV/c protons impinging on the spallation target was appropriately defined to match the energy and spatial distribution of the real proton bunches, as provided by the CERN Proton-Synchrotron (PS).

2.2.2 Methodology

The goal of the simulations is to follow the proton beam interaction with the lead spallation target and the neutron and γ-ray production that follows. Secondary charged particle production was not considered, as it had been previously studied during the design phase to select the appropriate characteristics for the sweeping magnet.

A full simulation of the particles (especially the neutrons) travelling along the beamline all the way to the experimental area would be impractical, considering that the solid angle subtended by the second collimator is less than 10^{-8} sr. Such calculations would require an amount of computing resources far beyond what can be reasonably available. To address this issue, the particles were tracked up to a scoring plane only a few tens of centimetres after the lead target, corresponding to the entrance of the vacuum tube that eventually leads to the experimental area (see figure 2.3). In particular,

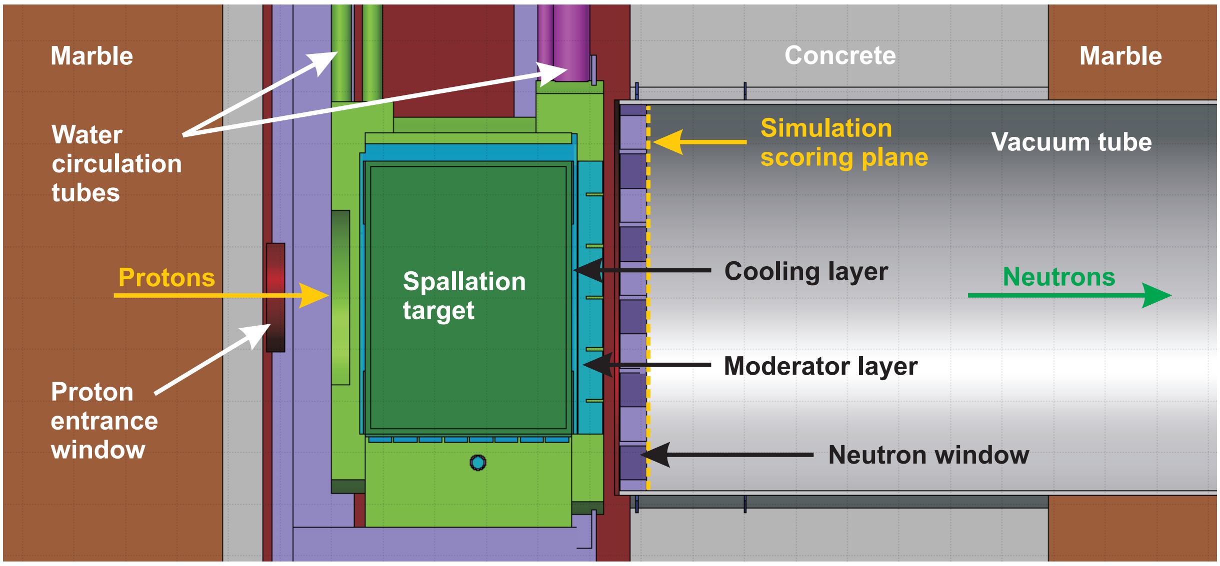

Figure 2.3: A more detailed view of the spallation target and the surrounding structure, as implemented in FLUKA. Particles produced in the target were scored on a plane at the entrance of the vacuum tube, as shown.

the neutron or γ-ray position (three coordinates), direction (three directional cosines[1]), energy, weight (importance) and time of arrival (defined as the time between the primary proton hitting the target and the secondary particles reaching the scoring plane) were scored. Particles entering the vacuum tube at an angle greater than 10° relative to the beam-line axis are immediately discarded as they would not reach the experimental area, thus also reducing the size of the dump files to a more manageable size. Once stored, this information is used by an independent external program that was written to perform an *a posteriori* propagation of the particles towards the experimental area and implements a variance reduction algorithm. The following description focuses on the implementation for neutrons; photons are treated similarly, except for the effect of gravity, as explained below.

The operation of this program rests on one particular assumption: within a sufficiently small angle θ_{cut} (relative to the beam axis) neutrons are emitted isotropically throughout the full energy range. In general, this is not true: high-energy neutron emission from the spallation target is (strongly) forward-peaked, while the thermal neutron flux is largely isotropic. Nevertheless, the assumption holds within a small forward angle

---

[1] For a vector v in $\mathbb{R}^3$, we can define the directional cosines as:

$$\alpha \equiv \cos a \equiv \frac{v \cdot \hat{x}}{|v|}$$
$$\beta \equiv \cos b \equiv \frac{v \cdot \hat{y}}{|v|}$$
$$\gamma \equiv \cos c \equiv \frac{v \cdot \hat{z}}{|v|}$$

where a, b, c are the angles between the vector and the Cartesian axes and $\hat{x}, \hat{y}, \hat{z}$ are the corresponding unit vectors. It then follows that:

$$\alpha^2 + \beta^2 + \gamma^2 = 1$$

This last property is routinely used in FLUKA to calculate the third directional cosine, once the other two have been determined, and must always be satisfied to double precision.

$\theta_{cut} = 5^\circ$; a conservative value of $\theta_{cut} = 3^\circ$ was thus used for these calculations.

The first step is to project each neutron's trajectory and determine its hitting point at a distance L corresponding to the experimental area (without accounting for any collimation) and discard all those that arrive outside a circle of radius $L \cdot \tan\theta_{cut} + 0.4$ m, (e.g. $183\text{ m} \cdot \tan 3^\circ + 0.4\text{ m} = 9.6\text{ m}$), where the radius of the vacuum tube after the lead target (i.e. the neutron scoring surface) is 0.4 m and is included to account for the beam halo. The remaining neutrons are the ones assumed to be emitted isotropically and included in the next step of the calculation.

Subsequently, a scoring surface in the experimental area is selected, defined by its position along the beam line (e.g. 183 m) and its radius (e.g. 2 cm). This surface is meant to represent a sample or detector. A scoring grid is defined on this surface and, for each neutron, a trajectory is calculated to each point on this grid starting from its initial position at the beginning of the vacuum tube. The grid can be defined arbitrarily, but a grid of 1 mm step was selected as a reasonable compromise between spatial resolution and computing time. Information on the neutron beam line (tube diameter reductions, collimator positioning and misalignments) is fed to the routine. For each instance of the neutron (i.e. for each calculated trajectory) the program checks if this trajectory hits either a tube or collimator. If so, this (instance of the) neutron is considered not to reach the experimental area. In the opposite case, it is scored.

It should be noted that, in calculating the neutron trajectories, the program was designed to account for the effect of gravity. While fast neutrons are practically unaffected over a 185 m flight-path, the effect is visible for thermal neutrons; a 26 meV neutron emitted horizontally will 'fall' by about 3.3 cm over a 185 m path. This has a non-negligible impact on the spatial profile of low energy neutrons (more details are given in Section 2.2.4).

The multiple utilisation of each simulated neutron is the element of this algorithm that allows us to increase the statistics of neutrons scored in the experimental area compared to what would be the result of a direct simulations with full transport of neutron through the entire beam line, as mentioned at the beginning of this section. The final result is appropriately normalized to provide the 'real' neutron flux and the spatial beam profile at the scoring surface in the experimental area.

2.2.3 Neutron flux

Figure 2.4 shows the simulated neutron flux in comparison with the evaluated flux determined experimentally and again expressed in isolethargic units (see Appendix A). The simulations are in overall fair agreement with experimental data, except for the high-energy region, where the models used to simulate high-energy hadronic interactions play a significant role. The small 'step' in the simulated data below around 4 eV corresponds to the energy where MCNPX begins using its so-called 'thermal cross-sections'. The overall good agreement with the experimental flux, especially in the description of the absorption dips that are due to the material encountered by the neutrons along their path (figure 2.5), confirms that the geometry and materials were accurately defined and that results from these simulations can be relied upon to extract additional information on the neutron beam, as described in the following sections.

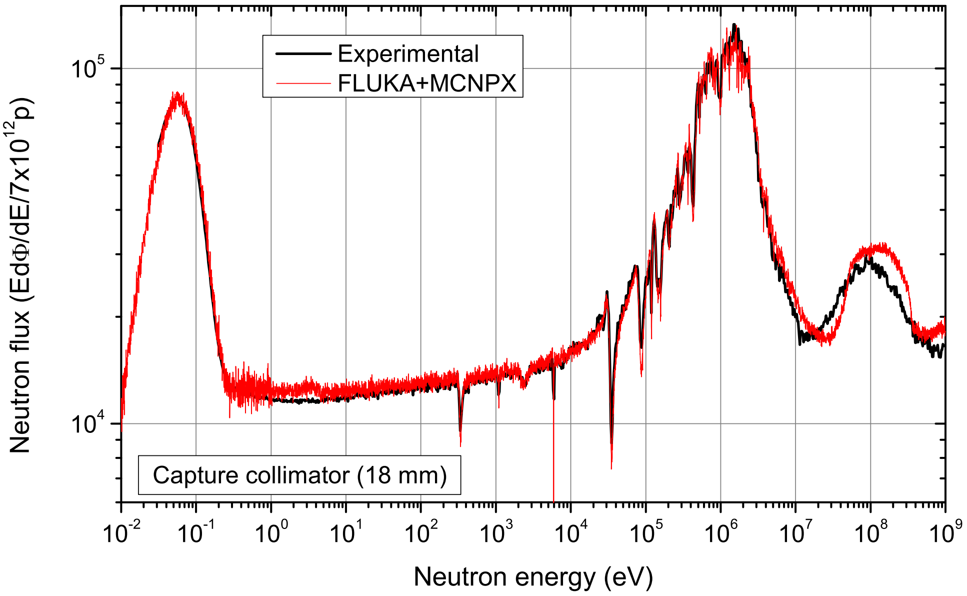

Figure 2.4: *Comparison of the simulated neutron flux with the evaluated experimental flux for the capture setup (18 mm collimator) and water as moderator.*

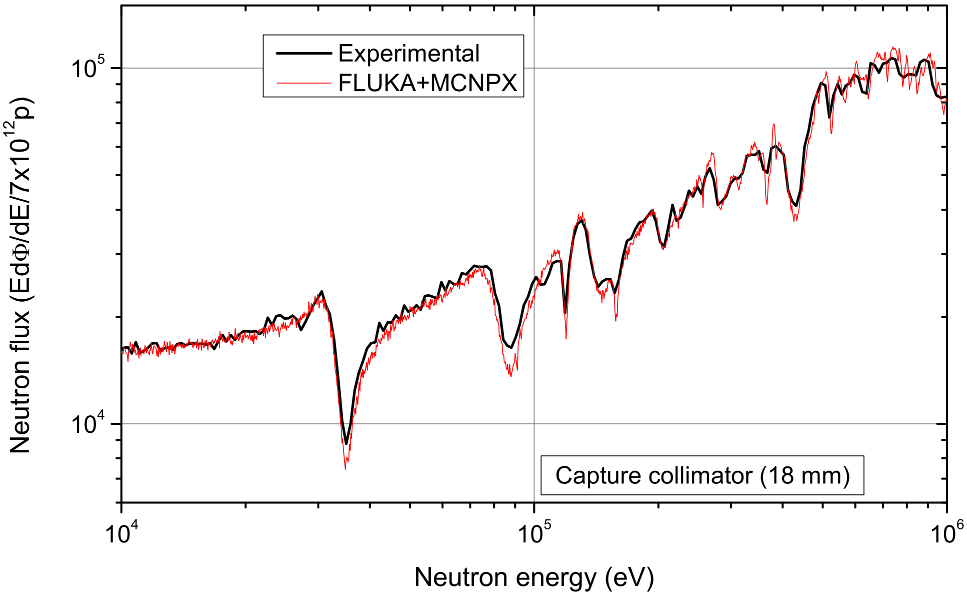

Figure 2.5: *Comparison of the simulated neutron flux with the evaluated experimental flux for the capture setup (18 mm collimator) and water as moderator, in the energy region 10 keV-1 MeV.*

2.2.4 Spatial profile and beam interception factor

While scoring the neutrons arriving in the experimental area, as previously described, the coordinates of impact on the scoring surface were also recorded. In this manner, it is possible to reconstruct and study the spatial profile of the neutron beam. Since the beam is shaped by the two collimators, the effect of the collimation system on the profile was investigated. Furthermore, as the neutron production inside the spallation target is not uniform and the emission of neutrons is strongly dependent on the energy, especially for higher energies, the energy dependence of the spatial profile was also studied.

As can be seen in figure 2.6, the full beam profile has a quasi-Gaussian shape. The asymmetry observed in the distribution, as well as the offset from the centre of the beam-axis is due to the known misalignments of the collimators. Furthermore, it can clearly be seen that the high-energy fraction of the beam is much more forward-peaked and has a 'flat' distribution nearly 1 cm in diameter.

When samples are smaller than the neutron beam size it often becomes necessary for the data analysis to determine which fraction of the beam is actually intercepted by the sample, except in the case of a relative measurement where both the sample of interest and the reference sample have the same dimensions and are located at approximately the same position, so that they can be considered to receive the same neutron flux. The so-called *beam interception factor (BIF)* of a sample of radius R can be expressed as:

$$BIF(E_n) = \frac{N_R(E_n)}{N_{TOT}(E_n)} \tag{2.1}$$

where N_{TOT} is the total number of neutrons in the beam at the given position of the sample and N_R is the number of neutrons hitting the sample.

The beam interception factor is expected to vary with energy, since high-energy neutrons are more forward-peaked than low-energy neutrons, and it is also expected to be sensitive to misalignments of the collimators and the sample. Having the ability to determine the spatial profile of the beam at a given position, it is simple to use the simulated data to extract the BIF as well.

Assuming a realistic collimation setup, reflecting the present status of the facility, and considering samples that are perfectly aligned with the beam axis, the BIF was calculated for sample diameters of 1, 2, 3 and 4 cm. The results can be seen in figure 2.7a. Three important features of the BIF curves should be noted. The fact that thermal and epithermal neutrons are emitted largely isotropically is reflected in the practically flat behaviour of the BIF in the 0.1 eV-100 keV region. As we go to higher neutron energies, the emission is more forward-peaked; as a result, the high energy fraction of the neutron beam is narrower, and the BIF naturally increases. A third feature is not so readily explained; this is the abrupt drop of the BIF below ~10 meV. Indeed, this feature is not related to the emission angle of the neutrons – thermal neutron emission is isotropic –, but to the effect of gravity. Thermal neutrons are slow enough (arriving around 100 ms after the GeV neutrons) for their path to be curved downwards by gravity sufficiently to 'miss' the samples.

In order to estimate the sensitivity of the BIF to the sample position, which could occur due to a small misalignment of the sample, the effect of a 1 mm horizontal or verti-

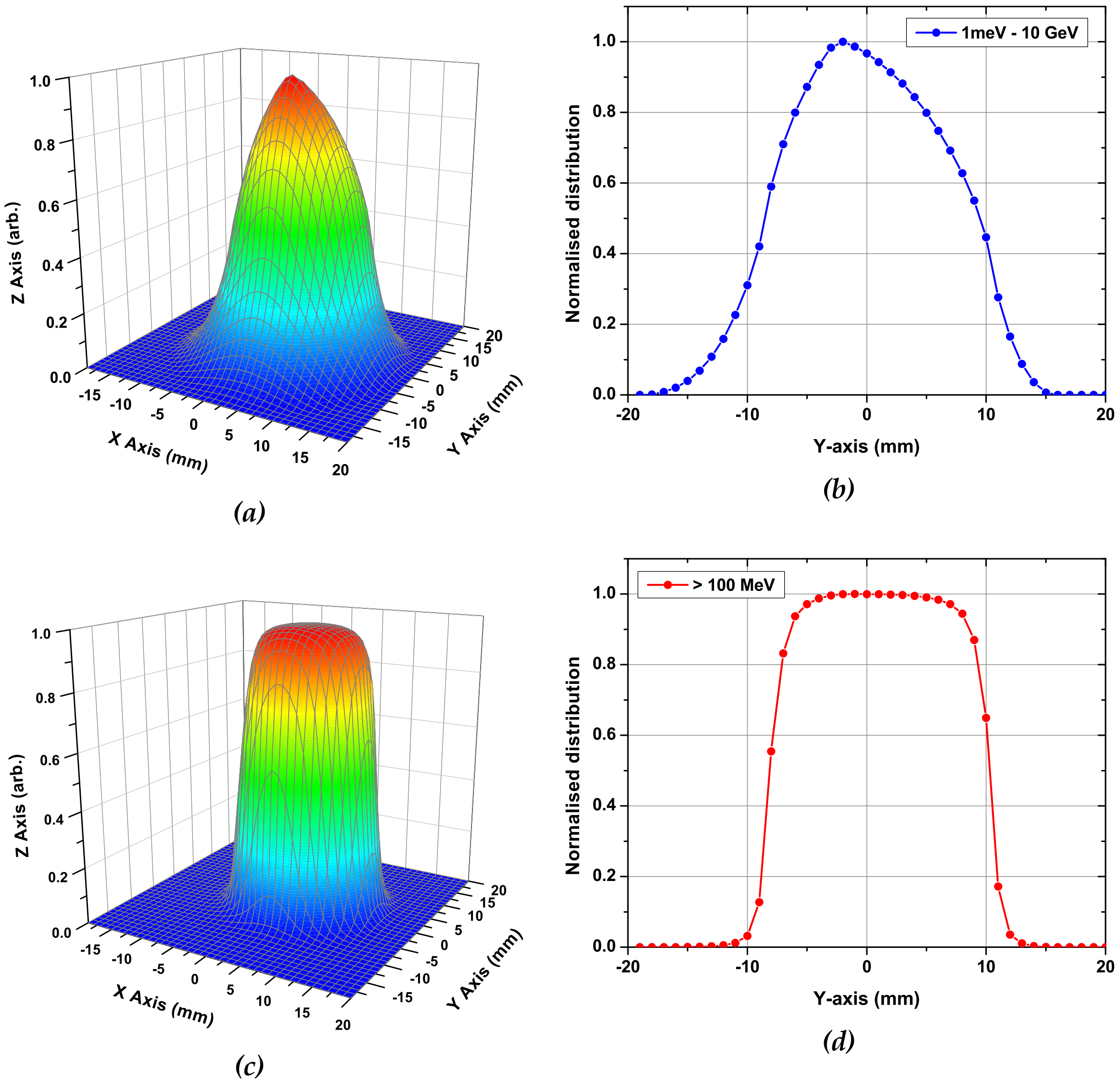

(a) *(b)* *(c)* *(d)*

Figure 2.6: *The simulated n_TOF neutron beam profile at 183 m from the spallation target (i.e. shortly after entering the experimental area) for the capture collimator setup: (a) the full beam profile and (b) its vertical projection, (c) the beam profile above 100 MeV and (d) its vertical projection. It can be observed that the high-energy part of the beam is much more forward-peaked. Overall, the beam diameter is less than 4 cm.*

cal misalignment relative to the reference position of a 2 cm sample was studied. The results can be seen in figure 2.7b. It is evident that a vertical misalignment is more important and heavily influences the shape of the *BIF* in the thermal region. This is related to the effect of gravity, as explained above; an upwards misalignment of the sample will lead it to lose even more of the 'falling' thermal neutrons leading to a further reduction of the *BIF* at thermal energies. Overall, the simulated misalignments lead to a fluctuation of the *BIF* value at thermal of several percentage points. For neutron capture experiments that rely on measuring the ratio of *BIF* values at 4.9 eV (the giant resonance energy in Au) and 26 meV (thermal neutrons), understanding this source of uncertainty is critical for the final cross-section calculation.

Results from simulations have been compared with the experimentally obtained spatial profile. These measurements were carried out with a newly commissioned pixel-Micromegas detector and are presented in more detail in Belloni et al. [59]. This comparison is useful to validate experimental results and to extend them to the higher energy range, but also invaluable for understanding and quantifying sources of uncertainty that are not readily accessible from experiments.

2.2.5 The effective neutron moderation length

The effective neutron moderation length was calculated from the simulated data as described in section 1.1.3. The full λ-distribution of the n_TOF neutron beam, including the contribution of the proton pulse width, is shown in figure 2.8. It can be observed that the shape of the distribution is strongly asymmetrical and varies greatly with energy, which makes clear why the simple Tof-to-energy relation (eq. 1.1) cannot be used to obtain accurate results. From this distribution, the mean λ-value for each energy bin can be extracted for further use. The corresponding curve is shown in figure 2.9a.

Fitting the data for the mean value with an $E^{-\frac{1}{2}}$ curve, as described in section 1.1.3, the t_0 offset is found to be approximately 163 ns. This value is larger than the 64 ns value reported in Lorusso et al. [37] which corresponds to the different spallation target assembly used for n_TOF-Phase I experiments (2001-2004). The different data and fits for Phase I and Phase II are compared in figure 2.9b.

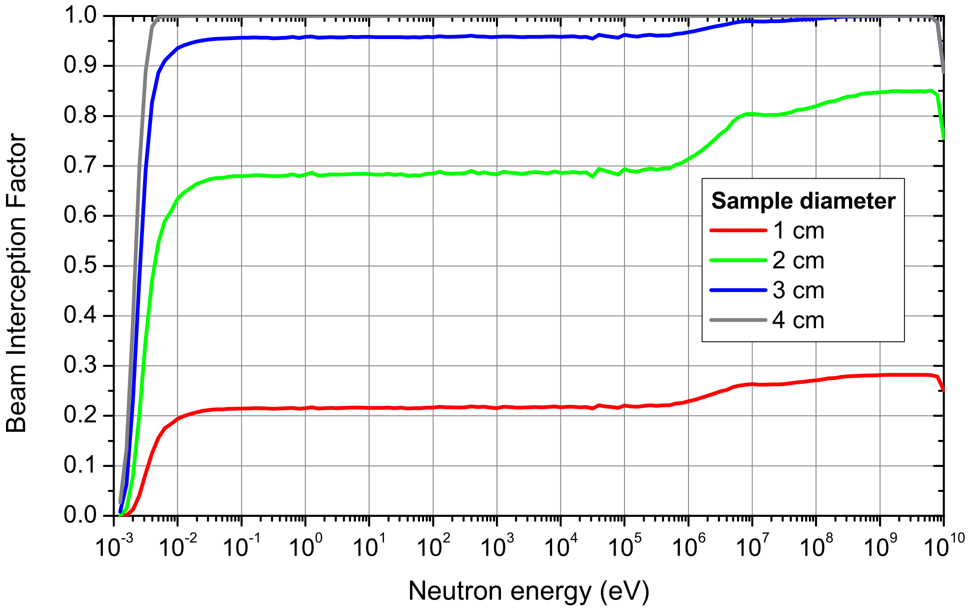

(a) *The simulated beam interception factor for samples of 1, 2, 3, and 4 cm diameter.*

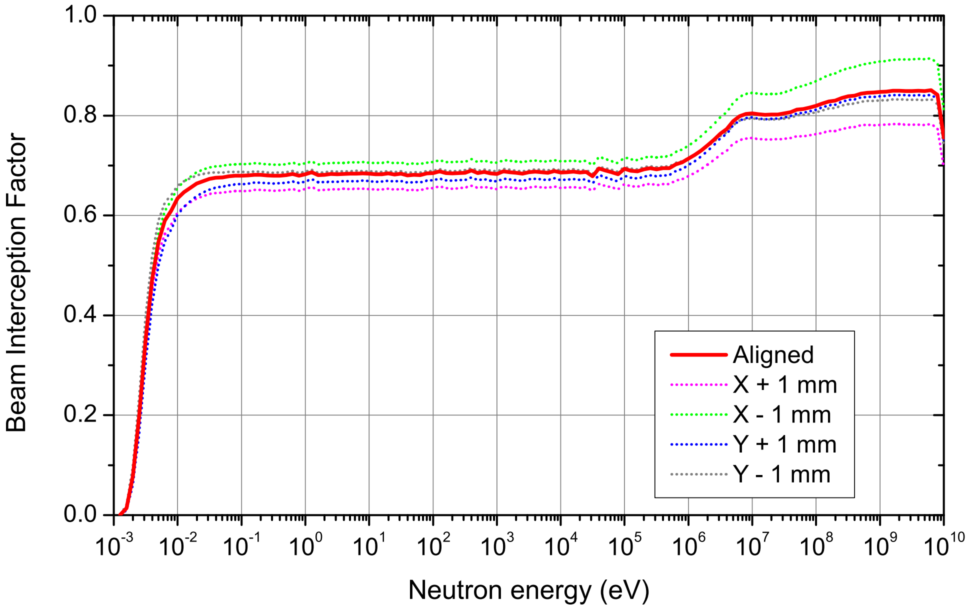

(b) *Effect of a 1 mm horizontal (X) or vertical (Y) misalignment of a 2 cm diameter sample on the beam interception factor. Differences of up to about 7% with respect to the reference values for a perfectly aligned sample are observed.*

Figure 2.7: *Simulated beam interception factor for different sample diameters (a), and effect of the sample misalignment on the beam interception factor (b).*

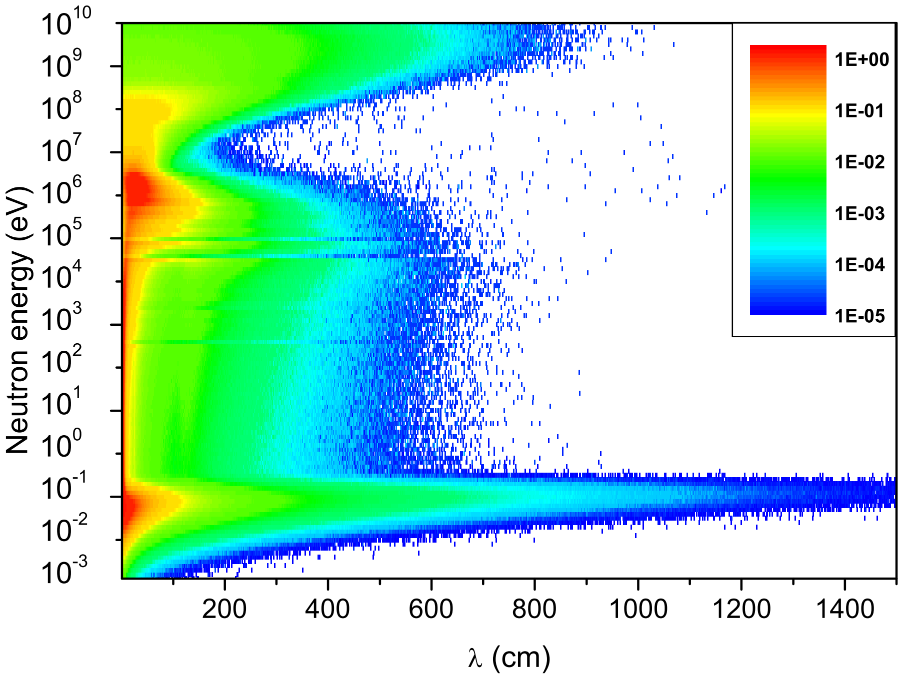

Figure 2.8: *The full λ-distribution of the n_TOF neutron beam, including the contribution of the proton pulse width which is dominant for high energies.*

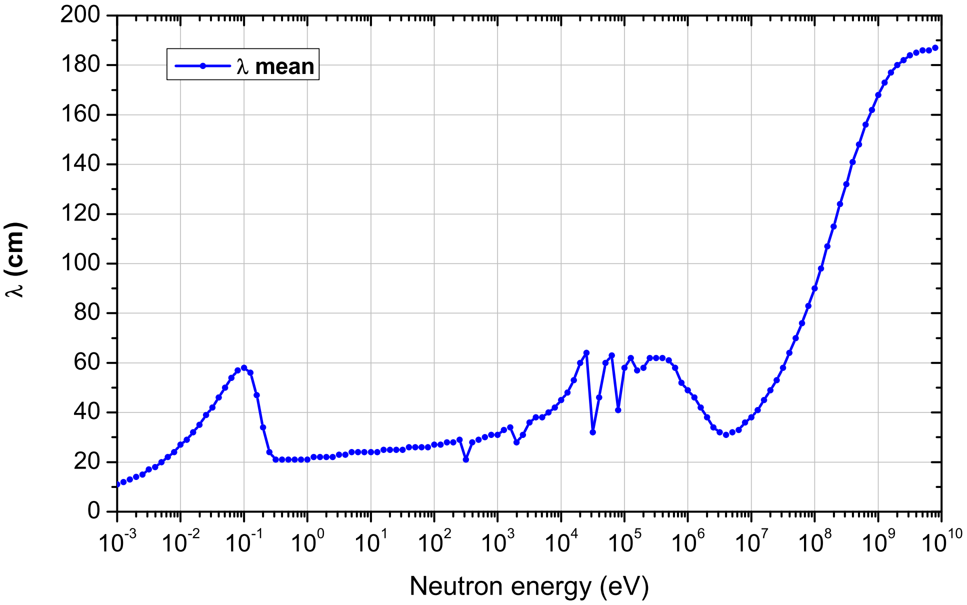

(a) *The mean value of the λ-distribution shown in figure 2.8 as a function of neutron energy.*

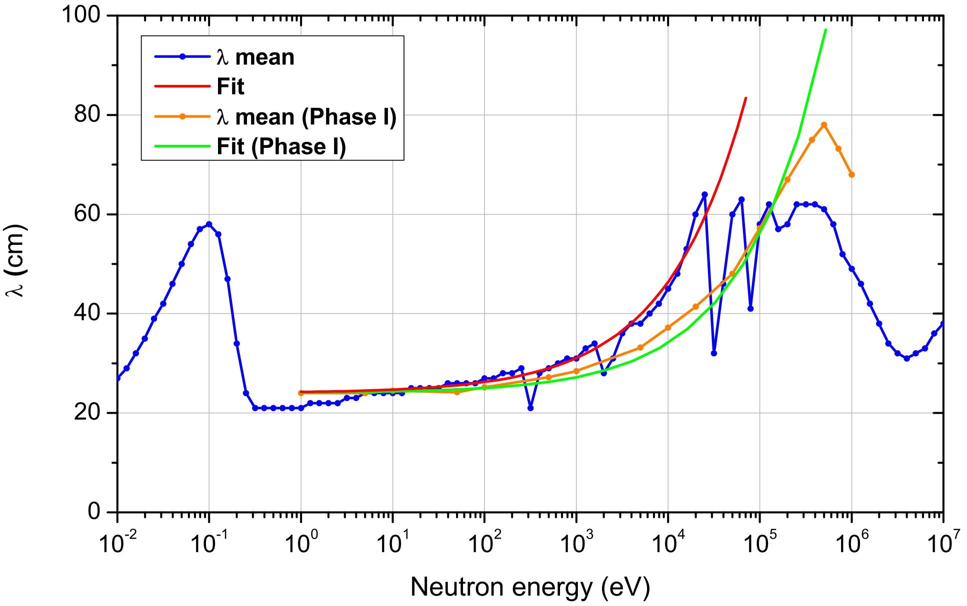

(b) *Simulated data of the mean value of the λ-distribution for the present and past (Phase I) target layout. The fits of the data to determine the t_0 offset in both cases are also shown. Phase I data are taken from Lorusso et al. [37].*

Figure 2.9: *Mean value of the λ-distribution (a), and comparison with Phase-I data, along with the corresponding t_0 fits.*

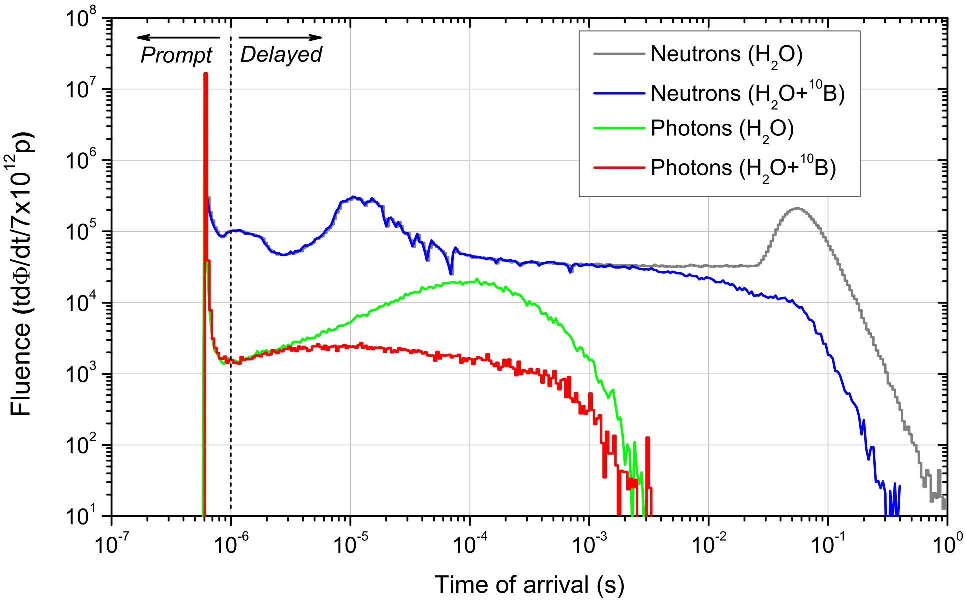

Figure 2.10: *Time-of-arrival of in-beam photons in the experimental area. The existence of a prompt and delayed component is evident. The time-of-arrival of the neutrons is also shown for comparison.*

2.2.6 In-beam photons

The interactions of the protons and neutrons with the spallation target and the materials surrounding the target and the beam-line lead to a significant production of γ-rays, a fraction of which reaches the experimental hall. Knowing the energy and time-of-flight distribution of these photons is essential for understanding the effects of the γ-ray backgrounds, where a prompt and delayed component can be distinguished.

Applying the same methodology described earlier for the study of the neutron flux, it has been possible to obtain the information on the photon flux. The time-of-flight of the photons arriving in the experimental hall has been studied, with the results displayed in figure 2.10. The existence of a prompt (*Tof*<1 μs) component arising from high-energy interactions in the target and a delayed (*Tof*>1 μs) component comprising mostly γ-rays produced from neutron capture reactions in the surrounding material is manifest. Indeed, the energy distribution of the γ-rays belonging to each of these two components reflects the very different origins of the prompt and delayed γ-ray background (figure 2.11). While the much larger prompt component reaches energies as high as several GeV, the delayed component features well defined peaks corresponding to neutron absorption reactions in different materials. For instance, the peaks at 478 keV, 511 keV and 2.2 MeV correspond to ^{10}B(n,α)^{7}Li*, pair annihilation and ^{1}H(n,γ) reactions respectively, while the peak at ~7.7 MeV is due to capture reactions in aluminium, lead and iron. It should finally be noted that, as expected, the prompt component is not affected by the choice of moderator, while the strong suppression of the 2.2 MeV peak with the use of borated water is evident and constitutes a major improvement compared to the situation prior to the installation of the new target assembly in 2008, when this background was a limiting factor for measurements.

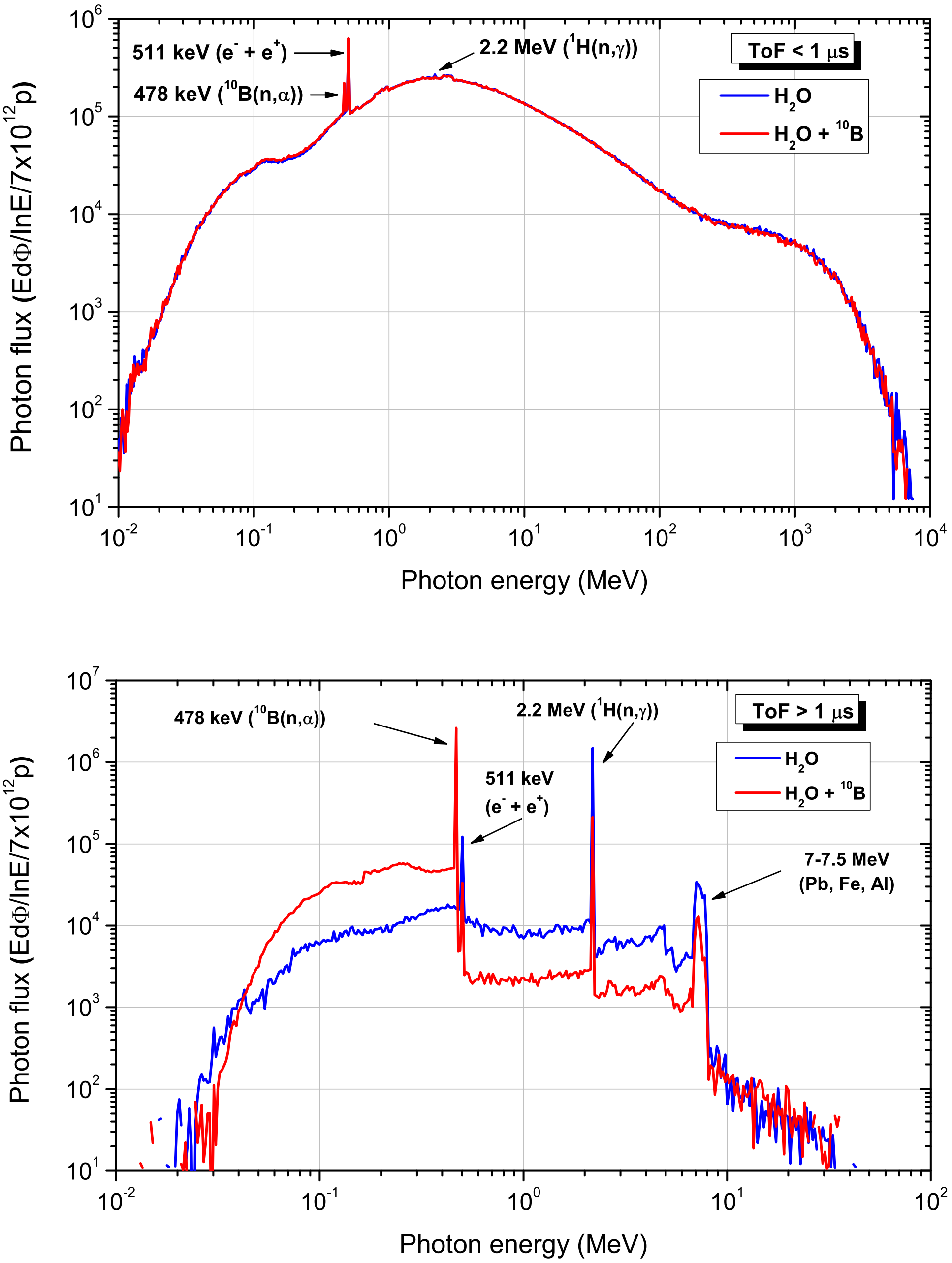

Figure 2.11: *Energy distribution of the prompt (top) and delayed (bottom) components of the in-beam γ-rays (see figure 2.10 and explanation in the text). While the prompt component, which contains photons with energies up to several GeV, remains largely unchanged with the addition of ^{10}B in the moderator (as expected), a very significant decrease of the delayed component above 500 keV can be observed.*

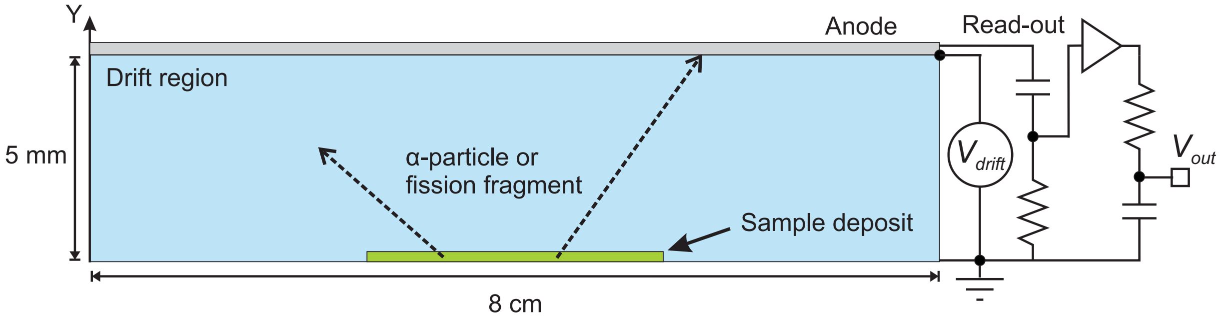

Figure 2.12: *Simplified geometry of the detector active volume and the sample used in the simulations. The electronic circuit assumed for the signal shaping that is performed at a later stage is also shown. (Drawing not to scale.)*

2.3 The Micromegas detectors

The behaviour of the Micromegas detectors was studied by means of Monte-Carlo simulations performed with FLUKA and processed with custom software written for this purpose. The aim of these simulations was to reproduce the experimental pulse height spectra of α-particles and fission fragments for the evaluation of the detector efficiency and the quality of the peak-search routine that was used to parse the experimental raw data. In general, this method could be used to study the influence of several parameters on the obtained spectra, such as the gas pressure, the drift gap and the drift voltage. In reality, the values of many of these parameters in this particular experiment were limited by other experimental considerations. For example, radio-protection requirements mandated that the gas pressure not exceed 1 bar to prevent possible leaks of radioactive material from the chamber; the drift space could not exceed 5 mm, given the available space in the chamber; and the drift voltage could be raised only up to the point where the number of sparks occurring in the detector remained very limited.

2.3.1 Detector geometry, sources and scoring

A simplified geometry was constructed, consisting of a single cylindrical gas volume and a sample deposit, as illustrated in figure 2.12. The dimensions of the gas volume were those of the active region of the detector, while the diameter and thickness of the sample were varied to match the characteristics of each simulated sample. The appropriate composition was defined for the gas mixture, while the density was calculated for a gas pressure of 1 bar.

The primary particle sources (α-particles and fission fragments) were defined with custom source routines. An isotropic emission over a 2π solid angle (in the direction of the gas volume) was defined for all particles. For the α-particles, the known average energy, which is usually between 4.5 and 5.0 MeV, was retrieved from EXFOR [13,14] and appropriately assigned in each case. Fission fragments, on the other hand, have a more complicated mass and energy distribution, which are difficult to predict theoretically. Various systematics are available and can be used to generate fission fragment events. One recent development, however, is the *GEF (**GE**neral **F**ission)* code [61–63]. The GEF code is an implementation of a semi-empirical model of the fission process, which treats

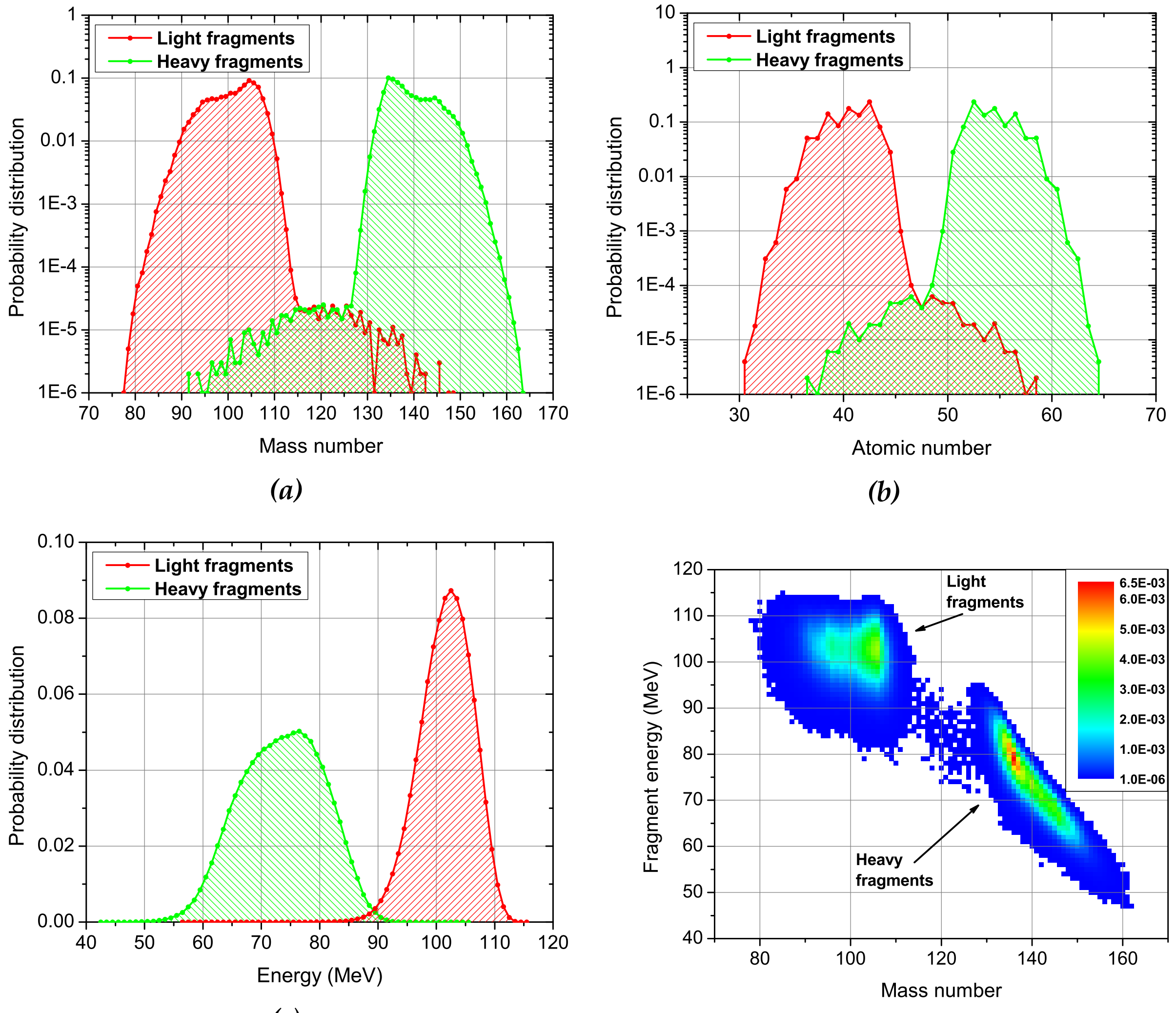

(a)

(b)

(c)

(d)

Figure 2.13: *Mass and energy distributions of ^{242}Pu fission fragments induced by an n_TOF-like neutron spectrum, as obtained with the GEF code: (a) mass distribution of light and heavy fragments, (b) atomic number distribution of the fragments, (c) kinetic energy distribution of the fragments, (d) mass distribution of the fragments plotted against their kinetic energy.*

different fissioning nuclei with a set of global parameters. Results from GEF have been found to be in good agreement with available experimental data. The relevant quantities of the nuclei involved in the calculations (mass, charge etc.) are sampled with a Monte-Carlo algorithm. An example of mass and energy distributions of fission fragments obtained with the GEF code and used in these simulations is shown in figure 2.13. The calculation was performed for ^{242}Pu, assuming an n_TOF-like neutron spectrum. The contribution of different fission modes (see Section 4.1.3) to the final mass distributions could also be obtained, but was not relevant in this analysis.

The response of a gas detector, in the form of the electrical signal generated, is generally determined by the energy deposited in the active volume by the detected particle. The amplitude of this signal is (positively) related to the total energy deposited by the particle, if not directly proportional. Its shape, on the other hand, before any shaping applied by the read-out electronics, is influenced by the spatial distribution of this energy deposition within the gas volume, which will determine the charge collection

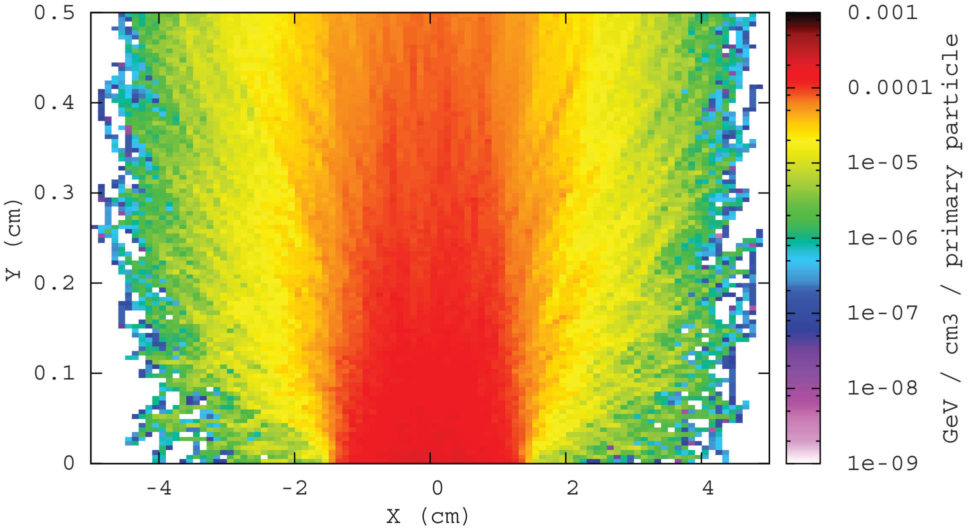

Figure 2.14: *The simulated energy deposition in the detector gas caused by α-particles emitted from a Pu sample (located at $y = 0$). This information was read independently in 100 scoring bins along the y-axis (i.e. the axis of the detector).*

time. To include this effect in the simulations, the gas volume was subdivided into 100 'slices' (scoring bins) along the y-axis and the energy deposition was scored separately in each. Higher-order corrections to the Bethe energy loss formula, such as the Barkas ($\sim Z^3$) and Bloch ($\sim Z^4$) corrections [64], as well as nuclear stopping power are included by default. The spatial distribution of energy deposited in the gas by α-particles emitted from a plutonium sample is shown in figure 2.14 as an example.

2.3.2 Signal reconstruction

The first step in reconstructing the output signal of the detector is to transform the energy deposition in the gas into the number of electron-ion pairs created, since the electrical charge eventually collected in the read-out electrode is the information that the detector actually measures.

It would seem reasonable to approximate the energy deposition required to create one ion pair with the value of the ionisation energy of the gas atoms. Nevertheless, the average energy required to created an electron-ion pair in a gas, known as its *W-value* [65], is generally found to be considerably higher (almost double) than the ionisation energy. The reason for this is that the ionising particle does not only lose energy in the gas through ionisation, but also through excitation of the gas atoms to higher energy states without ionisation. It has been observed that the W-value does not vary greatly between materials or type and energy of the ionising particle. Therefore, and given the composition of the gas mixture used (88% Argon) and the lack of experimental information on the W-values of particular gas mixtures, the known value for Argon was used ($W = 26$ eV). In translating the energy deposition in a scoring bin to charge production, one electron was considered produced for every 26 eV deposited, e.g. no electrons would be created for an energy deposition lower than 26 eV, one electron would be created for an energy deposition between 26 and 52 eV and so forth.

Once the charge produced in each scoring bin has been calculated as described above,

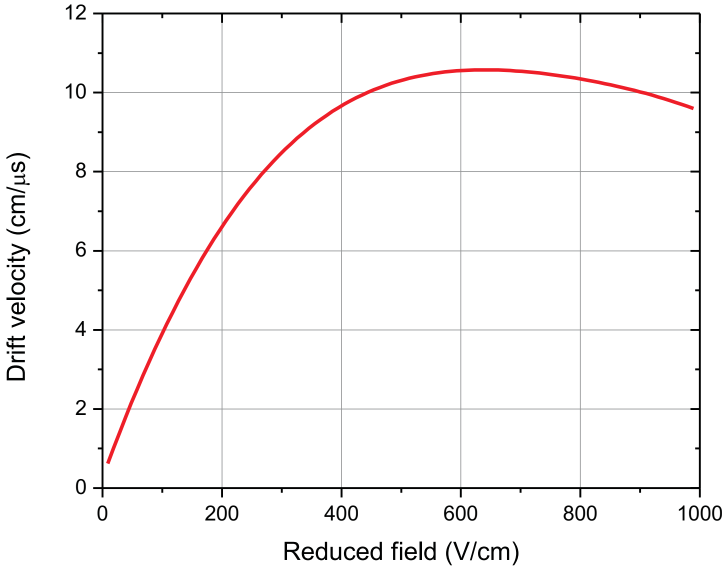

Figure 2.15: *The electron drift velocity in an Ar:CF_4:isoC_4H_{10} gas mixture (88:10:2) at a pressure of 1 bar, as a function of the electric field strength, calculated with the GARFIELD code.*

the movement of the electrons in the gas towards the read-out electrode under the influence of the electrical field needs to be studied. For this, it is necessary to determine the *drift velocity* of the electrons in the gas. It is expected that this quantity will depend on the electric field strength, which is a function of the drift gap and drift voltage applied, and the gas density (or, equivalently, the gas pressure). Indeed, the drift velocity is given by:

$$v_{drift} = \frac{\mu \mathscr{E}}{p} \tag{2.2}$$

where $\mathscr{E}$ is the electric field strength, p is the gas pressure and μ is the *mobility* (in units of m^2·atm/V·s). An in-depth presentation of the theory of electron and ion drift in gases is given by Huxley and Crompton [66].

The electric field strength and gas pressure could be input into the calculations in a straightforward manner. The mobility factor, on the other hand, is dependent on the kind of charged particle (electrons in this case) and the gas, but is generally not known for an arbitrary gas mixture, such as the Ar:CF_4:isoC_4H_{10} mixture used in this detector. To overcome this difficulty and to obtain the drift velocity for this particular mixture, the *GARFIELD* code [67] was used. GARFIELD is designed to simulate drift chambers and can calculate electrical fields in a chamber of nearly arbitrary configuration using finite-element methods, as well as electron and ion drift lines and velocities, and other quantities. Figure 2.15 shows the result obtained for the electron drift velocity in the specific mixture for a pressure of 1 bar, as a function of the electrical field strength. This curve was fitted and used in the code to calculate the correct value of the drift velocity for each drift voltage value that was given as input. It can be seen that, for typical field values (around 500 V/cm), the electron drift velocity in the gas is of the order of 10 cm/μs. With this information at hand, the charge collected as a function of time $Q(t)$ can be calculated using the electron drift time obtained for a given drift gap and drift voltage.

As each charge 'bunch' created in the 100 scoring bins is collected in the read-out electrode, it will cause a response in the read-out circuit that decays exponentially with some time-constant τ_{RC}. The contributions from each bunch will obviously overlap. Therefore, the current that will be read out as a function of time will be:

$$I(t) = \int_0^t \frac{dQ}{d\tau} e^{-\frac{t-\tau}{\tau_{RC}}} d\tau = e^{-\frac{t}{\tau_{RC}}} \int_0^t \frac{dQ}{d\tau} e^{-\frac{\tau}{\tau_{RC}}} d\tau \tag{2.3}$$

Since we are dealing in discrete values, due to the finite binning of the scoring grid, the equation can be rewritten as follows for implementation in the code:

$$I_i = e^{-\frac{t_i}{\tau_{RC}}} \sum_{i=1}^{i=N_{bins}} \left(\frac{dQ_i}{d\tau} \cdot e^{-\frac{t_i}{\tau_{RC}}} \right) \tag{2.4}$$

As a final step, this signal must be shaped, as it would be in a real-life preamplifier. It can be shown that a raw signal passing through a $CR-(RC)^4$ circuit is shaped to a nearly Gaussian form. In this work, a simpler $CR - RC$ circuit was assumed (a differentiator-integrator circuit, see figure 2.12), as it already provides sufficient shaping and is significantly less complicated to implement in code. Indeed, since the preamplifier circuit used in the experiment needed to be quite fast (which means that less shaping is performed on the signal), the actual form of the signals resembles the ones simulated with a $CR - RC$ circuit, rather than a Gaussian.

The response function of a $CR - RC$ circuit (with different time constants for the two components $\tau_1 = R_1C_1$ and $\tau_2 = R_1C_2$) can be calculated as described in Appendix B and, finally, the output signal is given by:

$$V_{out}(t) = V_{in} \cdot \frac{\tau_1}{\tau_1 - \tau_2} \cdot \left(e^{-\frac{t}{\tau_1}} - e^{-\frac{t}{\tau_2}} \right) \tag{2.5}$$

Once calculated, the reconstructed signal is re-sampled at a frequency of 100 MHz (i.e. a 10 ns step) to match the sampling rate of the digitally recorded experimental data.

In all these calculations, certain factors involved, such as the electron charge and the normalisation of the energy deposition to the precise volume, are mere scaling factors, which were therefore irrelevant for this analysis. The gain induced by the electron avalanche and the amplification region of the Micromegas detector is another such factor. Nevertheless, with this last exception, all other factors were included as they did not significantly impact the processing time and kept the results in 'physical' rather than arbitrary units.

2.3.3 Combination of results

Once the code is in place to extract a realistic signal for each simulated event, it is possible to combine several of these signals to create simulated data that resembles the raw data acquired experimentally. First, an appropriate time-window is opened (preferably a few ms long). To increase the realism of the simulation, a white noise signal is created and added by sampling a Gaussian distribution of the desired width. Then, the desired signals can be introduced; for example, signals for α-particles can be added at random positions and in numbers that reflect the actual sample activity.

The artificially generated data can be parsed with the same peak-search routine used for the experimental raw data. In this manner, it is possible to obtain pulse height spectra that can be compared with those obtained experimentally with appropriate scaling and a certain level of smoothing to account for the detector and read-out resolution. Pile-up effects can be studied by placing signals at random positions and then sequentially in well-separated positions and observing the changes in the resulting pulse-height spectra. The comparison of experimental and simulated amplitude spectra can be used to estimate the detector efficiency, as described in more detail in Chapter 3.

Chapter 3

Data analysis and results

The procedure for the off-line analysis of the recorded raw data and the extraction of the desired cross-sections is carried out with an ensemble of analysis routines that were developed as part of this thesis and is described in detail in the present chapter. Different features of the experimental setup that induced unwanted backgrounds in the data required special treatment during the analysis. Furthermore, a hitherto unobserved ageing effect in the detectors negatively impacted part of the measurement. The results obtained are presented and discussed at the end of the chapter.

3.1 Raw data analysis

As described in Chapter 1, the analogue waveform of the detector output is digitised and stored, with the data being compressed on-line with a zero-suppression algorithm. The raw data files are eventually transferred on tape for long-term storage.

The first step in the analysis is the data reduction, i.e. the search for detected events in the detector output. The data from each detector are analysed by means of a routine that determines the signal baseline and the amplitude and position in time of the detected signals, among other quantities. This information is stored in so-called *DST (**D**ata **S**torage **T**ape)* binary files. If a raw data analysis routine, such as the one being described, is already in place, the DST files are produced automatically as soon as the raw data is stored, but they can also be produced later. In the latter case, of course, the time necessary for the operation can be much longer, considering the data need to be retrieved from tape. If necessary, different versions of DST files for the same data can be created in order to optimise and test this routine. The DST file format is obviously not practical for further use. Since the analysis of n_TOF data is widely carried out using ROOT [68], an appropriate conversion program creates a corresponding ROOT file for each DST file.

The analysis of the raw data is complicated by certain features of the experimental setup and by sample-induced backgrounds. These include the baseline oscillation induced by the prompt γ-flash, which is discussed in Section 3.1.2, spontaneous fission events, discussed in Section 3.4.1 and the high α-decay rate of the samples which resulted in a significant signal pile-up probability.

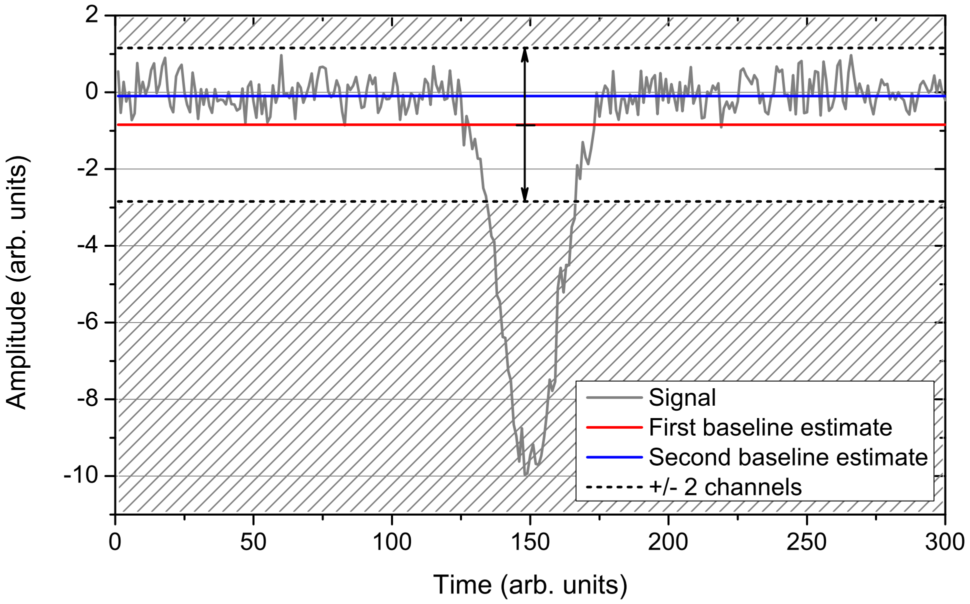

Figure 3.1: *An example to illustrate the operation of the baseline calculation algorithm (details in the text).*

3.1.1 Baseline calculation

The signal baseline is determined by analysing the pre-trigger and post-acquisition window data (512 pre-samples and 2048 post-samples). The simple approach of estimating the baseline as the average value of these channels could be used if analysing data from a low-activity sample. In the case of the plutonium samples, however, signals due to α-particles – and, to a lesser extent, fission fragments produced by spontaneous fission events – are often detected during those several microseconds. These would lead to the estimation of a baseline that is lower than the real one (since the signals are negative).

To correct for this difficulty, a simple iterative algorithm was implemented to obtain the desired result with minimum processing requirements. A first estimate of the baseline was calculated with the straightforward approach of taking the average value of the samples. In the next pass, only the data points within a specified range from the previous baseline estimate were considered, thus excluding any distant values that were part of a pulse, and the average was again taken to calculate the next estimate of the baseline. The width of this range was slowly restricted with each iteration to avoid a quick convergence to a non-optimal value. Once the difference between baseline estimates became smaller than a specified value, the convergence criterion was satisfied and the iterations stopped. In this manner, the value quickly converged to the true baseline within a few iterations, if a signal was present, or just two, if only noise was recorded in the pre- and post-samples. An example is shown in figure 3.1, where a Gaussian signal has been added to white noise whose baseline is at zero amplitude. The average of the full signal (red line) is therefore lower than the real value (around -0.8). In the second iteration, we exclude all points outside a range of 2 units from the first baseline estimate and take the average. The new estimate is already around -0.1.

Alternatively, the baseline could have been calculated in a more sophisticated approach as the zero-frequency ω_0 obtained by a discrete Fourier transform of the data in ques-

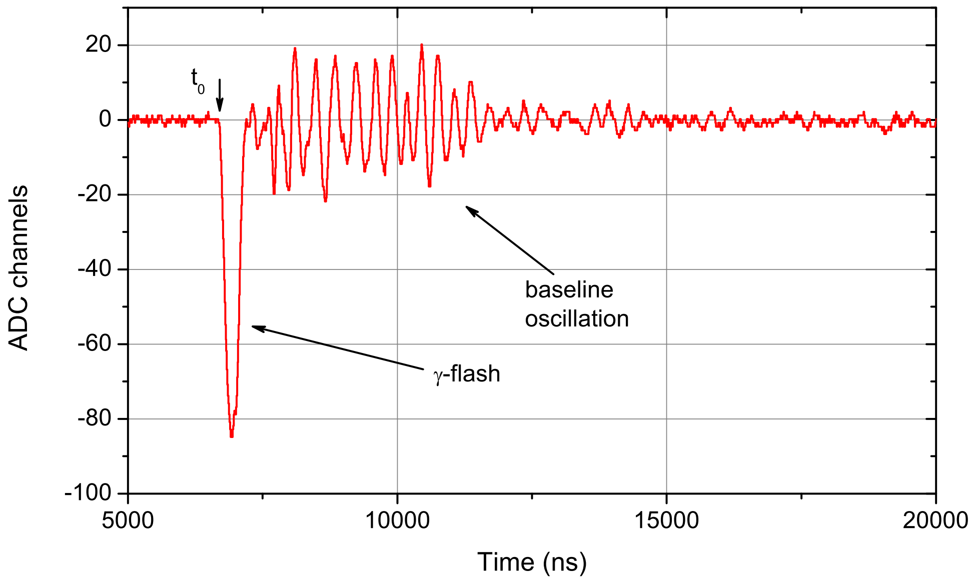

Figure 3.2: *The beginning (first several μs) of a recorded signal. After the pre-trigger channels, the initial γ-flash signal and the baseline oscillations that follow it are clearly visible. The signal baseline has already been estimated and subtracted, as described in the previous section.*

tion, but with larger CPU-cost.

3.1.2 Detector response to the γ-flash

As discussed in Section 2.2.6, the interactions of the proton beam with the spallation target lead to a significant production of prompt γ-rays that reach the experimental area at times-of-flight around 630 ns and constitute the bulk of what is commonly termed the *γ-flash*. Additional contributions are expected from charged particles created near the experimental area, e.g. in the second collimator, by the high-energy fraction of the neutron beam (E_n > 100 MeV). In the present experimental setup, the γ-flash causes an initial signal lasting a few hundred nanoseconds, followed by a baseline oscillation that lasts for several microseconds or, in terms of neutron energy, down to a few MeV, and a frequency of about 3 MHz. The behaviour of the detector signal can be observed in figure 3.2, where the baseline oscillations are clearly visible.

The initial signal is most likely caused by energy deposition in the active volume of the detector by the in-beam photons. Due to the small dimensions (5 mm thickness along the beam direction) and low density of the detector active volume, the interaction probability of a γ-ray is quite low. The number of γ-rays that arrive at prompt times-of flight (*Tof*<1 μs) with each beam bunch, however, are of the order of 10^7, leading to a measurable energy deposition, comparable to a fission fragment, despite the detector's relative transparency to γ-rays.

The oscillation of the baseline is related less to the detector itself and more to the associated electronics, especially the preamplifier. Although its exact origin is still a topic of discussion, it is possibly caused by an electromagnetic wave that travels along the beam-line (coming from the spallation target or, more likely, the second collimator or elsewhere near the experimental area) and is detected as RF-noise in the electronics once it enters the experimental area, which acts as a cavity. This viewpoint is enforced by the fact that the addition of shielding around the preamplifier box, in the form of aluminium foil, helps to reduce the amplitude of the oscillations.

Since the amplitude and width of the oscillations are comparable to those of fission fragment signals, the high-energy limit of the measurement would be limited to a few MeV at most, without some treatment of this noise, as described in the following section. Furthermore, while the time evolution of the oscillations is fairly constant, their amplitude varies with proton intensity, further complicating the analysis.

3.1.3 The high neutron energy region: the 'compensation' method

The problem of the post-γ-flash baseline oscillation can be mitigated by applying a software *compensation* [69] to the digitally recorded data, provided that the amplitude of the oscillations does not exceed the range of the flash-ADC leading to a saturation of the signal. Particular attention was given to avoiding this when setting the range of the digitisers. Although different methods could be used, such as pattern recognition or pulse-shape fitting algorithms, the vast amount of data to process makes a simpler and faster algorithm, such as the one presented here, preferable.

The compensation method is based on the observation that the oscillations recorded in adjacent detectors for the same beam bunch are almost identical. This can be seen by comparing the recorded signals from two detectors placed consecutively in the chamber, such as the example shown in figure 3.3. This is done after the baseline for each signal has been estimated and subtracted and the start times of the γ-flash signal have been matched. This start time also serves as the reference for calculating the corresponding time-of-flight of each detected signal, accounting for the approximately 630 ns required by the photons to reach the detector and initiate the γ-flash signal. The subtraction of the output of adjacent detectors causes the oscillations to largely cancel each other out, leaving a residual signal that consists primarily of signals attributable either to fission fragments or α-particles, along with some residual noise. If a signal is present in the output of the second detector, it appears in the residual signal as a pulse of inverted polarity and can be therefore easily ignored in the analysis. The residual noise has a much lower amplitude than the initial oscillation, but can still determine the selection or rejection of signals with amplitudes very near to the amplitude threshold. Once the signal is cleaned up in this manner, it can be analysed with the same peak-search routine used for the lower energy region to extract the desired pulse height spectra.

The obvious weakness in the performance of this method is the possible interference of real signals from the two detectors. This can be an important effect in the presence of high count-rates, when pulses in the two detectors can completely or partially overlap, cancelling each other out or distorting their respective shape and amplitude. When this is the case, a correction similar to a dead-time correction needs to be applied. For the very low count-rates of the present experiment, however, the probability of a fission signal being present in both detector outputs was very low, much less for them to appear at the same time-of-flight and interfere with each other in the subtraction. This effect was therefore completely negligible and could be safely ignored.

A further difficulty lies in the exact determination of the start time of the γ-flash signal (the t_0 of figure 3.2). If only noise was present in the pre-trigger signals, it would be enough to set a low threshold and look for the first crossing. As explained earlier and

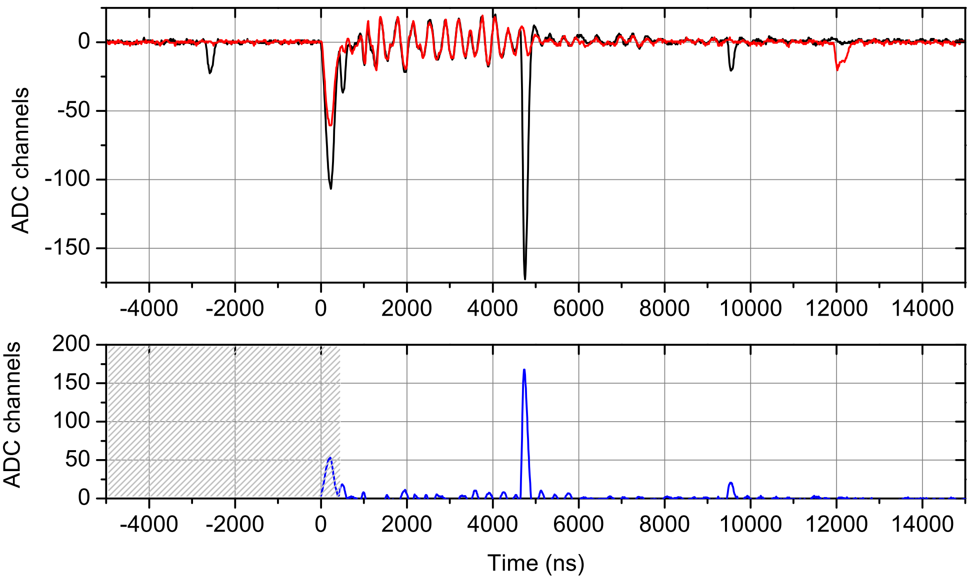

Figure 3.3: *Top: The beginning (first few μs) of the recorded signals during the same proton bunch from two adjacent detectors. The baseline has been subtracted in both cases and the start times have been matched. Although the amplitude of the γ-flash signals is different, the baseline oscillations are nearly identical. Bottom: The residual signal after the subtraction of the two signals. The oscillation is almost entirely suppressed, but a small residual signal usually remains. The shaded area marks the limit for signal detection, which can start only after the γ-flash signal has completely ended.*

as can be seen in figure 3.3, sample-induced signals are often present in the pre-trigger data, while the amplitude of the γ-flash signal is not always very high, making the selection of an appropriate threshold quite difficult. For this reason, data from 'parasitic' (low intensity) protons pulses, where the γ-flash signal is generally much lower, were not used for the high-energy analysis. This was also the case for data acquired during the short periods when thick tungsten, lead and other filters that strongly reduced the in-beam photon flux – and, therefore, the amplitude of the γ-flash signal– were present in the beam as auxiliary samples for capture measurements.

3.1.4 The peak-search routine

Once the baseline has been estimated (and the baseline oscillations are removed, if we are dealing with the high-energy region), the data is parsed with a pulse recognition routine. The routine is a slightly simplified implementation of the Mariscotti peak-identification algorithm [70], which is commonly used in spectrometry applications.

The implemented algorithm first looks for data that exceed a set threshold (relative to the baseline). At a minimum, this threshold is chosen to be just above the electronic noise, which is found to have values of ± 2-3 channels with respect to the baseline. In practice, choosing a threshold higher by a few channels, e.g. equal to 10, helps to reject a large number of signals with a very low amplitude that would also be well below the amplitude threshold for fission events applied later, reducing the processing time and keeping the size of the produced files at a reasonable size.

Upon detecting a threshold crossing, the routine searches for a peak by looking for the

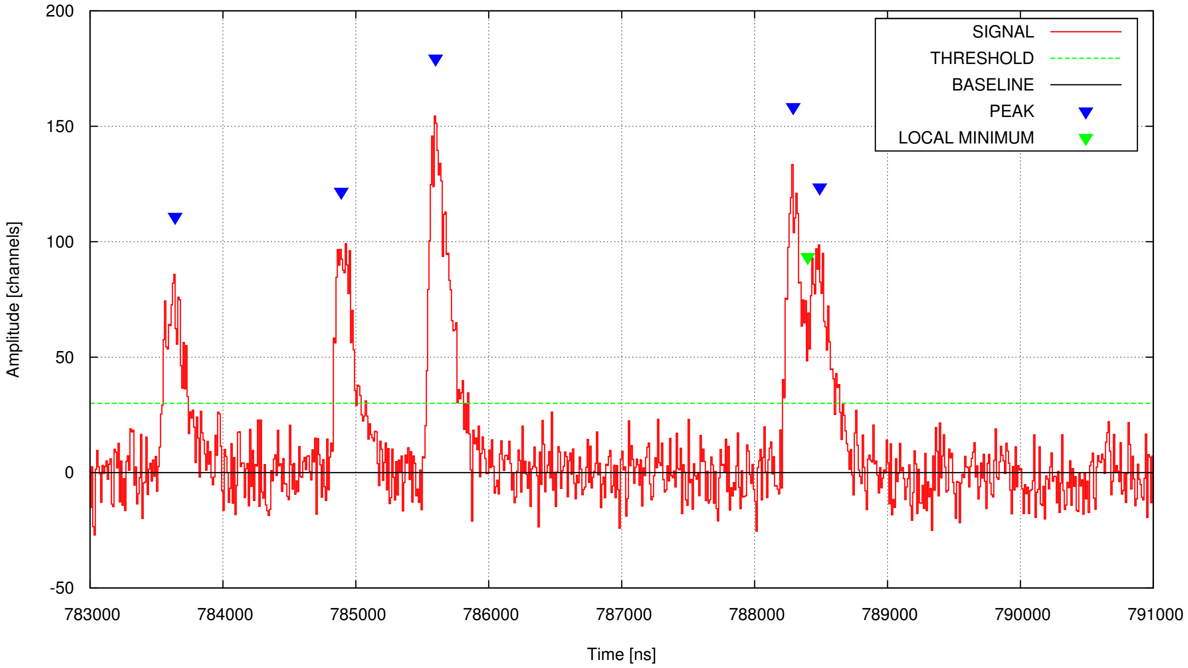

Figure 3.4: *An example of the performance of the peak-search routine on an artificially generated signal. By looking for local minima after a peak, the routine is able to discriminate between partially overlapping signals.*

appropriate sign change of the smoothed first derivative of the data. Having identified the position of the peak, and therefore also its amplitude, it looks for the baseline crossing of the falling signal after it to determine the total width, calculates the FWHM (Full Width at Half-Maximum) and integrates the data between the start and end of the peak to obtain the area, which is proportional to the collected charge.

Given the high activity of the samples, however, the probability of pulse pile-up is not negligible. The routine needs to be able to discriminate between partially overlapping pulses. To this end, upon detection of a peak, the routine searches for local minima after it by looking for the appropriate sign change of the smoothed second derivative of the data. A local minimum after the peak indicates that another event was detected before the signal from the original peak was able to fall below the threshold. The routine then looks for this second peak as before and proceeds in the same manner until the signal does fall below the threshold, where from it continues reading the data looking for the next threshold crossing. An example is given in figure 3.4 using signals artificially generated from simulations of the detector, as described in Section 2.3. The signals are placed at random positions and white noise is added. The peak-search routine easily locates individual peaks, but is also able to discriminate adjoining peaks, when a local minimum is present between them. Furthermore, by looking at the smoothed derivatives of the signal, as opposed to derivatives calculated channel-by-channel, the routine safely ignores small 'fake' peaks caused by the electronic noise, such as those visible around the peak of the first signal from the left or the fall of the third signal.

For each detected peak, the most important quantities to determine are its amplitude and position, which determines the corresponding neutron time-of-flight. As explained above, the amplitude is relatively straightforward to obtain, once the peak has been detected. Due to the presence of nearby overlapping signals, however, the exact start time of a peak is not always easy to accurately determine. In the ideal case when signals are well separated from each other, it is possible to determine the start time as soon as the signal rises above the noise or, conventionally, when it reaches 20% of its amplitude. Due to high α-activity of the samples, this is often not possible, as the start of a fission signal can be masked by an α-induced signal.

Besides this evident difficulty, however, there is one additional consideration that suggests an alternative approach to determining the desired time-of-flight. This is because the shape of the signals is generally not constant. Indeed, although the fall of the signals, which is directly related to the time-constant of the associated electronics remains almost identical from signal to signal, the rise of the signals is much more variable. This can be explained by considering the geometry of the sample-detector setup and the charge collection mechanism. A fission fragment emitted parallel to the detector axis, will very likely traverse the entire drift gap depositing energy (and creating ionisation electrons) along its path. In such a case, charge collection begins immediately with the charge created near the micromesh and ends when the charge that was created immediately outside the sample is collected. This implies a charge collection time that is equal to the maximum electron drift time in the drift gap and, therefore, a relatively longer rise-time of the signal. If, on the contrary, a fission fragment is emitted at a small angle with respect to the sample plane, it is likely to stop before reaching the micromesh and will not deposit energy in the full depth of the drift gap. The total charge will therefore be collected within a shorter time and the rise of the signal will be faster.

This can be confirmed by simulations, using the signals generated as described in Section 2.3. The effect of the emission angle was studied by generating fission fragments first with an emission angle of 0° with respect to the beam axis (i.e perpendicularly to the sample surface) and then with an emission angle of 80° with respect to the beam axis (i.e. 10° relative to the sample surface). While the fall time of the signals is always the same, the rise-time distribution changes considerably, as shown in figure 3.5. Signals created by forward-emitted fission fragments have a narrower distribution around longer rise-time values. The distribution for laterally emitted fission fragments is wider with a tail towards faster rise-times. This is the expected result based on the considerations of the previous paragraph.

It is evident, therefore, that using the start time of the signal, even if it could be accurately determined, may lead to an overestimation of the time-of-flight due to this delay between the fission event and the start of the charge collection. To deal with this effect, it is rather more appropriate to consider the time of the real event as a fixed offset before the peak maximum. This offset corresponds to the maximum drift time of electrons in the drift region of the detector, which is travelled by the electrons created near the sample surface that need to traverse the entire 5 mm drift gap. For a drift velocity around 10 cm/μs (see figure 2.15) this takes around 50 ns.

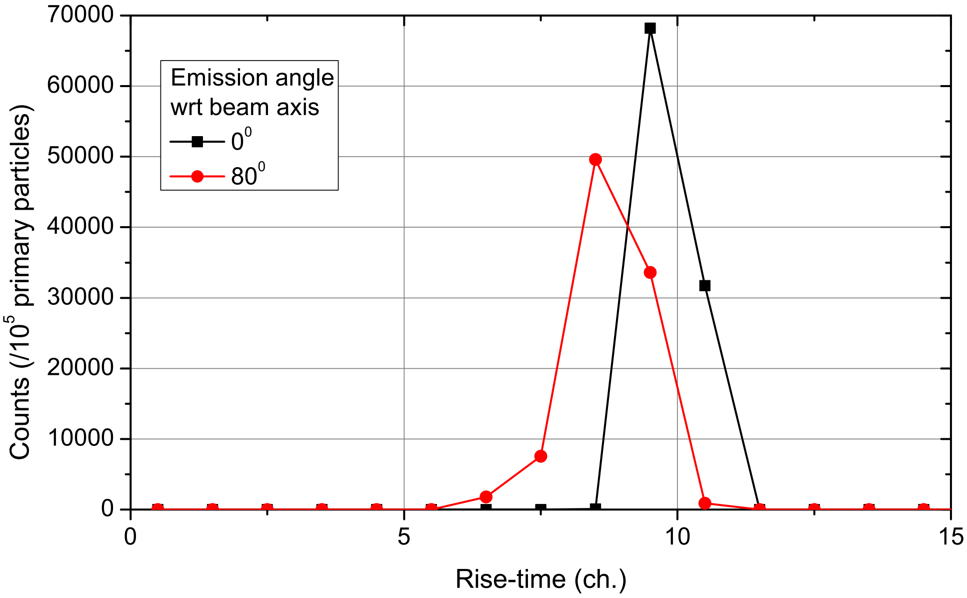

Figure 3.5: *Rise-time of simulated fission fragment induced signals for fragments emitted at 0° and 80° with respect to the beam axis. Since the energy deposition by laterally emitted fragments is generally localised nearer to the sample and not in the full depth of the drift region, the charge is collected in a shorter time period leading to shorter rise-times.*

3.2 Data processing, visualisation and selection

As explained earlier, once the raw data has been analysed, the information collected is stored in the DST files, which are then converted to the ROOT format. In addition to the information extracted by the raw data analysis routine on individual signals, these files also contain certain general acquisition parameters necessary for the identification of the data included in each file. In particular, the information contained in the DST/-ROOT files for each signal includes the:

- run number
- event number
- proton pulse type (dedicated or parasitic)
- proton pulse intensity
- detector ID number
- baseline of the detector output
- signal amplitude
- FWHM of the signal
- total width of the signal
- signal area
- neutron time-of-flight
- corresponding neutron energy

A *run* comprises the data stored during a particular acquisition period. The duration of this period is almost arbitrary and is chosen to keep the file sizes at a more manageable level. A run generally lasts a few hours, depending on the amount of beam being received and the amount of data recorded in the detectors. Rather counter-intuitively, the *event number* is simply a counter increasing by one for each proton pulse ('event') and does not refer to actual detected events. Finally, the neutron energy value included in the DST/ROOT files is just a first estimate, calculated in a straightforward manner, simply accounting for the geometrical distance from the spallation target and is only included to allow for a preliminary check of the data soon after it is recorded and before the detailed analysis. The data stored for each of the above quantities can be visualised individually or in any desired combination.

The second step of the analysis is to extract the quantities that are necessary for the quality check of the data and the cross-section calculation. This is accomplished by means of another custom routine which handles the visualisation of the data and includes the specified criteria for the selection of fission events.

3.2.1 Data processing and visualisation

The data visualisation and selection routine, written in the ROOT environment, includes several histogram definitions for the desired data projections. For each detector, the routine creates a signal amplitude spectrum, distributions of amplitude vs. neutron energy, FWHM and signal area, and time-of-flight distributions. Furthermore, proton pulse type and intensity distributions are also created. Once the selection criteria are set, the routine applies them to the data and creates histograms with the fission counts vs. neutron energy, which are the primary ingredient for the cross-section calculation. The routine can handle beam-on and beam-off runs with the appropriate flag. Once the various histograms have been defined and filled with the data from the DST files, these projections can be plotted and the different parameters of the experiment studied.

Neutron energy binning

Whenever the neutron energy is a parameter in one the above-mentioned distributions, it is necessary to define an energy binning. The choice of the binning is very important and represents a balance between the energy resolution required to observe particular features, such as resonances, that require a fine binning, and the level of statistics, which may impose a coarser binning when the number of detected events is low. Of course, the binning can vary between different energy ranges; a finer binning can be used in the resonance region compared to the region above the fission threshold, where the behaviour of the cross-section is much smoother.

Aside from these considerations, it is also important to choose an energy binning that facilitates the visualisation and analysis of data that span several orders of magnitude in neutron energy. Obviously, using energy bins of equal width would lead either to very wide bins at low energies or very narrow ones at high energies. To address this issue, the neutron energy range is subdivided into bins of equal logarithmic width w, meaning that for any energy bin with a lower and upper energy limit of E_i and E_{i+1} respectively:

$$\log E_i + w = \log E_{i+1} \tag{3.1}$$

This is called *isolethargic* binning and is discussed in detail in Appendix A. If E_{min} and E_{max} are the limits of the energy range being studied and N_{bins} is the number of bins in this interval, then the (logarithmic) bin width w is:

$$w = \frac{\log E_{max} - \log E_{min}}{N_{bins}} \tag{3.2}$$

For example, a bin width $w = 0.01$ defines a binning of 100 bins (of equal logarithmic width) per neutron energy decade.

Time-to-energy conversion

The time-to-energy conversion, i.e. the accurate determination of the neutron energy corresponding to an individual detected event, is carried out as described in Section 1.1.3, by means of the iterative procedure that makes use of the simulated $\lambda(E_n)$ distribution of the neutron moderation length. In doing so, the geometric distance from the target L_{geom} needs to be fine-tuned; this can be accomplished by choosing the value that better reproduces the well-known resonance energies of ^{235}U. Depending on the time-of-flight, calculations are made using the classical or relativistic formulae below and above a defined cut-off. For this analysis, the relativistic formulae were used for neutron energies above 0.1 MeV. The obtained neutron energy value replaces the preliminary one included in the DST file.

3.2.2 Fission events selection

The most important distributions created with the data selection routine are the amplitude (pulse-height) spectra and the amplitude vs. neutron energy distributions for each detector. These distributions are essentially the same, since the amplitude spectrum is merely a projection of the amplitude vs. E_n distribution over a specific energy range. Fission events are selected with a signal amplitude threshold, which needs to be defined by balancing between the need to reject background (e.g. signals from α-particles) and to include as many of the fission signals as possible.

An example of amplitude vs. E_n distributions is shown in figure 3.6, where two very different cases are presented. On one hand, the distribution obtained from the ^{235}U sample (top) reveals, as expected, that the α-particle background is quite low (the sample activity is 0.54 kBq), while the fission count-rate is quite elevated. By comparison, the distribution obtained from one of the ^{242}Pu samples shows a much higher α-background (the sample activity is ~130 kBq) and a lower fission count-rate due to the lower fission cross-section. It is not immediately evident from these two distributions that there is a significant spontaneous fission component in ^{242}Pu which is not present in ^{235}U and which is discussed later.

The amplitude vs. neutron energy distributions represents an overview of the data. This information can be condensed in a simple amplitude spectrum. The corresponding pulse-height spectra for ^{235}U and ^{242}Pu are shown in figures 3.7 and 3.8 respectively. The sudden cut-off below 10 channels is applied to reduce the size of the ROOT files by avoiding to include a very large number of very low amplitude signals that would

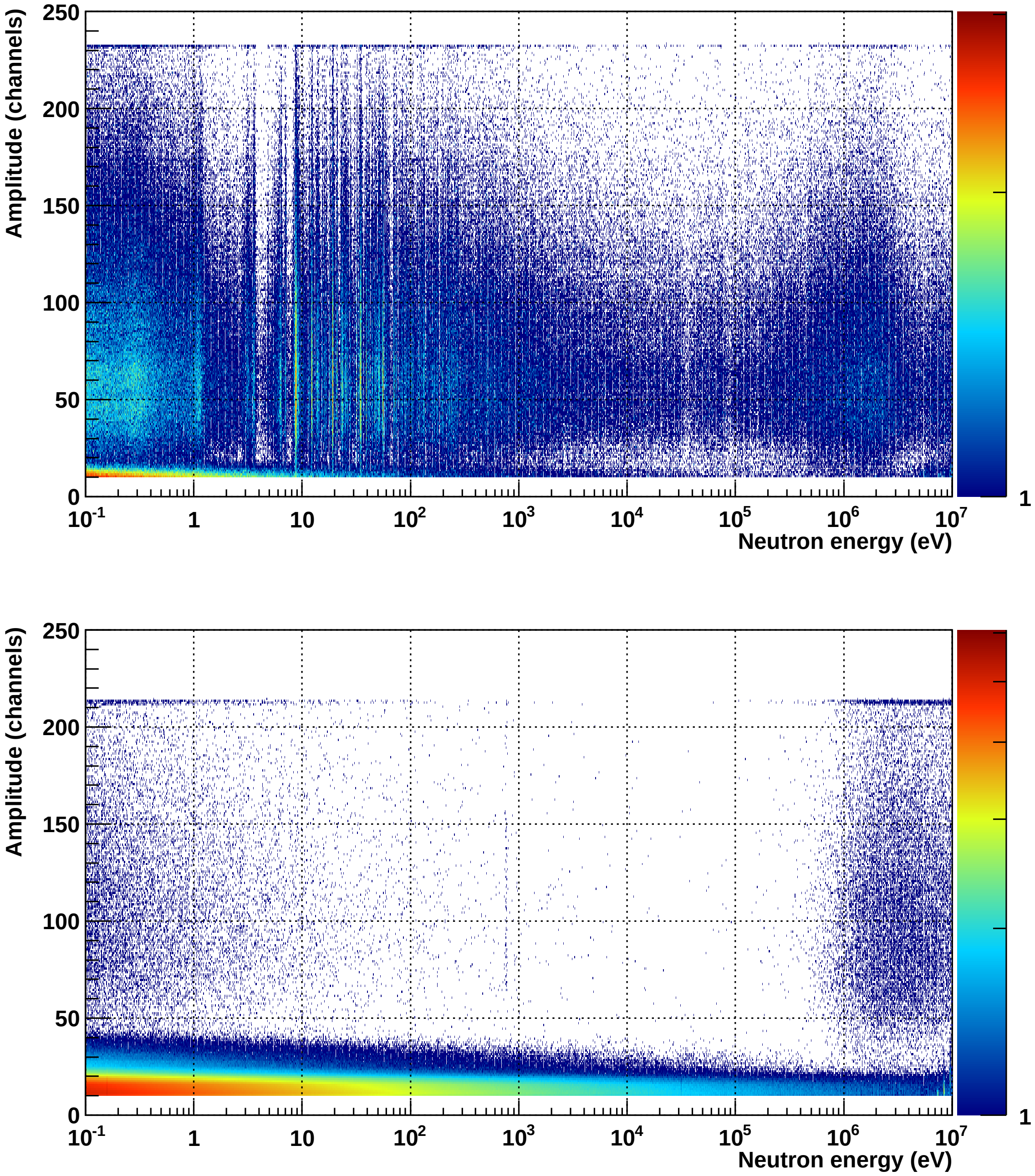

Figure 3.6: *Amplitude vs. neutron energy distributions, with an energy binning of 2000 bins per energy decade. Top: The distribution obtained from the* ^{235}*U sample. Bottom: The distribution obtained from one of the* ^{242}*Pu samples. The difference in the* α*-activity is evident, as is the difference in the absolute value of the cross-section for low-energy neutrons.*

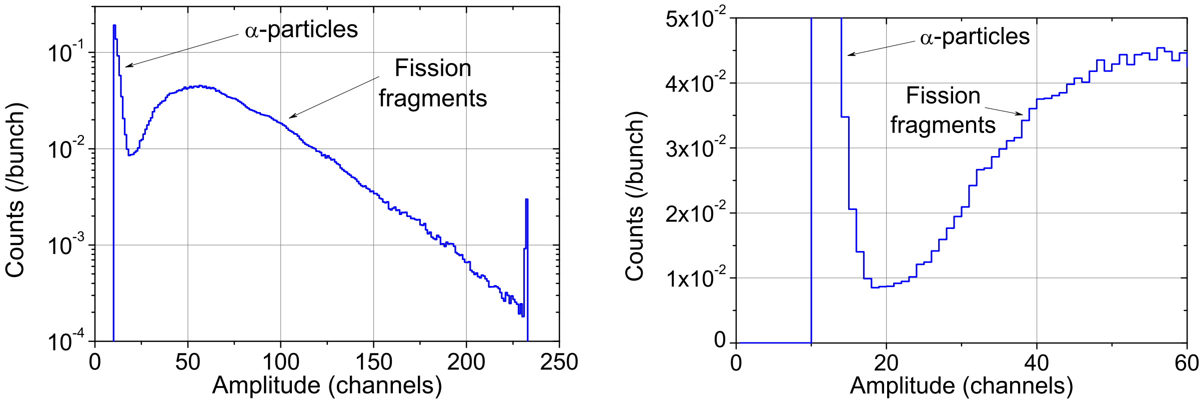

Figure 3.7: *Left: Amplitude spectrum obtained from the ^{235}U sample. Right: The same spectrum, focused on low amplitude values so that the quality of the separation between α-particles and fission fragments can be better observed.*

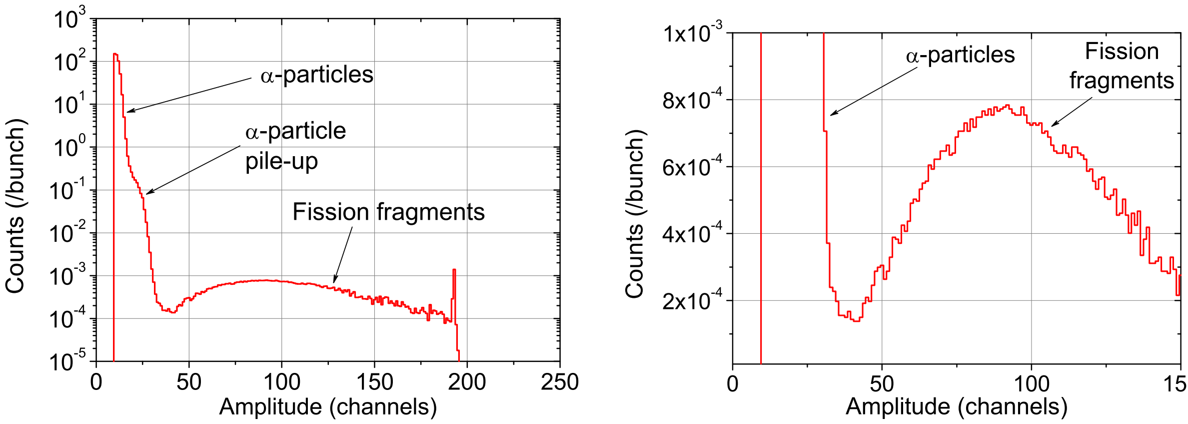

Figure 3.8: *Left: Amplitude spectrum obtained from a ^{242}Pu sample. Right: The same spectrum, focused on low amplitude values, so that the quality of the separation between α-particles and fission fragments can be better observed. The much higher α-background compared to ^{235}U is evident, as is the pile-up tail that 'invades' the separation 'valley' between α-particles and fission fragments.*

be surely rejected in the analysis, although they were included in the early stages of testing of the pulse-recognition routine.

Although the bulk of the α-article and fission fragment amplitude distributions can be clearly separated, the choice of a specific amplitude threshold is not equally straightforward. For any threshold chosen, it needs to be possible to estimate the fraction of fission fragment signals rejected and the number of α-particle signals included. The final choice was to select an amplitude threshold high enough to reject all α-particle signals. Since this is still well before the bulk of the fission fragment signals, only a small percentage of fission events is rejected, which becomes the sole correction that needs to be calculated, since the fraction of α-particle signals selected is zero.

After choosing and applying an amplitude cut to the data from each detector, we can obtain histograms with the fission counts vs. neutron energy. Figure 3.9 shows fission yields from ^{235}U (top) and ^{242}Pu (bottom). The resonance structure of the ^{235}U cross-section is already visible in the data. Some resonances are also visible in the ^{242}Pu data, but the most prominent feature is a constant background that seems to dominate at low neutron energies. This background is due to spontaneous fission events and is discussed in Section 3.4.1.

Finally, all the histograms created are saved in an output ROOT file. Each such file contains data from a single run. In the ideal situation when the detector performance is perfectly stable, all these files could be merged and the cross-sections extracted from a single file containing the full statistics. For a several months long experiment, this stability is generally difficult to achieve. As explained in Section 3.3, however, there was one additional reason why this condition was not met in this particular experiment.

3.3 Sample-induced damage to detectors

An unexpected effect of the high α-activity of the samples (>6 MBq per sample for ^{240}Pu) was encountered in the course of the measurement, with a steady degradation of the fission fragment amplitude distribution. After the end of the measurement, a visual inspection of the detectors used with the ^{240}Pu samples revealed the source of the problem: as shown in figure 3.10 (left panel), an obvious circular discolouration of the mesh whose dimension and position exactly matched those of the samples was observed. Upon closer inspection with a microscope (right panel), it became clear that the micromesh had suffered serious mechanical damage, particularly around the rims of the holes which were evidently deformed (see for comparison figure 1.9, showing an undamaged micromesh).

The damage suffered by the detectors must lead to a deterioration of the electrical field near the micromesh holes and therefore of the detector gain and overall performance. Indeed, this was clearly observed in the ^{240}Pu data, where fission fragment and α-particle signals eventually became virtually indistinguishable in the obtained pulse height spectra during the course of the measurement, as shown in figure 3.11a. Because of this, a considerable part of the ^{240}Pu data must be discarded, compromising the measurement. It is worth noting that, even when the detectors were operating normally, the long α pile-up tail greatly reduced the quality of the separation. This would either require using a very high amplitude threshold, strongly reducing statistics, or attempting to characterise the α-background from the beam-off data and subtracting it, with the obvious disadvantage that the final fission counts would be the result of the cancellation of two very large numbers, leading to a significant uncertainty.

Although the damage to the detectors was not as obvious, a similar but less pronounced effect was observed in the ^{242}Pu data, as a slow but non-negligible gain shift throughout the duration of the measurement, as shown in figure 3.11b. The data, therefore, had to be analysed in smaller subsets where the gain could be considered constant.

For the above reasons, results on ^{242}Pu only are presented in this thesis. The ^{240}Pu(n,f) measurement is planned to be repeated at n_TOF's new Experimental Area II (EAR-2), where the increased neutron intensity will reduce the duration of the measurement, thus avoiding the degradation of the detector over the long period that was observed in EAR-1 [71]. Furthermore, since EAR-2 is placed at the end of an 18 m flight-path, about 10 time shorter than the flight-path to EAR-1, the acquisition windows will be correspondingly shorter, substantially improving the signal-to-background ratio (since the background is mainly related to the very large α-activity of the samples).

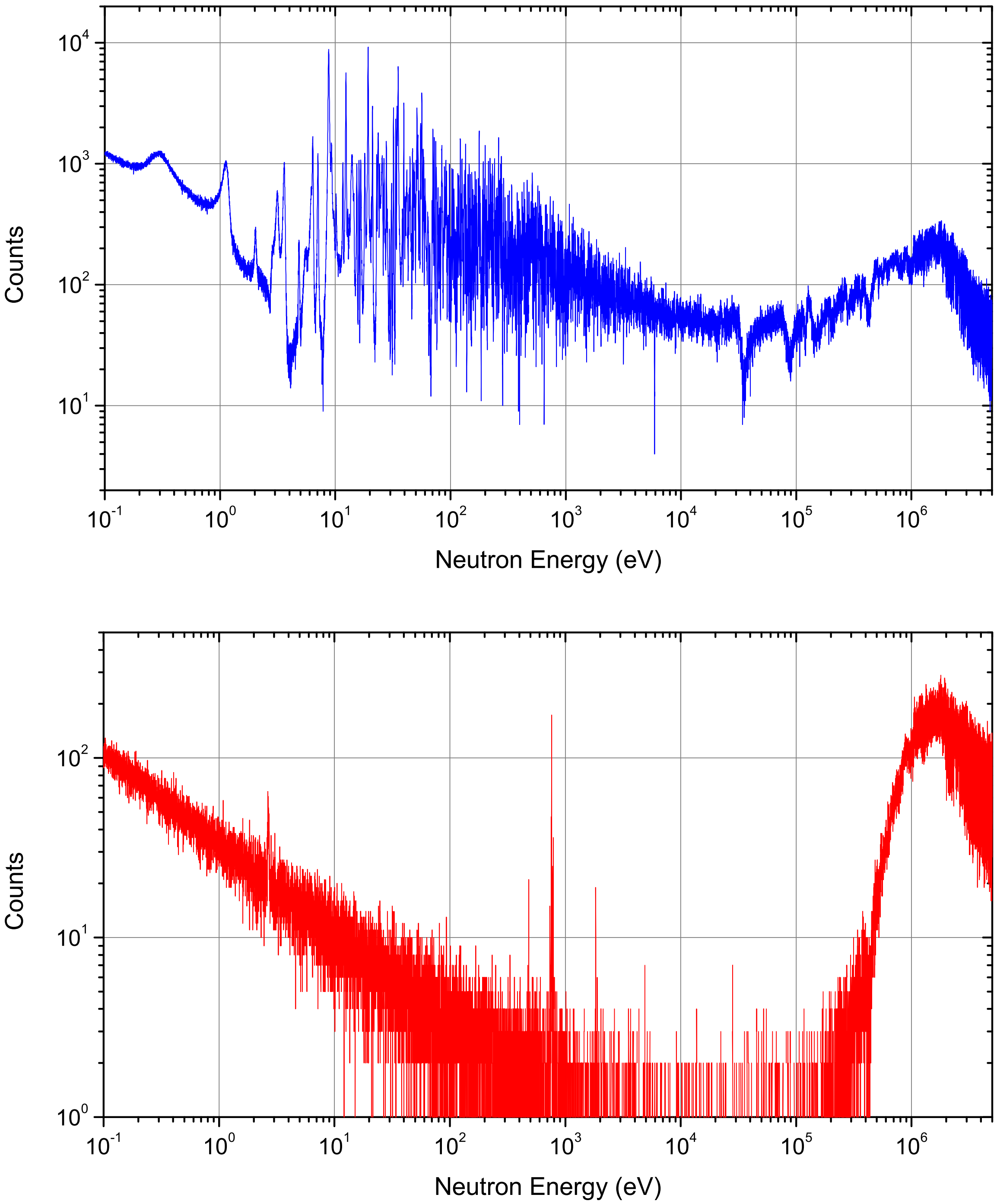

Figure 3.9: *Fission counts vs. neutron energy at 2000 bins per energy decade obtained from* ^{235}*U (top) and* ^{242}*Pu (bottom). The resonance structure of the* ^{235}*U(n,f) cross-section is visible. Some resonances are visible in* ^{242}*Pu, but a constant background is prominent, particularly in the low energy region.*

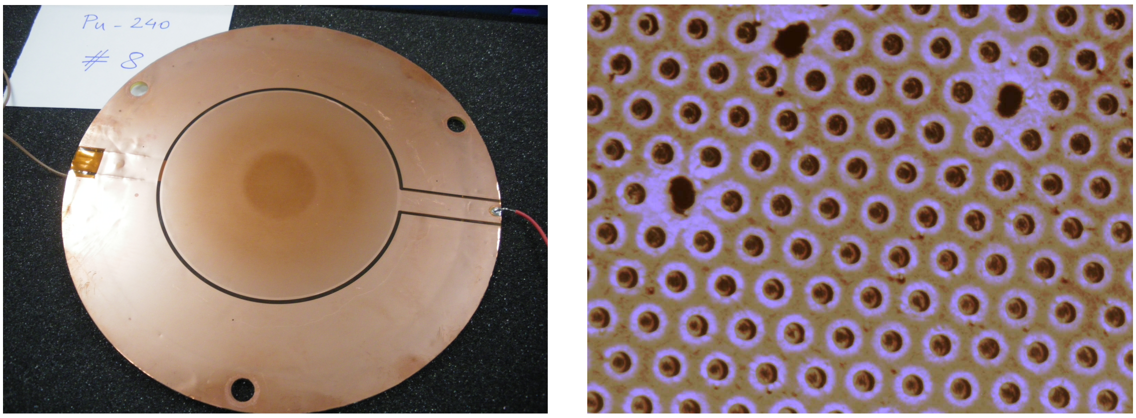

Figure 3.10: *Left: One of the Micromegas detectors used with a* ^{240}*Pu sample pictured after the end of the measurement. A 3 cm diameter discolouration is visible on the micromesh. Right: Picture of the micromesh taken with an electronic microscope (courtesy A. Teixeira, CERN). Mechanical damage around the rims of the holes can be observed, in addition to localised severe damage around some holes. This leads to a severe deterioration the electrical field and therefore of the detector gain and performance.*

3.4 Cross-section calculation

After processing the data as described in Section 3.2, fission yields (fission counts vs. neutron energy) have been obtained for each isotope. These are the main ingredient for the cross-section calculation. Finally, the ^{242}Pu(n,f) cross-section is calculated relative to the ^{235}U(n,f) cross-section according to:

$$\sigma(E_n) = \frac{N(E_n) - N_{sf}(E_n)}{N_{ref}(E_n)} \cdot \frac{\varepsilon_{ref}}{\varepsilon} \cdot \frac{f_{c,ref}}{f_c} \cdot \frac{n_{ref}}{n} \cdot \sigma_{ref}(E_n) - \sum_i a_i \cdot \sigma_i(E_n) \tag{3.3}$$

In the above equation, N are the recorded counts, ε is the detector efficiency, understood as the fraction of fission fragments that exit the sample deposit and enter the active volume of the detector, f_c is the correction factor for the amplitude threshold applied to the data (i.e. the fraction of detected fission fragments above the threshold) and n are the areal densities of the samples. The last term subtracts the contribution from sample impurities and a_i are the relative abundances of contaminants in the sample, multiplied by the corresponding cross-sections. The spontaneous fission counts are marked as N_{sf} and are subtracted from the total fission counts. The subscript 'ref' refers to the respective quantities corresponding to the reference isotope, in this case ^{235}U. The areal density n in atoms per barn can be obtained from the known areal density ρ_A in g/cm^2 as:

$$n = 10^{-24} \frac{[\mathrm{cm}^2]}{[\mathrm{b}]} \frac{N_A \cdot \rho_A}{A_r} \tag{3.4}$$

Calculating the cross-section relative to a reference reaction eliminates systematic uncertainties related to the determination of the n_TOF neutron flux and also to the use of the beam interception factor obtained from simulations to correct the flux with the fraction of the beam actually intercepted by the samples.

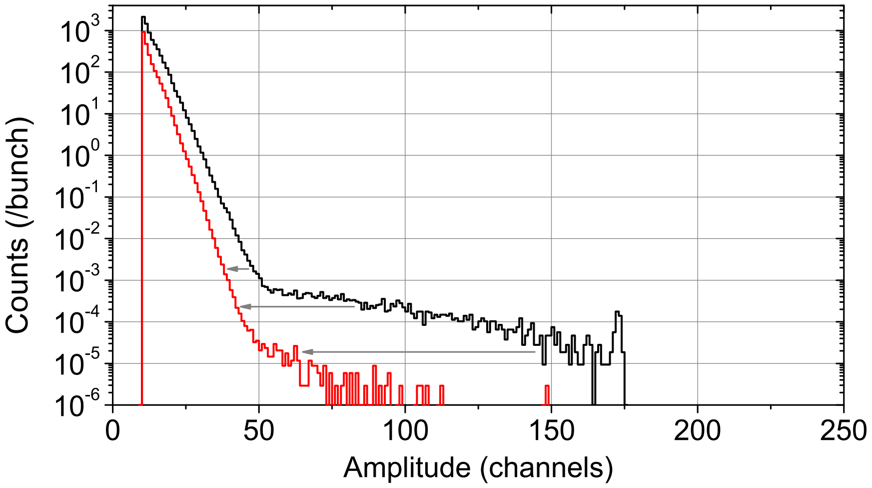

(a) *Amplitude spectra obtained from one of the ^{240}Pu samples at the beginning of the measurement (black line) and a few months later (red line). It is evident that the gain of the detector has decreased and the resolution has deteriorated to such an extent that there is no longer any separation between α-particles and fission fragments. Even at the beginning, the long pile-up tail made the analysis significantly more difficult.*

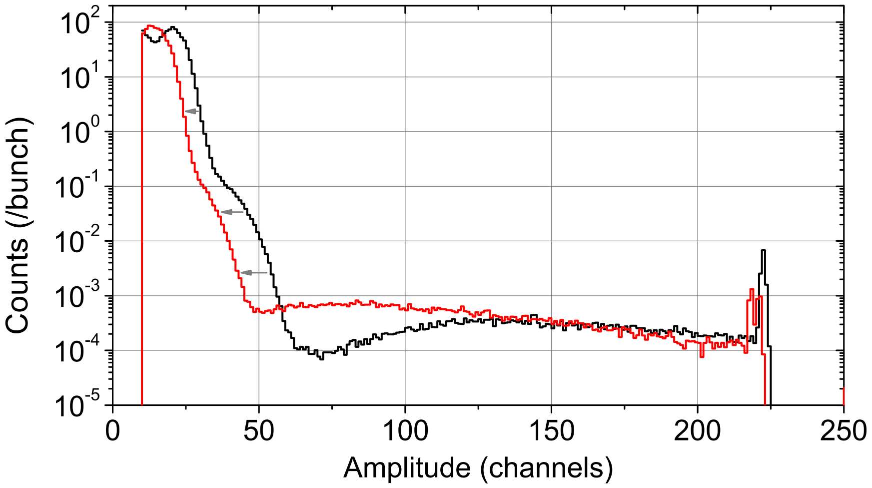

(b) *Amplitude spectra obtained from one of the ^{242}Pu samples at the beginning of the measurement (black line) and near the end (red line). A slow gain drift is observed with a corresponding slight deterioration of the α-particle and fission fragment separation, which, however, can be dealt with by analysing the data in smaller subsets.*

Figure 3.11: *Examples of the gain drift observed in detectors associated with a ^{240}Pu sample (a), and a ^{242}Pu sample (b).*

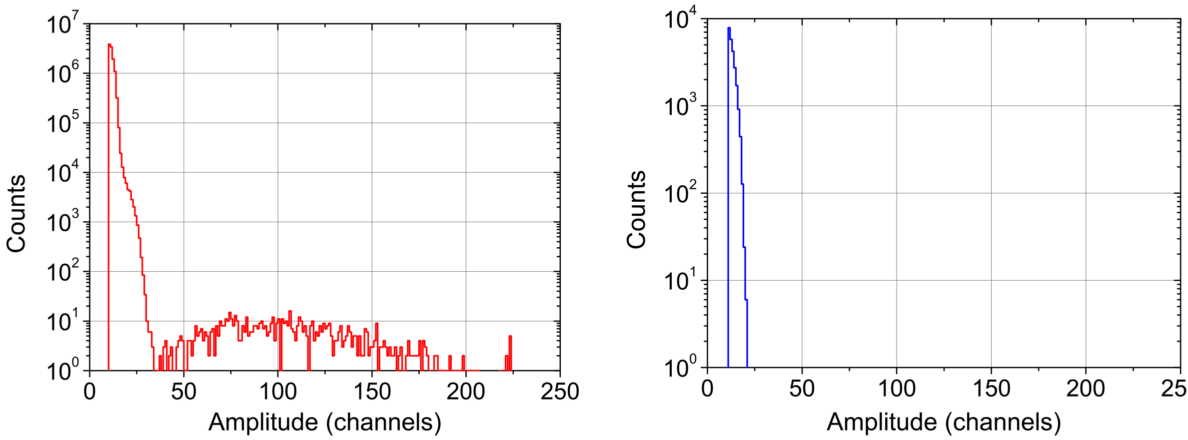

Figure 3.12: *Left: Beam-off amplitude spectrum obtained from one of the ^{242}Pu samples. Spontaneous fission events can be clearly observed. Right: By comparison, no spontaneous fission events are recorded from the ^{235}U sample in the same time.*

The spontaneous fission counts N_{sf} are subtracted as explained in Section 3.4.1, where backgrounds due to sample impurities are also discussed, while the detector efficiency and the amplitude threshold correction are discussed in Section 3.4.2.

3.4.1 The spontaneous fission background and sample impurities

The branching ratio for spontaneous fission in ^{242}Pu is $5.5{\times}10^{-4}\%$ ($T_{1/2,sf} = 6.8 \times 10^{10}$ y). Recent high-accuracy measurements of the spontaneous fission half-life of ^{242}Pu performed at IRMM have confirmed these values with a result of $T_{1/2,sf} = 6.74 \times 10^{10}$ y (1.3%) [72]. Given the activity of the samples, we can expect an average of 0.03 spontaneous fission counts per sample per bunch (i.e. per 80 ms acquisition window). Considering that a single run (a few hours of data taking) can consist of a few thousand bunches, a significant number of spontaneous fission events is certain to be observed. That this is the case can already be seen in figure 3.9 (bottom), but can be observed directly in the beam-off data shown in figure 3.12, where fission events are obviously present in the ^{242}Pu data despite the absence of the neutron beam. In order to proceed with the analysis, this background needs to be properly characterised and subtracted.

Since the spontaneous fission rate is constant, so that $\frac{dn_{sf}(t)}{dt}$ = const., it follows that the number of spontaneous fission counts per neutron energy bin will be proportional to the equivalent $\Delta t_i = t_i - t_{i+1}$. Starting with equation 1.1 and solving for time we obtain:

$$t = L\sqrt{\frac{m}{2}}\frac{1}{\sqrt{E_n}} \tag{3.5}$$

We can therefore express time as a function of the logarithm of the energy:

$$t \propto \frac{1}{\sqrt{E_n}} = E_n^{-1/2} = e^{\ln E_n^{-1/2}} = e^{-\frac{1}{2}\ln E_n} = e^{-\frac{\ln 10}{2}\log E_n} \tag{3.6}$$

Using equation 3.6, the time width Δt_i of an energy bin can be expressed as:

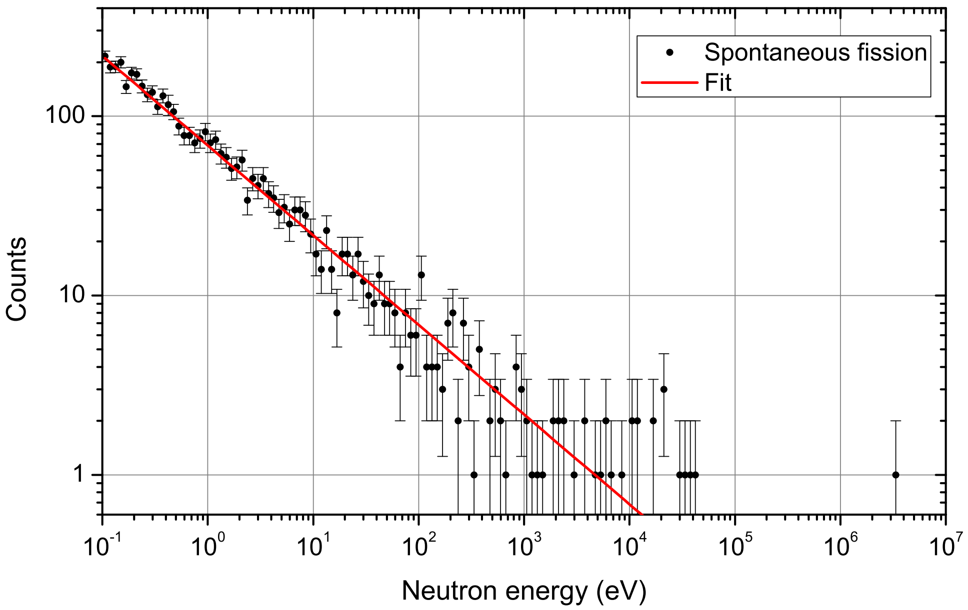

Figure 3.13: *Beam-off fission counts from ^{242}Pu and the fitting curve calculated as described in this section.*

$$\begin{aligned} \Delta t_i = t_i - t_{i+1} &\propto e^{-\frac{\ln 10}{2}\log E_i} - e^{-\frac{\ln 10}{2}\log E_{i+1}} \\ &\overset{3.1}{=} e^{-\frac{\ln 10}{2}\log E_i} - e^{-\frac{\ln 10}{2}(\log E_i + w)} \\ &= (e^{-\frac{\ln 10}{2}w} - 1)e^{-\frac{\ln 10}{2}\log E_i} \Rightarrow \\ \Delta t_i &\propto e^{-\frac{\ln 10}{2}\log E_i} \end{aligned} \tag{3.7}$$

We can therefore fit the spontaneous fission background data with a curve of the following form:

$$S.F.(E_n) = a \cdot e^{-\frac{\ln 10}{2}\log E_n} = a \cdot e^{-1.15129\log E_n} \tag{3.8}$$

where a is the sole fitting parameter which expresses the normalisation to the duration of the acquisition of the beam-off data.

Once obtained using the beam-off data, the background fit is normalised to the number of beam-on events, along with a correction for the different energy binning, since the background is generally treated with a coarser binning due to the lower statistics and to the fact that its behaviour is smooth and well-understood. An example of the fit is shown in figure 3.13. Finally, the background fit is subtracted from the fission counts (shown in figure 3.9), leaving only the neutron-induced fission events.

In order to confirm that the spontaneous fission background dominates in the low energy region, except where visible resonances are present, the fitting procedure was repeated using beam-on data below ~2 eV (the first resonance is at 2.7 eV). If significant contributions from neutron-induced reactions in the sample were present, the fitting parameter should be different than the one obtained from the beam-off data. This was not the case, as the values were practically identical. In Figure 3.14, the ^{242}Pu fission

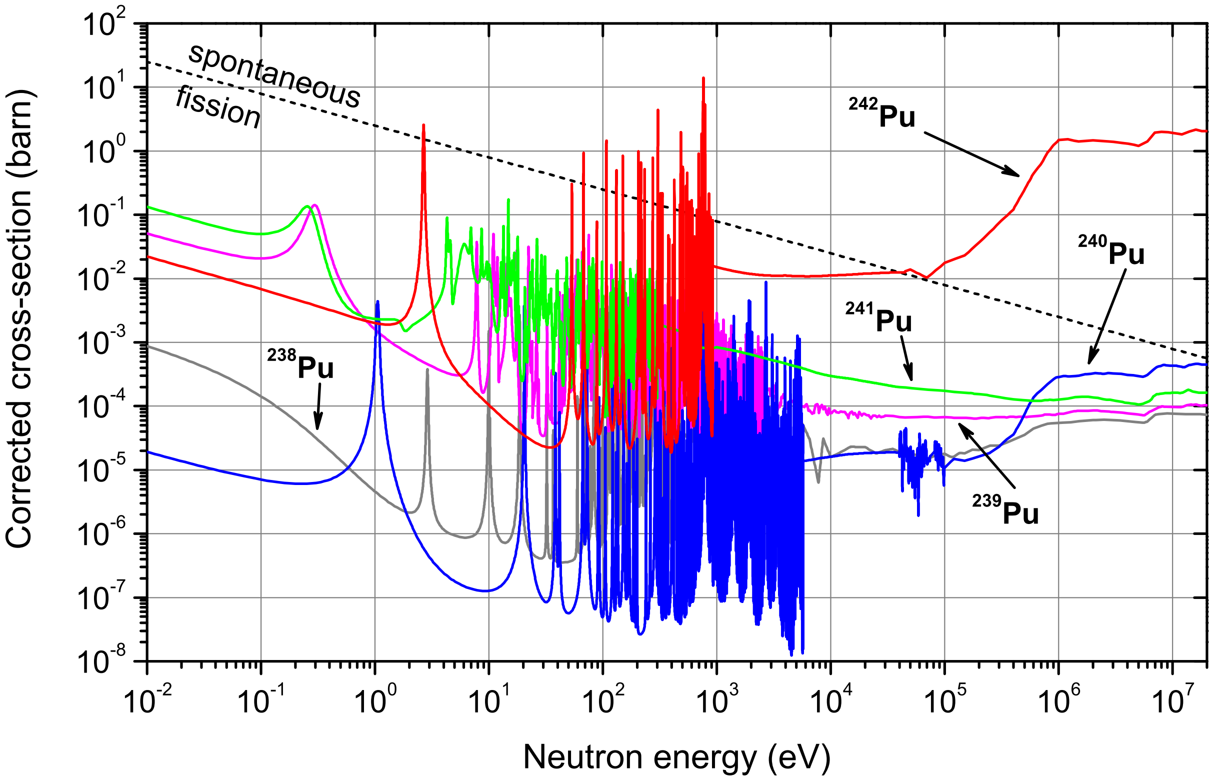

Figure 3.14: *The fission cross-section of ^{242}Pu, along with the fission cross-sections of the main contaminants present in the samples corrected for their abundances. The equivalent 'cross-section' of the spontaneous fission background is also shown and clearly dominates the low-energy region, except for certain ^{242}Pu resonances, and remains significant up to almost 100 keV.*

cross-section is shown along with relative contributions from the main sample contaminants and spontaneous fission. Spontaneous fission clearly dominates the low-energy region, with the exception of certain ^{242}Pu resonances, and remains significant up to almost 100 keV.

3.4.2 Detector efficiency and amplitude threshold correction

Each fission event leads to the production of two fission fragments emitted in practically opposite directions. Fission events are identified by the detection of the fragment that is emitted in the general direction of the detector gas volume. Before, however, the fragment can deposit energy in the gas, it needs to exit the sample deposit. While samples for fission cross-section measurements are generally made very thin for this precise reason, still, the fraction of fission fragments that lose all their energy inside the deposit is not negligible. The *detection efficiency* ε is defined as the fraction that does escape and deposits energy in the gas. In the simplest approach, this quantity is determined by calculating the energy loss of fission fragments inside the sample, for example using the a tool such as the SRIM code [73, 74]. For this analysis, the fraction of fission fragments that was stopped in the sample was estimated by means of Monte-Carlo simulations performed with FLUKA, as described in Section 2.3. Although the underlying physics is the same, a Monte-Carlo simulation better accounts for geometric effects, such as the different lengths travelled by the fission fragments inside the sample, and makes use of

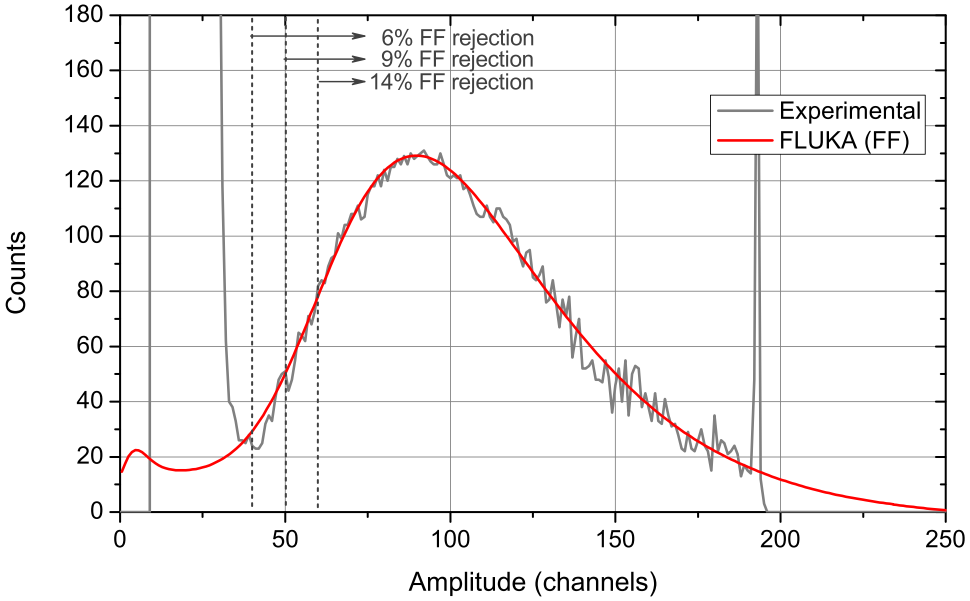

Figure 3.15: *A simulated fission fragment amplitude spectrum compared to an experimental spectrum obtained from a* ^{242}*Pu sample. Three different amplitude thresholds (at 40, 50 and 60 channels) are shown along with the corresponding fraction of rejected fission signals.*

realistic fission fragment distributions, which is impossible or, at least, highly impractical to achieve with a tool like SRIM. For the plutonium samples, approximately 99% of the fission fragments emitted in the direction of the gas volume were found to exit the sample and deposit energy in the gas ($\varepsilon = 0.99$), while for the thicker ^{235}U sample, approximately 5% of the fission fragments were stopped inside the deposit ($\varepsilon = 0.95$).

The fraction of fission events rejected by the amplitude threshold can be estimated in two ways. For ^{242}Pu, the known spontaneous fission rate can be used to determine this correction using data from the beam-off runs. Unfortunately, this method cannot be applied to ^{235}U. Furthermore, due the gain-drift previously described, the beam-off data obtained for ^{242}Pu are too sparse to obtain corrections valid for the entirety of the acquired data. To avoid this obstacle and to treat all samples in a consistent way, the simulated data were used. For each sample, a simulated amplitude spectrum was produced and subsequently smoothed to account for the detector and read-out resolution, attempting to match the experimental spectrum obtained from the same sample. An example is shown in figure 3.15, where the experimental amplitude spectrum obtained from a ^{242}Pu sample is compared with the simulated fission fragment spectrum. The integrals of the two distributions above 50 channels are within 0.1% of each other, which shows the very good reproduction of the experimental spectrum, at least above the centre of the 'valley' between α-particle and fission fragment signals. About 10% of fission signals are rejected ($f_c = 0.90$) with a typical choice of threshold a few channels above the centre of the 'valley', but the correction can vary between 85 and 95% ($f_c = 0.85 - 0.95$) depending on the detector and the choice of threshold.

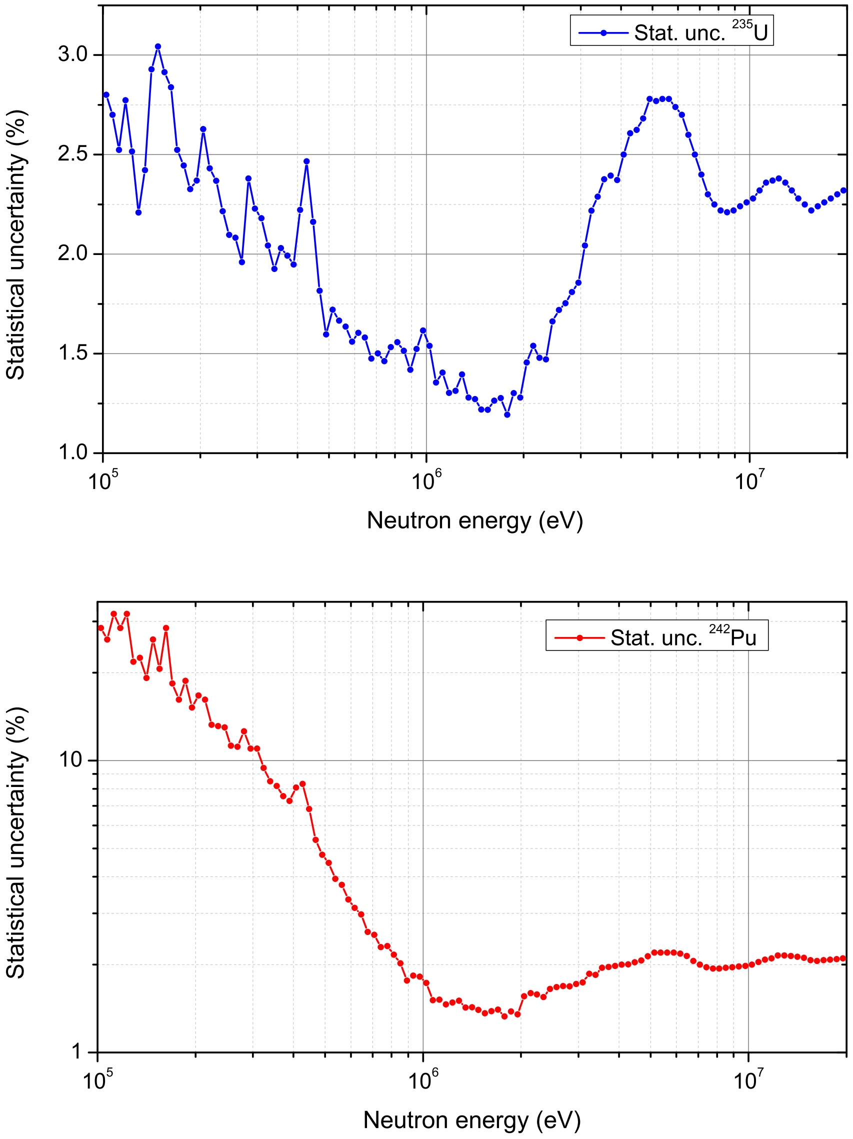

Figure 3.16: *Statistical uncertainties for* ^{235}*U and* ^{242}*Pu. The narrow structures are related to the absorption dips in the neutron flux.*

3.4.3 Uncertainties

The statistical uncertainty above 100 keV for ^{235}U and ^{242}Pu is shown in figure 3.16 for an energy binning of 50 bins per decade. The uncertainty varies between 1 and 3% for ^{235}U. In the case of ^{242}Pu, the statistical uncertainty is above 10% up to 300 keV and decreases rapidly, falling below 2% above 900 keV. It remains below 2% up to 4 MeV and below 3% up to 20 MeV. The statistical uncertainty at the resonances is around 1-2%, but higher between resonances due to the low cross-section.

Several factors contribute to the systematic uncertainties of the measurement and they are listed in Table 3.1.

In all cases, the stated uncertainty in the mass of the samples is less than 1%. In the case of the ^{235}U sample, however, the addition of a mask to reduce the active area of the sample to match the plutonium samples (see Section 1.2.2) causes a 3% uncertainty in the area. While this does not affect the areal density of the sample, which is the

Table 3.1: *Systematic uncertainties of the cross-section calculation.*

Contribution	Uncertainty
Sample mass	0.3% (^{235}U)$^{(a)}$ 0.9% (^{242}Pu)$^{(b)}$
Detector efficiency $^{(c)}$	2%
Amplitude threshold correction	2%
^{235}U(n,f) cross-section	< 1%
Neutron beam attenuation/divergence	*negligible*
Dead-time correction	*negligible*

$^{(a)}$ Uncertainty of the sample activity only. The total uncertainty on the mass (accounting for the deposit diameter, impurities etc.) is likely near 1%.

$^{(b)}$ Total uncertainty.

$^{(c)}$ Including uncertainty from fission fragment emission anisotropy.

quantity used in the calculations, it translates into a corresponding uncertainty in the overall normalisation.

Since the ^{235}U and ^{242}Pu samples are placed within a length of about 20 cm along the beam axis, the divergence of the neutron beam can be considered negligible. Furthermore, the attenuation of the neutron beam through the detectors (copper and kapton) and, more importantly, the sample backings (aluminium) are of the order of a few parts per thousand, with the exception of the strongest aluminium resonances at several tens of keV, which is an energy region outside this analysis due to extremely low statistics.

In all the analysis and the simulations described in Chapter 2, the emission of fission fragments was considered isotropic. In reality, the anisotropy of the fragment emission becomes significant above 1-2 MeV and then increases again above 6-7 MeV, when second-chance fission begins to occur [75–77]. Due to the increased linear momentum transfer, the angular distribution of the fragments becomes slightly biased towards forward angles. This could lead to an overall small increase in the detection efficiency of the fragments, since they traverse a smaller path inside the deposit. Nevertheless, this change is quite small (within 1%). Furthermore, due to the size and relative position of the samples and the detectors, the angular acceptance of the detector exceeds 80% in the worst case (i.e. the material further away from the sample centre).

No dead-time correction was considered for ^{242}Pu, due to the very low fission count-rate. Of course, α-pile-up occurs with a probability of a few percent (hence the obvious pile-up tail in figure 3.8 (left)), but this is partly taken care of by the raw data analysis routine (see Section 3.1.4) and, in any case, affects signals well below the amplitude threshold. Even in the case of ^{235}U, the relatively low mass of the sample meant that the fission pile-up probability was negligible even around 1 MeV, where the peak of the neutron rate occurs.

The ^{235}U(n,f) cross-section is considered known within 1%, especially above 150 keV, where it is among the neutron cross-section standards [78].

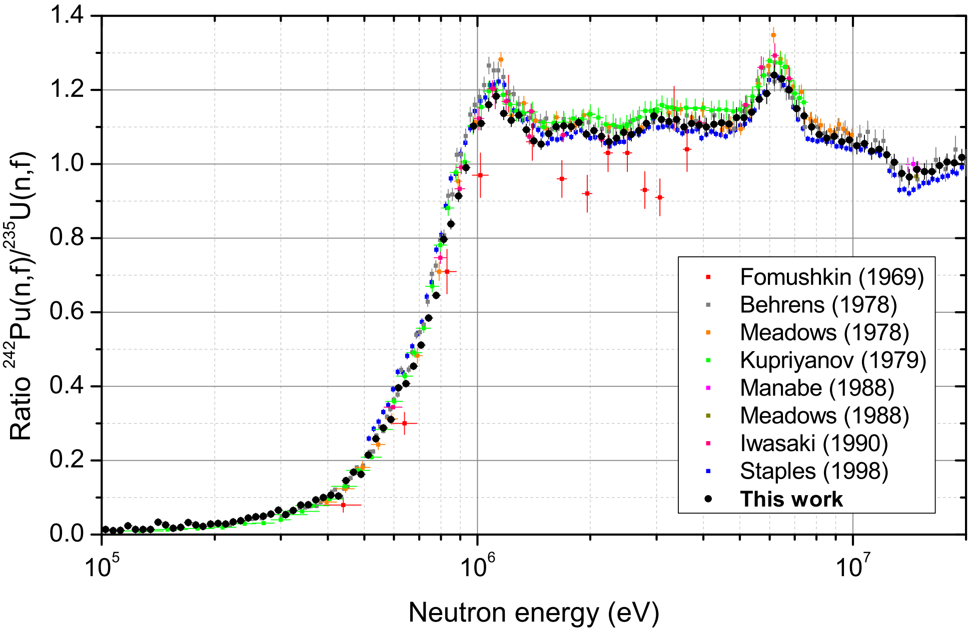

Figure 3.17: *The measured* ^{242}*Pu(n,f)/*^{235}*U(n,f) ratio compared to previous datasets retrieved from EXFOR. With one exception, all measurements are in agreement within approximately 15%.*

3.5 Results and discussion

3.5.1 The ^{242}Pu(n,f)/^{235}U(n,f) ratio

The ratio between the fission cross-sections of ^{242}Pu and ^{235}U is the critical experimental quantity for this measurement, since the final cross-section is calculated based on this result. Several datasets on the ^{242}Pu(n,f)/^{235}U(n,f) ratio are present in EXFOR [79–86]. With the exception of the data by Fomushkin et al. [79] that show large uncertainties and a somewhat anomalous behaviour of the ratio above 1 MeV compared to the other measurements, all the other datasets are in general agreement. There are only small discrepancies in the rise of the ratio up to 1 MeV, but the situation deteriorates above 1-2 MeV, with discrepancies near or above 10%. According to the corresponding EXFOR entry, the measurement by Fomushkin et al. was performed using a sample which included 6% of ^{239}Pu and also 17% of ^{240}Pu and 1% of ^{241}Pu, which could justify difficulties in isolating counts from ^{242}Pu, especially in the presence of fission events caused by low-energy parasitic neutrons in the fissile isotopes.

The results from the present measurement are plotted against the other datasets in figure 3.17. Above 1.5 MeV, the data follow the general trend of the results of Staples et al. [86], although they are for the most part systematically higher, while remaining below the Kupriyanov et al. data [82] and close to the Meadows et al. data [80]. The 'bump' just above 1 MeV seems to be slightly less pronounced in the present data. Below 1 MeV, the data are in overall agreement with previous measurements.

3.5.2 Results for ^{242}Pu(n,f)

Experimental results from several previous measurements of the ^{242}Pu(n,f) cross-section are present in EXFOR [79–96], although many cover a restricted energy range and/or consist of only a few points. The most comprehensive measurement to date was performed at the LANSCE (Los Alamos Neutron Science Center) facility of the Los Alamos National Laboratory (LANL) by Tovesson et al. [96].

The NEA request for the ^{242}Pu(n,f) cross-section concerns the 0.2-20 MeV range [11]. Nevertheless, and despite the high spontaneous fission background, several resonances were detected. Unfortunately, results below 2 keV from Tovesson et al. have not yet been included in EXFOR, so a comparison with that measurement is presently not possible in that range. On the contrary, data from the measurements by Auchampaugh et al. [89] and Bergen et al. [90] extend over the resolved resonance region. Results are shown in figure 3.18, along with the other experimental data and the evaluated cross-section from major libraries (ENDF/B-VII.1, JEFF 3.2, JENDL 4.0 and BROND 2.2).

The resonance at 2.67 eV (figure 3.18a) is the first to appear in the ^{242}Pu(n,f) cross-section and is very prominent, even above the spontaneous fission background. At around 482 eV, another resonance was detected which is also present in the data by Bergen and Auchampaugh (figure 3.18b). Several resonances between 700 and 800 eV have been detected, including one not present in evaluations or in any of the other datasets at 778 eV (figure 3.18c). A systematic offset in the resonance energies with respect to the data by Bergen and Auchampaugh is clearly observed, although the present data seem to better match the position of the resonances in the evaluated cross-sections. Among the libraries plotted with the data, resonances are included up to 1150 eV (in (JEFF 3.2), although several have also been detected above this energy. At 1835 eV, the present data confirm the observed resonance by Bergen and Auchampaugh (figure 3.18d), as is the case at 4.9 keV and 28.2 keV (figures 3.18e and 3.18f). None of these last three resonances are included in any of the evaluated libraries.

Results for the cross-section above 100 keV and up to 20 MeV are shown in figure 3.19. The two datasets by Auchampaugh are highly discrepant above 1 MeV and show a very different trend of the cross-section above the second-chance fission threshold compared to all other measurements. The data by Fomushkin are also in clear disagreement, even in the range of the rise of the cross-section. Excluding these datasets, the remaining data follow the same overall trend, with the most extended measurements being those by Bergen, Weigmann [94] and Tovesson. Discrepancies up to a few MeV are within 10% and slightly lower at higher energies, in part due to the fact that the number of datasets is also lower. An exception is in the range of 7.5-9.0 MeV where larger discrepancies are due mainly to the Weigmann data showing a completely different trend than the other datasets at the top of the second-chance fission 'step'. Around the fission threshold and up to about 1 MeV, the present data follow the well-defined trend of the other measurements. Above that energy, the data are generally 2-3% higher than the Tovesson data, without for the most part exceeding the data by Weigmann. The 'bump' at around 1 MeV seems slightly less pronounced compared to other measurements.

Considerable discrepancies are found between evaluations. In figure 3.20, the evaluated cross-sections are plotted against the most extended datasets. The BROND evaluation is at the low end of experimental uncertainties up to almost 2 MeV and considerably higher than available data above 7 MeV. The JENDL evaluation seems to exactly

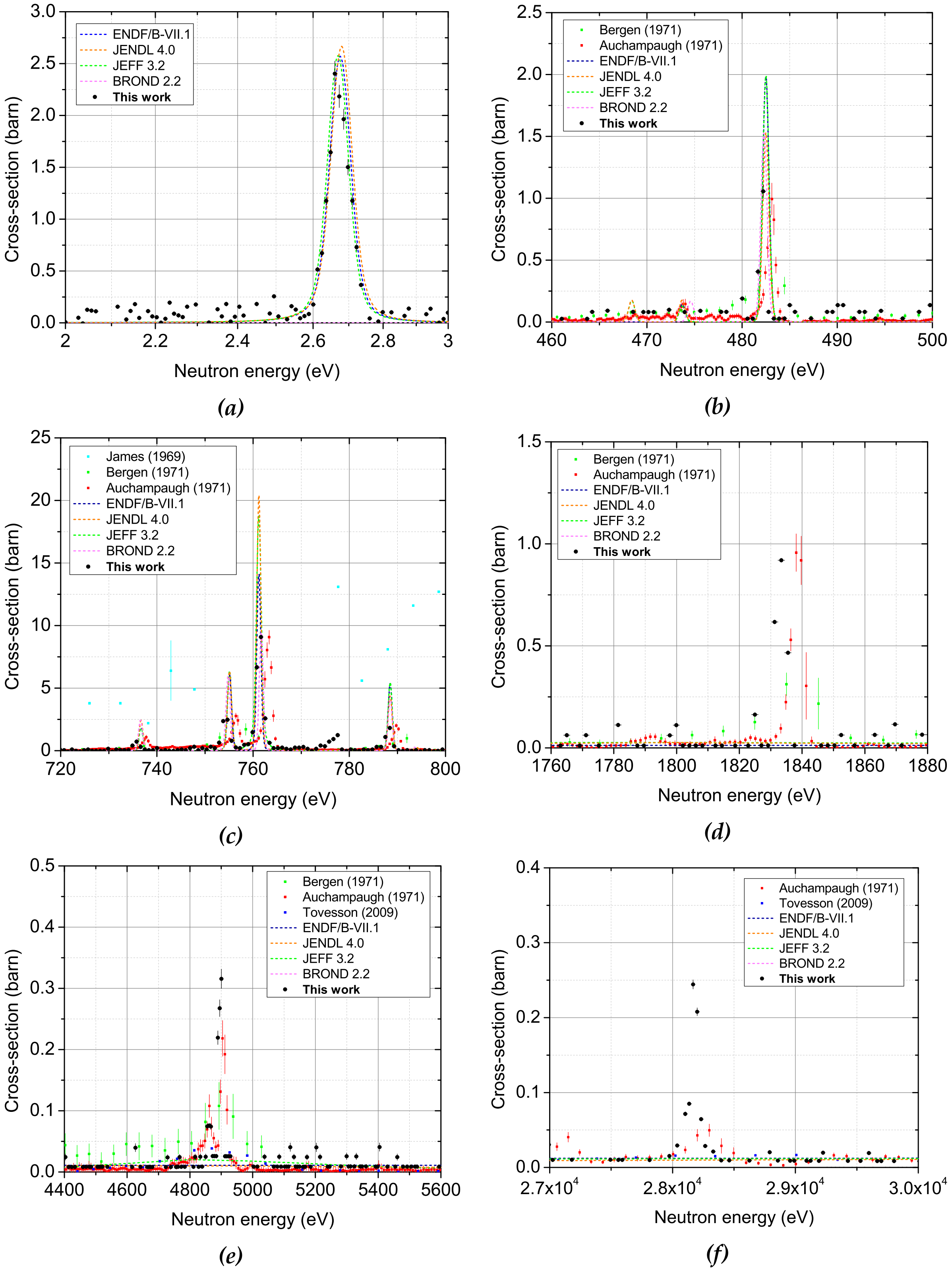

(a) *(b)* *(c)* *(d)* *(e)* *(f)*

Figure 3.18: *Several resonances detected in the ^{242}Pu(n,f) data, along with evaluated cross-sections from the ENDF/B-VII.1, JEFF 3.2, JENDL 4.0 and BROND 2.2 libraries: (a) The first resonance at about 2.7 eV, (b) the resonance at 482 eV, (c) several resonances between 730 and 790 eV, including one not previously detected at about 778 eV, (d) a resonance at around 1835 eV, (e) the resonance at 4.9 keV, (f) the resonance at 28.2 keV.*

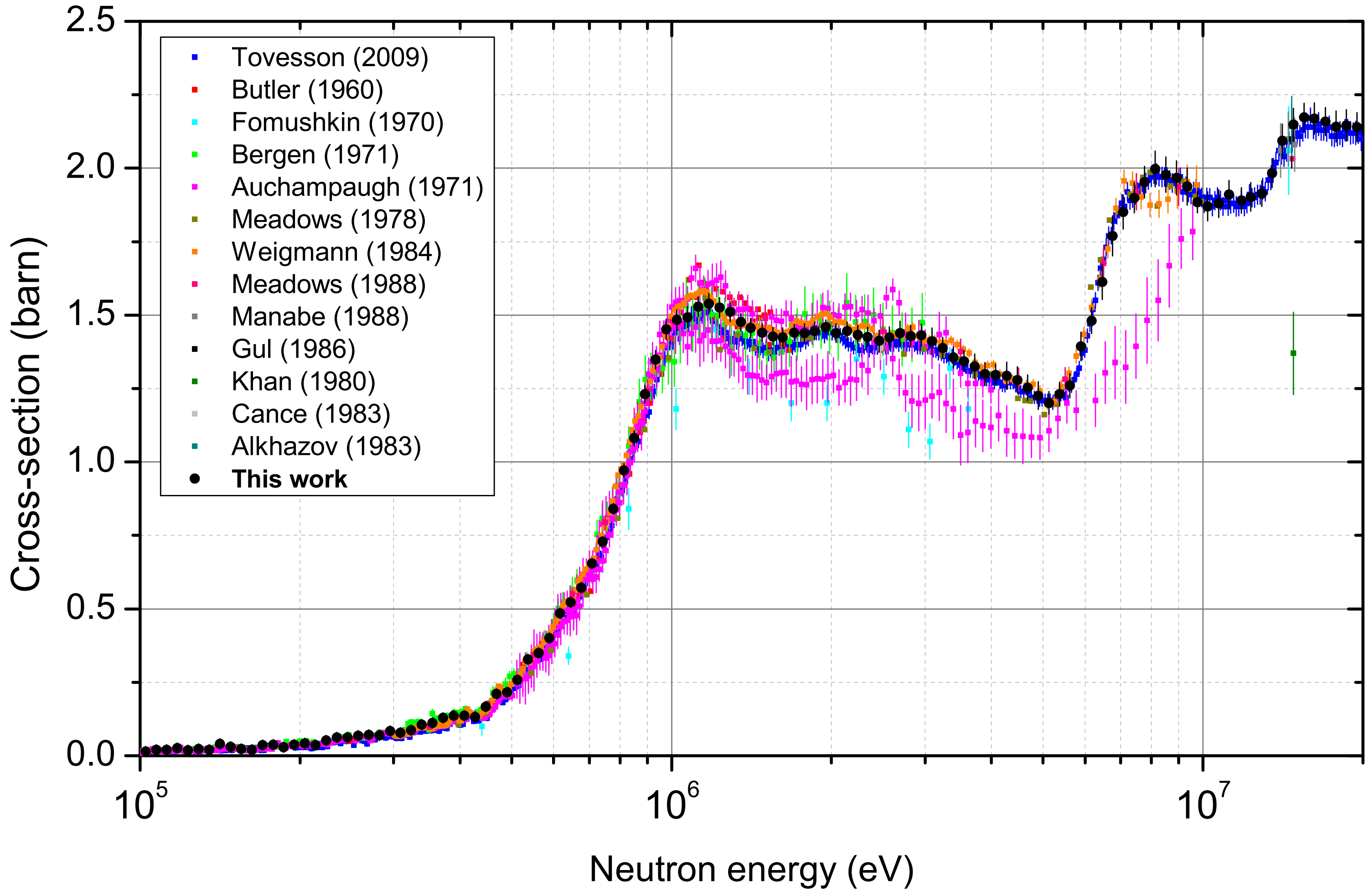

Figure 3.19: *Results on the* ^{242}*Pu(n,f) cross-section between 100 keV and 20 MeV compared with results from previous measurements retrieved from EXFOR.*

follow the data by Weigmann, ignoring other results. In both cases, a re-evaluation based on more recent measurements is likely required. The ENDF and JEFF evaluations are almost identical and seem to better follow the experimental data, with the exception of the data above 16 MeV, where they significantly underestimate the measured cross-section.

In conclusion, the present measurement of the ^{242}Pu(n,f) cross-section, the latest in a series of fission cross-section measurements performed at n_TOF, has been completed successfully, despite the experimental difficulties that were encountered. The most significant contribution to the uncertainty lies in the overall normalisation of the results, which is a recurring theme in such experiments and which emphasises the need for repeated measurements of these cross-sections with different experimental setups in order to isolate systematic uncertainties and obtain accurate estimates of fission cross-sections of actinides. The present data represent a significant contribution in this direction.

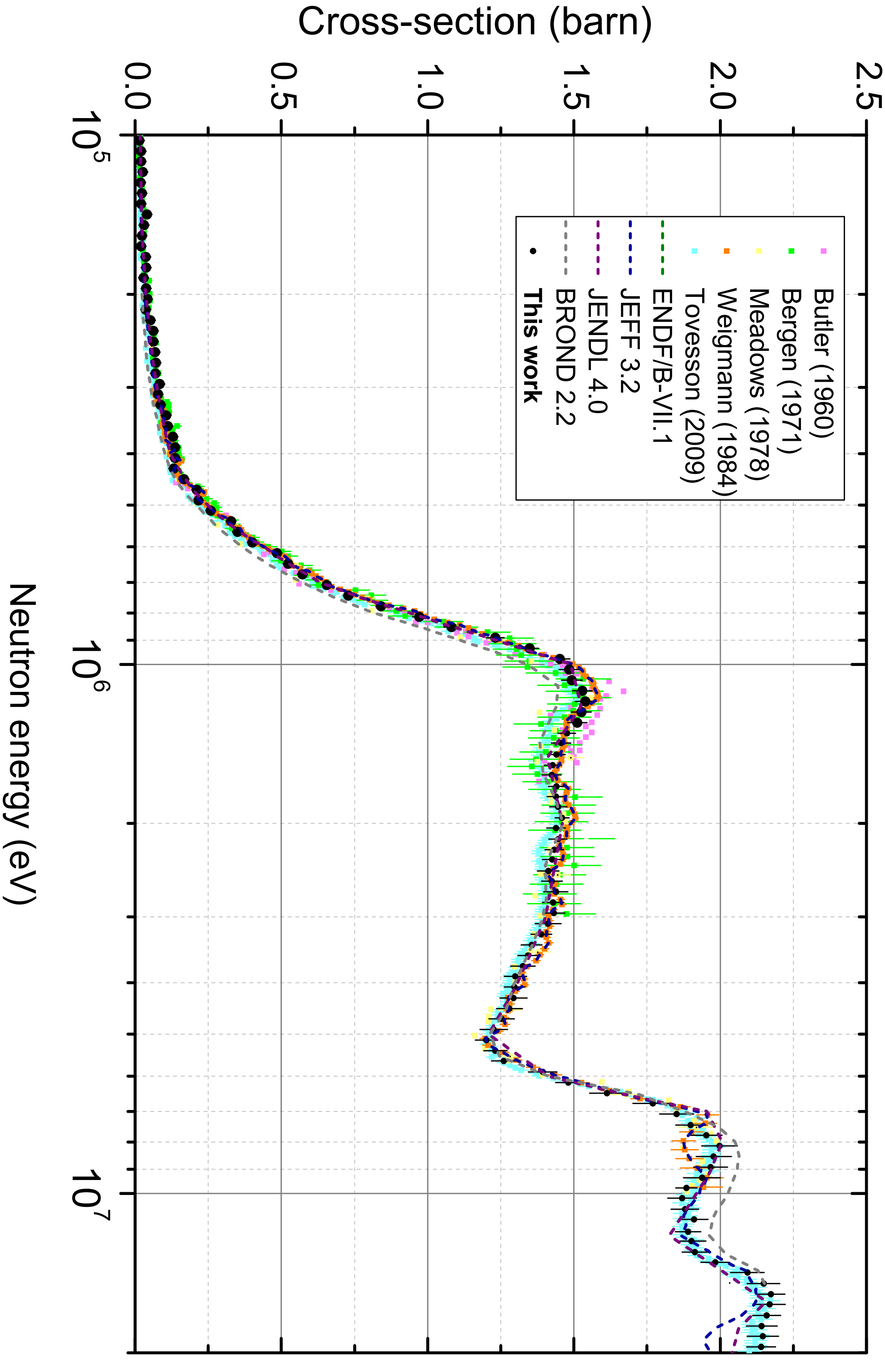

Figure 3.20: *Results on the ^{242}Pu(n,f) cross-section between 100 keV and 20 MeV along with some of the most representative precious measurements compared to evaluated libraries (ENDF/B-VII.1, JEFF 3.2, JENDL 4.0 and BROND 2.2).*

Chapter 4

Theoretical fission cross-section calculations

A theoretical calculation of the ^{242}Pu(n,f) cross section has been performed with the EMPIRE nuclear reaction model code. Before the presentation of the EMPIRE code, the parameters used and the results of the calculations, this chapter begins with an overview of the theory of nuclear fission in order to provide the theoretical framework and the physical meaning of the parameters used in the calculations. Discussions of different aspects of nuclear fission can be found in Wagemans [97] and Vandenbosch and Huizenga [98], while fission in the context of statistical models is discussed by Cole [99] and Krappe and Pomorski [100].

4.1 Nuclear fission

4.1.1 Discovery of fission

With the discovery of the neutron by Chadwick [101, 102] in 1932, an entirely new set of nuclear interactions could be studied. Up to that time, activation of nuclei with charged particles, such as protons, deuteron nuclei and α-particles had been limited to light elements. Lacking electrical charge, neutrons would naturally be expected to interact much more easily, even with heavy nuclei, despite the fact that available neutron sources were much less intense than charged particle sources. In 1934, Fermi and co-workers [103, 104] undertook a series of experiments in which they exposed a large number of elements to neutrons produced with a beryllium-radon source. They observed that, following the capture of a neutron, many nuclei – indeed, more than 40 of about 60 investigated – become radioactive and decay by emitting an electron (β^--decay). This results in a residual nucleus that has an atomic number one unit higher than the target nucleus, according to: $n + {}^{A}_{Z}X \rightarrow {}^{A}_{Z+1}Y + \beta^- + \overline{\nu_e}$. Following this logic, it seemed that the goal of producing transuranic elements could be accomplished by bombarding heavy nuclei with neutrons and causing similar reactions. Experiments using natural uranium yielded different activities, which were initially interpreted as coming from transuranic elements, despite the fact that the considerable number of the observed activities raised doubts on this interpretation.

In 1938, Hahn and Strassmann [105] determined the presence of substances with chemical behaviour similar to barium and lanthanum in the products of these experiments and attributed the activities to isomeric states of radium and actinium, which are directly below barium and lanthanum in the periodic table and are thus expected to have similar chemical behaviour. This interpretation, however, implies that (n,2α) reactions are occurring in uranium, after bombardment with both thermal and fast neutrons, raising further doubts about the correct interpretation of the experiments. Attempting to resolve this situation, in 1939, Hahn and Strassmann [106] isolated the products of these reactions using sensitive radiochemical techniques that allowed them to distinguish between barium and radium (and lanthanum and actinium) and determined that barium was present, along with isotopes of lanthanum, and not the heavier radium and actinium.

Meitner and Frisch [107, 108] concluded that bombarding heavy nuclei with neutrons causes them to become so unstable that they split into two nuclei of intermediate weight and roughly equal mass. This would be accompanied by the release of approximately 200 MeV as kinetic energy of the fission products, corresponding to the mass difference between the original nucleus and the fragments. This was soon confirmed independently by Frisch [109], who performed experiments in an ionisation chamber, and Joliot [110]. Meitner and Frisch named this new phenomenon *fission*, borrowing the term that describes cellular division in biology. They were also the first to propose a theoretical interpretation of fission based on an analogy of the nucleus with a drop of liquid that splits into two smaller drops when it is excited into vibration. In this analogy, the occurrence of fission of a particular nucleus would hinge on the balance between the nuclear forces, acting as surface tension, and the electrostatic repulsion between protons. Given the difference in range between nuclear and electromagnetic interactions, fission is expected to be more likely in heavier nuclei, where the protons are already distributed in a larger volume. Based on such considerations, they estimated that nuclei with atomic numbers near 100 would instantly break apart.

A very interesting review of the rapid developments in nuclear physics that occurred during the 1930s following the discovery of the neutron and led to the discovery of fission is given by Amaldi [111], one of Fermi's collaborators in the original work and a review article by Turner [112], who, in 1940, quite impressively notes that:

> *'Although less than a year has passed since the discovery by Hahn and Strassmann that the capture of neutrons by uranium nuclei may lead to their disruption to form lighter nuclei, nearly one hundred papers on this subject have already appeared. This number does not include the many older papers written before the true nature of the process was understood.'*

4.1.2 The liquid-drop model

Very soon after fission was identified, Bohr and Wheeler [113] formulated a theoretical framework for the newly-discovered phenomenon based on the liquid-drop model previously developed by Gamow [114, 115] and qualitatively applied to fission by Meitner and Frisch.

The semi-empirical mass formula, in its simplest form (without any pairing effects, discussed later) can be written as:

$$\begin{aligned} E &= E_v + E_s + E_c + E_a \\ &= a_v A - a_s A^{2/3} - a_c \frac{Z(Z-1)}{A^{1/3}} - a_a \frac{(N-Z)^2}{A} \end{aligned} \tag{4.1}$$

Considering that the radius of the nucleus has empirically been found to be proportional to $A^{1/3}$ as $r = r_0 A^{1/3}$, with $r_0 \approx 1.25 \times 10^{-15}$ m, the first and dominant term, which is proportional to A, is called the *volume* term and expresses the fact that the binding energy of the nucleus generally increases with increasing number of nucleons. The second term is proportional to $A^{2/3}$ and is therefore called the *surface* term. This term accounts for the fact that nucleons near the nuclear surface interact with fewer other nucleons on average and are therefore less bound, hence the negative sign of this term. The third term is the *Coulomb* term and describes the repulsive electrostatic force between the protons – again, a negative contribution. The fourth term, known as the *asymmetry* or *symmetry energy* term is related to the specific composition of the nucleus and arises as a direct consequence of the Pauli exclusion principle. Since protons and neutrons in the nucleus occupy two distinct sets of states that are populated according to the exclusion principle (see Section 4.1.3), an excess of neutrons, for example, will lead to higher energy neutron states being populated, despite the fact that lower energy proton states are available, thus increasing the energy of the whole nucleus.

Since the density of nuclear matter is known to be constant, the volume of a nucleus can also be considered to remain constant, even when the nucleus is deformed. Of the four terms in equation 4.1, the volume and asymmetry terms are proportional to A (the volume) and are therefore independent of the deformation. The discussion of the changes in energy of the nucleus for different deformations can therefore be limited to the surface and Coulomb terms.

Assuming a spherical shape as the most stable configuration of the nucleus, in an obvious analogy to a liquid drop, then the deformed nucleus can be described as an ellipsoid by revolution, whose semi-major and semi-minor axes can generally be written respectively as:

$$\begin{aligned} a &= R(1 + \varepsilon_1) \\ b &= R(1 - \varepsilon_2) \end{aligned} \tag{4.2}$$

The volume of the nucleus must remain constant, therefore, using eq. 4.2:

$$\begin{aligned} V(\varepsilon) &= V(\varepsilon = 0) \Leftrightarrow \\ \frac{4}{3}\pi a b^2 &= \frac{4}{3}\pi R^3 \Leftrightarrow \\ (1+\varepsilon_1)(1-\varepsilon_2)^2 &= 1 \Leftrightarrow \\ 1 - \varepsilon_2 &= (1+\varepsilon_1)^{-1/2} \approx 1 - \frac{\varepsilon_1}{2} \Leftrightarrow \\ \varepsilon_2 &= \frac{\varepsilon_1}{2} \end{aligned} \tag{4.3}$$

so that the axes of the ellipsoid can be rewritten as functions of a single eccentricity parameter ε as:

$$\begin{aligned} a &= R(1+\varepsilon) \\ b &= R\left(1-\frac{\varepsilon}{2}\right) \end{aligned} \tag{4.4}$$

With the axes so defined, the surface of the ellipsoid can be written as:

$$S(\varepsilon) = 4\pi R^2\left(1+\frac{2}{5}\varepsilon^2+...\right) = S(\varepsilon=0)\left(1+\frac{2}{5}\varepsilon^2+...\right) \tag{4.5}$$

so that the surface energy term of the deformed nucleus will be also related to the surface energy of the spherical configuration as:

$$E_s(\varepsilon) = E_s(\varepsilon=0)\left(1+\frac{2}{5}\varepsilon^2+...\right) \tag{4.6}$$

Similarly, for the Coulomb energy we finally obtain:

$$E_c(\varepsilon) = E_c(\varepsilon=0)\left(1-\frac{1}{5}\varepsilon^2+...\right) \tag{4.7}$$

where

$$E_c(\varepsilon=0) = \frac{1}{4\pi\varepsilon_0}\frac{3}{5}\frac{(Ze)^2}{R} \tag{4.8}$$

Combining equations 4.6 and 4.7, the total deformation energy (i.e. the energy change relative to the initial spherical configuration) is:

$$\begin{aligned} E(\varepsilon) &= E_s(\varepsilon)+E_c(\varepsilon) \\ &= E_s(\varepsilon=0)\left(1+\frac{2}{5}\varepsilon^2+...\right)+E_c(\varepsilon=0)\left(1-\frac{1}{5}\varepsilon^2+...\right) \\ &= [E_s(\varepsilon=0)+E_c(\varepsilon=0)]+E_s(\varepsilon=0)\frac{2}{5}\varepsilon^2-E_c(\varepsilon=0)\frac{1}{5}\varepsilon^2+... \\ &\approx E(\varepsilon=0)+\frac{2}{5}\varepsilon^2 E_s(\varepsilon=0)\left[1-\frac{E_c(\varepsilon=0)}{2E_s(\varepsilon=0)}\right] \end{aligned} \tag{4.9}$$

We can then define the *fissility parameter* x to be:

$$x = \frac{E_c(\varepsilon=0)}{2E_s(\varepsilon=0)} \tag{4.10}$$

When $x > 1$, then $E(\varepsilon) < E(\varepsilon = 0)$ and fission proceeds freely. If, on the other hand, $x < 1$, then $E(\varepsilon) > E(\varepsilon = 0)$; in this case, the deformation energy will generally increase with increasing values of the deformation parameter ε, until higher order terms in the above expansions become significant, leading to a decrease. This competition between the surface and Coulomb terms leads to the creation of a (single-humped) potential barrier. Since a local minimum in the deformation potential appears for zero deformation, the liquid-drop model predicts a spherical shape for nuclei in their ground state, which, as will be discussed later, is not generally true.

Substituting from eq. 4.1, we obtain:

$$x = \frac{a_c \frac{Z^2}{A^{1/3}}}{2a_s A^{2/3}} = \frac{a_c}{2a_s}\frac{Z^2}{A} \tag{4.11}$$

Values for the coefficients in the simplified semi-empirical mass formula (eq. 4.1) can be obtained by fitting experimental nuclear mass values. Using these values we finally obtain[1]:

$$x \approx \frac{1}{51}\frac{Z^2}{A} \tag{4.12}$$

The limit, therefore, for the existence of a potential barrier to inhibit spontaneous fission is:

$$x > 1 \Leftrightarrow \frac{Z^2}{A} > 51 \tag{4.13}$$

which means that nuclei with values of Z larger than about 125 will be unstable against fission and would spontaneously split immediately after their creation. The value of Z^2/A for ^{242}Pu, for comparison, is 36.5, with $x = 0.73$.

What has been described so far in this section is an entirely macroscopic treatment of the fission process. An important weakness of this approach is that the height of the fission barrier, which is of the order of a few MeV, is the result of a partial cancellation of two terms (the surface and Coulomb energies), each of the order of hundreds of MeV. Second order effects of much lower magnitude, such as those related to the nuclear shell structure, can therefore still become very important in determining the characteristics of the fission barrier. This coupling between collective variables that describe the fissioning nucleus macroscopically and single-particle effects is one of the major difficulties in constructing a complete theory of fission that will accurately predict all of its observed characteristics.

4.1.3 The double-humped fission barrier

An obvious shortcoming of the liquid drop model is that it ignores effects caused by the shell structure of the nucleus. It further implies a strong dependence of the fission barrier on Z^2/A, which contradicts experimental observations, as does the assumption of a spherical shape for the ground states.

---

[1] Different sets of values can be found depending on the analysis performed. Nevertheless, the factor of 51 in eq. 4.12 does not vary significantly and the exact value does not influence the essence of the discussion or the conclusions drawn.

In the single-particle approach, each nucleon is treated as being in a potential well that corresponds to its interaction with all the other nucleons. The nucleus is seen as a 'Fermi ball' of protons and neutrons and its energy states are calculated accordingly by summing the energy of the states occupied by individual nucleons. Protons and neutrons are considered to occupy two independent sets of states in this potential. Shell structure can be combined with the liquid-drop model with the 'macroscopic-microscopic' (or 'shell correction') approach put forward by Strutinsky [116], leading to significant effects on the fission barrier.

The mass formula (eq. 4.1) can be expanded to include additional terms that correspond to the *pairing energy* and the *shell correction*:

$$\begin{aligned} E &= E_v + E_s + E_c + E_a + \delta(A, Z) + \delta U \\ &= E_{LDM} + \delta(A, Z) + \delta U \end{aligned} \tag{4.14}$$

The pairing term is again related to the Pauli exclusion principle and the specific composition of the nucleus and it expresses the fact that the energy of the nucleus will be lower when there is an equal number of protons (neutrons) with spin up and spin down. Obviously this is achieved for even numbers of protons (neutrons). The pairing energy is given by:

$$\delta(A, Z) = \begin{cases} -\delta_0 & Z, N \text{ even} \\ 0 & A \text{ odd} \\ +\delta_0 & Z, N \text{ odd} \end{cases} \tag{4.15}$$

where:

$$\delta_0 = \frac{a_p}{A^{1/2}} \tag{4.16}$$

The shell correction term δU introduced by Strutinsky is calculated as the difference $\delta U = U - \tilde{U}$ between the total energy U of the nucleus calculated with a realistic single-particle model that includes non-uniform single-particle state densities and level degeneracies, and the energy $\tilde{U}$ calculated for a uniform distribution obtained by averaging the nucleon level density over a sufficiently wide energy range so as to smooth-out any shell effects, while following the overall density of single-particle states. The advantage of this approach is that whatever systematic errors are introduced by the calculation of the total energy of the nucleus as a sum of single-particle state energies are expected to cancel each other out, leaving only effects attributable to the actual shell structure of the nucleus for a given deformation.

The value of the shell correction was found to be strongly dependent on the single-particle level density near the Fermi energy of the nucleus. The changes in the shell model level density at the Fermi energy, therefore, cause oscillations in the shell correction with increasing deformation. The pairing correction, on the other hand, has an opposite behaviour to the shell correction, but a lower magnitude, thus reducing the amplitude of the oscillation without changing its overall behaviour.

The superposition of the shell correction and the pairing term on the liquid-drop estimate of the nuclear energy as a function of deformation results in a double-humped

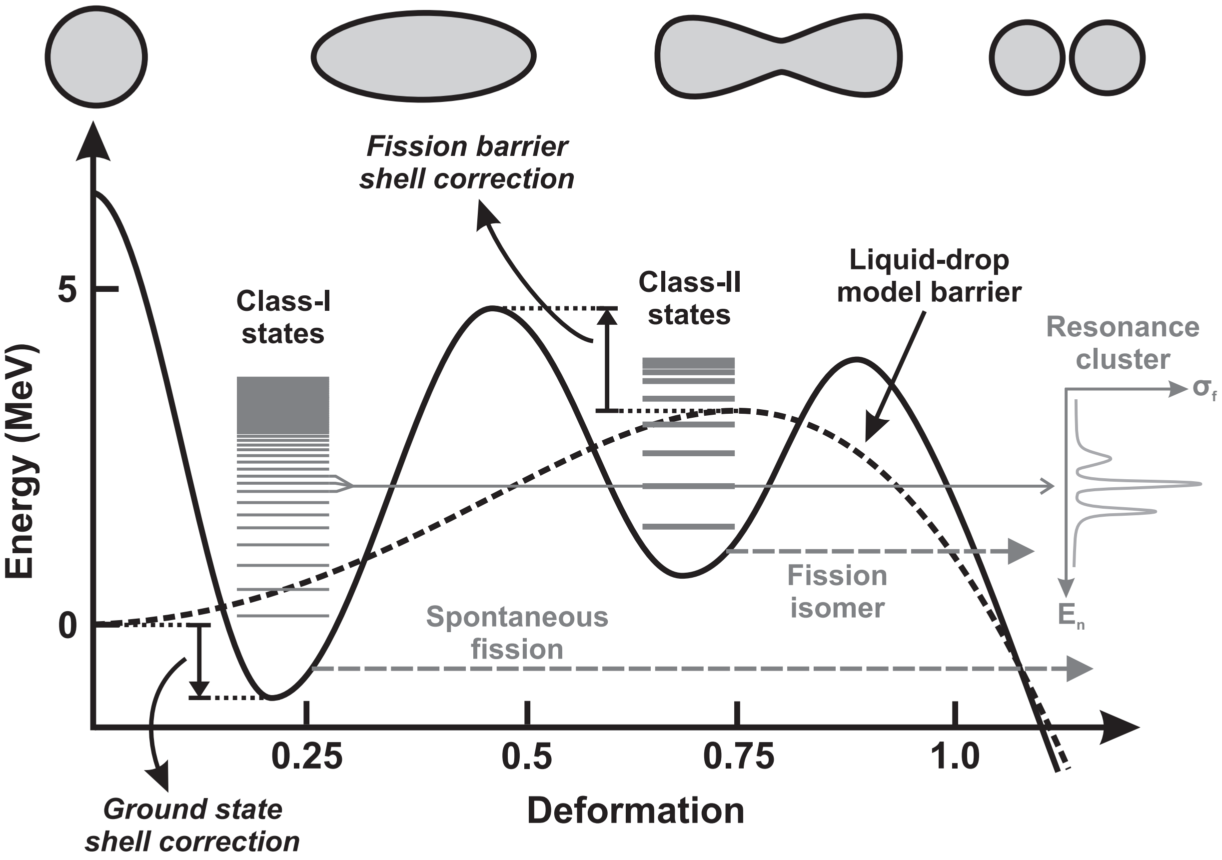

Figure 4.1: *A schematic illustration of a double-humped fission barrier, with a corresponding liquid-drop model barrier. Class-I and Class-II states are found in the first and second potential wells respectively, and their coupling leads to the modulation of low energy neutron fission resonances. The zero energy value corresponds to the energy of the undeformed nucleus in the liquid-drop treatment. Axis values are indicative.*

fission barrier, since the second large local minimum of the shell correction corresponds roughly to the liquid-drop model saddle point. Additionally, the first large minimum of the shell correction creates a local minimum in the deformation energy for non-zero deformation. This implies a non-spherical equilibrium shape for the ground state of the nucleus, as determined experimentally but contrary to the liquid-drop model assumptions where the spherical shape is considered as the most stable. These calculations were also able to more adequately reproduce the observed fission barrier heights. Figure 4.1 shows a double-humped fission barrier, along with the corresponding liquid-drop model barrier. States in the first well are called 'Class-I' states and are dense and narrow, while the 'Class-II' states in the second well are wider and more sparsely spaced.

The double-humped fission barrier was an essential breakthrough in the understanding of the fission mechanism and a very detailed and formal description is given by Bjørnholm and Lynn [117]. This result offered a theoretical explanation of two experimentally observed features of fission that could not be interpreted within the liquid-drop model. The first was the existence of *fission* (or *shape*) *isomers*. Fission isomers are states that undergo fission, but with a relatively very long half-life, instead of proceeding via γ-deexcitation in much faster times. These could now be understood as states in the second potential well. The second effect was the 'modulation' of low energy fission

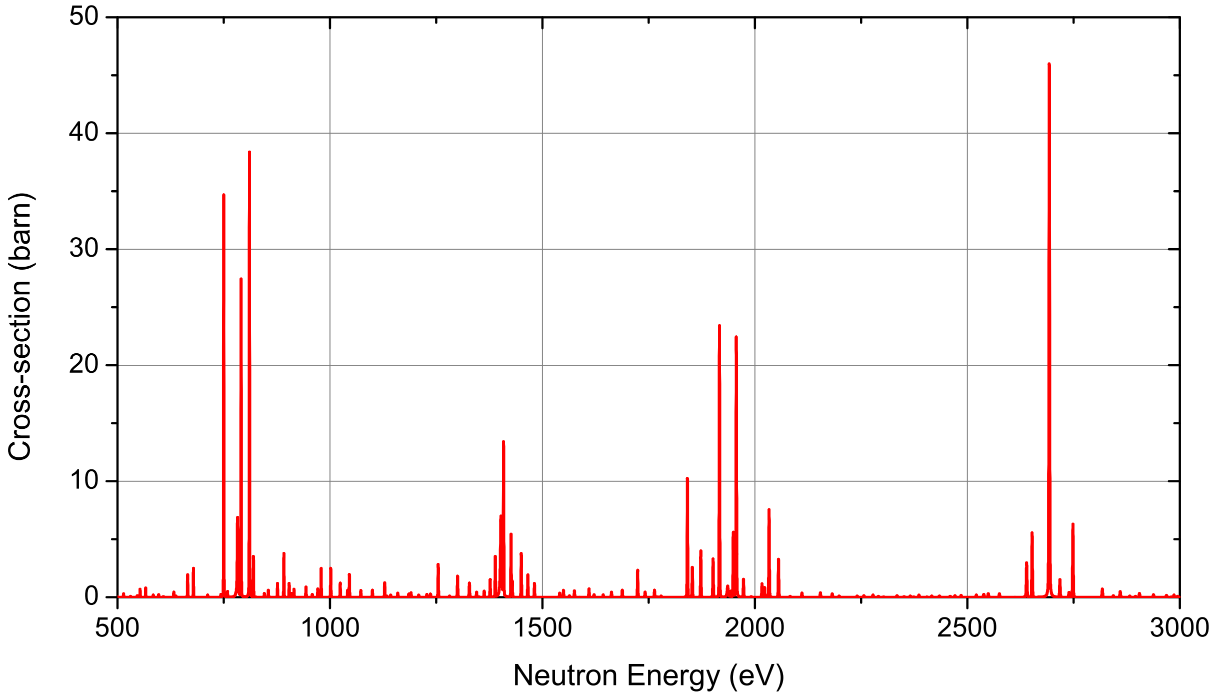

Figure 4.2: *Clusters of resonances in the fission cross-section of* ^{240}*Pu, attributable to coupling of Class-I and Class-II states. The spacing between clusters corresponds to the spacing of Class-II states, while the spacings within each cluster correspond to the spacing of Class-I states.*

resonances, or, in other words, the tendency of these resonances to be found in clusters, such as those shown in figure 4.2. Each cluster corresponds to a Class-II state, which has a higher fission width, since it only needs to penetrate a much thinner barrier, while the internal structure is due to the narrower and denser Class-I states. Whenever the nucleus is excited to a Class-I state that is well-matched in energy and spin-parity with a Class-II state, then the fission probability is higher and a resonance is observed in the measured fission cross-section. The spacing between clusters corresponds to the spacing of Class-II states, while the spacings within each cluster are characteristic of Class-I states.

More recently, these concepts have been expanded with the assumption that the nucleus does not encounter a single barrier, but rather a system of barriers within a multi-dimensional potential surface and has, therefore, different paths (or *modes*) available to fission. This new concept of *multi-modal fission* has been advanced by Möller [118, 119] and there is some experimental evidence to support this approach. Furthermore, along similar lines concerning alternative paths to fission, and attempting to model the pre-scission shape, when the two nascent fission fragments are still connected by a long 'neck', the *multimodal random neck-rupture model* (MM-RNRM) [120, 121] predicts different fission modes, such as the 'Superlong' (SL) mode, leading to a symmetric fission fragment mass distribution and the 'Standard I' (ST-1) and 'Standard II' (ST-2) modes that account for shell effects in the fragment mass distribution and are responsible for the fine structure in the asymmetric mass peaks.

Finally, certain experimental observations, most notably the narrow resonance-like structures at the fision threshold of ^{230,232}Th – known as the 'thorium anomaly' –, have been interpreted [122] assuming a triple-humped fission barrier, in which the second hump of the conventional double-humped barrier is split into two barriers by a shallow well or at least displays a 'hump' along the slope after its peak. The theoretical possibility of the existence of multiple-humped fission barriers – and triple-humped barriers in particular – is already discussed by Bjornholm and Lynn [117] in the context of Strutinsky's theory, but the question has not yet been conclusively settled.

4.1.4 Neutron-induced fission cross-sections

Based on the theoretical discussion of the fission process, the main features of fission cross-sections can be explained. At low incident neutron energies (thermal and up to about 1 eV), the reaction probability is proportional to the time the neutron spends inside the nucleus, therefore inversely proportional to the neutron velocity. This is commonly called the '$1/v$ law', which is a common feature of low-energy neutron absorption reaction cross-sections. Using eq. 1.1, it can be expressed as:

$$\sigma \propto \frac{1}{v} \propto \frac{1}{\sqrt{E}} \tag{4.17}$$

When the neutron binding energy is higher than the *activation energy* (the difference between the peak of the fission barrier and the ground state), such as in ^{235}U and ^{239}Pu, then the absorption of even a 'zero-energy' neutron leads to a compound nucleus that is unstable against fission and the fission cross-section is very high, even for very low incident neutron energies. When that is not the case, as for ^{238}U and ^{237}Np, additional energy must be provided to the compound nucleus in order to overcome the barrier. This explains the differences of several orders of magnitude in the low-energy fission cross-sections shown in Figure 4.3.

The different behaviour observed in these isotopes can be largely attributed to the pairing energy described in the previous section. The activation energy of isotopes of U, Np, Pu is in most cases around 6.5 MeV. The excitation energy of a nucleus after neutron capture, however, is increased or lowered by an amount $\delta(A, Z)$ depending on its nucleon configuration. For odd-N nuclei, such as ^{235}U and ^{239}Pu, neutron capture leads to an even-N nucleus whose ground state is lowered by $\delta \approx 0.78$ MeV, thus resulting in an excitation energy of the compound nucleus increased by the same amount. On the other hand, even-N nuclei, such as ^{238}U and ^{237}Np, either have a ground state lowered or a ground state of the compound nucleus increased by the same amount, leading in both cases to lower excitation energies of the compound nucleus and inhibiting fission for low incident neutron energies.

Following the smooth '$1/v$' behaviour (or even superimposed on it), resonances begin to appear in the fission cross-section, corresponding to excited states of the compound nucleus with particularly high fission widths. These resonances are relatively narrow and can be resolved experimentally. This *resolved resonance region* extends up to about 10 keV for heavy nuclei. At higher energies, above 50-100 keV, depending on the nucleus, the compound system is excited into its continuum and individual states cannot be resolved (hence the name *unresolved resonance region*), leading to a smooth behaviour of the cross-section in this region.

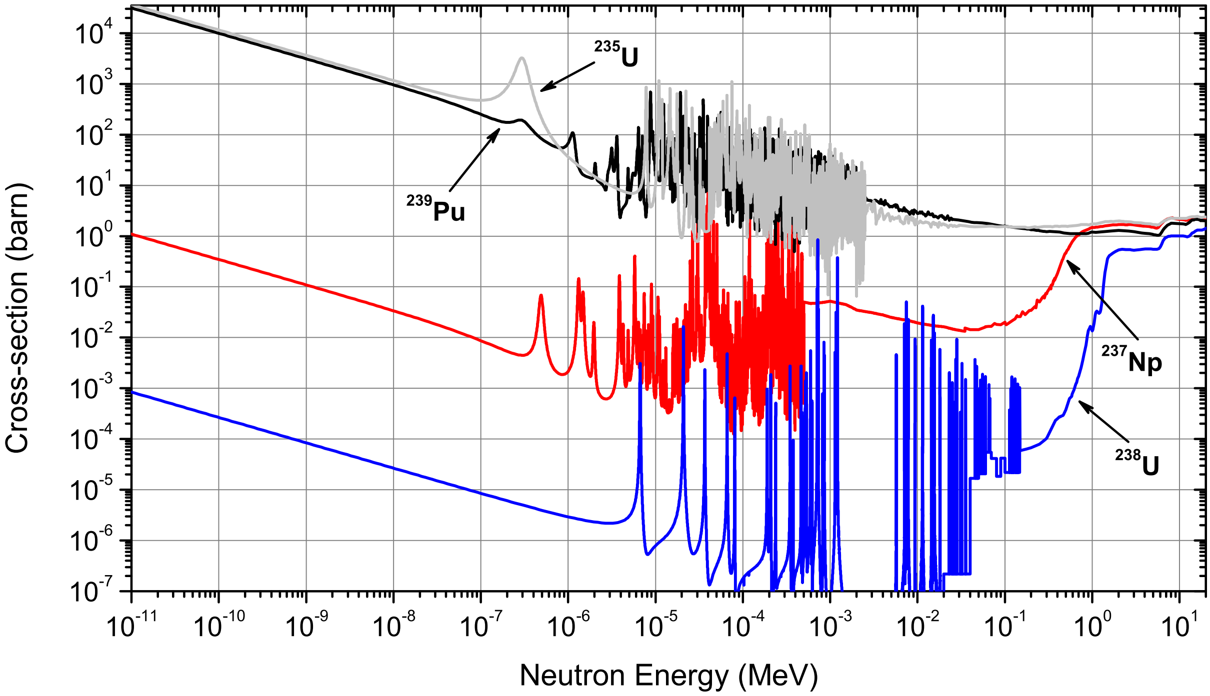

Figure 4.3: *Evaluated fission cross-sections of* ^{235}*U,* ^{239}*Pu,* ^{237}*Np and* ^{238}*U retrieved from the ENDF/B-VII.1. The cross-sections of* ^{235}*U and* ^{239}*Pu at low incident neutron energies are several orders of magnitude higher than those of* ^{237}*Np and* ^{238}*U, which exhibit a 'fission threshold' at several hundred keV. Above a few MeV, the cross-sections are quite similar.*

The fission-cross section of certain nuclei, with the exception of particular resonances, remains quite low, for reasons discussed above and increases abruptly when the incident neutron carries the necessary amount of energy to overcome the fission barrier. This generally occurs in the MeV region, or just short of it. After the so-called *fission threshold*, the cross-sections are quite similar, as can be seen in Figure 4.3.

Additional structure, seen as 'steps' in the cross section after the fission threshold are due to *multi-chance fission*. This term describes (n,xnf) channels, where the nucleus fissions after the pre-equilibrium emission of one (second-chance fission), two (third-chance fission) or more neutrons (*n*-chance fission). As the energy of the incident neutron and the excitation energy of the compound nucleus increase, so does the probability of the emission of one or more pre-equilibrium neutrons, which occurs on a time-scale much faster than fission.

4.2 The EMPIRE code

EMPIRE-III [123, 124] is a modular system of nuclear reaction codes, widely used both for theoretical cross-section calculations and data evaluation. A variety of light and heavy projectiles over a wide energy range can be selected, while the emission of neutrons, protons, α-particles etc. is automatically taken into account up to a defined 'depth' (i.e. number of emitted particles) in competition with full γ-cascades in the nuclei involved in the calculations. The code includes all major reaction mechanisms, such as compound nucleus reactions, pre-equilibrium emission and direct interaction using various optical model parameters automatically retrieved from RIPL (Reference Input Parameter Library) or chosen by the user. It also includes an optical model for fission. In the present work, version 3.1 was used (version 3.2 has since been released) with the default parameters concerning nuclear masses, ground state deformations, discrete levels, decay schemes and strength functions.

4.3 Calculation details and results

For the calculations on ^{242}Pu(n,f), exit channels with up to 3 emitted neutrons were followed, since exit channels with charged particles become important at higher energies due to the Coulomb barrier. Apart from the fission channel, the total, elastic, capture, (n,2n) and (n,3n) channels were taken into account. For each calculation, results on all the channels were compared with experimental data (where available) to determine the overall best set of parameters that reproduces all competing channels, rather than just the channel of interest – fission, in this case.

Unfortunately, no experimental data on the (n,2n) reaction are available, with the exception of a single data-point [125] at 14.7 MeV which gives an unrealistically low value and seems to be ignored by all evaluations. The evaluations themselves offer cross-section estimates with differences that exceed even 60%. No experimental data is available on the (n,3n) channel either, while evaluations show even larger discrepancies.

The level densities of the nuclei involved in the calculations were treated within the framework of the Enhanced Generalised Superfluid Model (EGSM) [126] (an extension of the GSM developed by Ignatyuk et al. [127, 128]), adjusted to experimental values of the level density parameter α and to discrete levels for $U' < U_{cr}$, and the Fermi gas model above U_{cr}. Within the GSM, the key quantities used to describe the excited nucleus are not considered as constant, but rather as functions of nuclear temperature. Furthermore, the level density function itself changes between the low- and high-energy range (the superfluid and normal phase respectively) which are defined by a critical excitation energy U_{cr}. For $U' < U_{cr}$ the nucleus is in the superfluid phase, where $\rho(U')$ is the level density of quasiparticle excitations, while for $U' \geq U_{cr}$ the nucleus is in the normal phase, where the level density follows the parametrisation of the Fermi Gas Model [129]. Improvement in the EGSM compared to the GSM lies in the more accurate treatment of high angular momenta in the spin distribution in the Fermi Gas Model, important for heavy-ion induced reactions.

Initial values for the fission barrier parameters (barrier height and width) were retrieved from the RIPL-3 library [130] and subsequently adjusted by about 5-10% in each case to better reproduce the experimental data. EMPIRE describes humps in the fission barrier either numerically (within the Hartree-Fock-Bogolyubov model) or with smoothly joined inverse parabolas to describe the entire fission path, which was the option selected in this work. In this approach, the barrier humps (h) and wells (w) are parametrised as a function of the quadrupole deformation parameter β as:

$$\begin{aligned} V_h(\beta) &= E_h - \frac{1}{2}\mu\omega_h^2(\beta-\beta_h)^2\,,\, h = 1, N_h \\ V_w(\beta) &= E_w - \frac{1}{2}\mu\omega_w^2(\beta-\beta_w)^2\,,\, w = 2, N_w \end{aligned} \tag{4.18}$$

where $N_{h(w)}$ are the number of humps (wells), $E_{h(w)}$ are the maxima and minima of the potential, $\beta_{h(w)}$ are the corresponding position along the deformation axis, $\omega_{h(w)}$ are the harmonic oscillator frequencies that define the curvature of the barrier (higher curvature means smaller width) and μ is the inertial mass parameter, approximated as $\mu \approx 0.054A^{5/3}$ MeV^{-1}. A double-humped barrier was assumed for these calculations, although the possibility to employ a triple-humped barrier has been incorporated in EMPIRE [131]; there was, however, no compelling argument to apply it in the present study.

The transmission probability through the full barrier accounts both for sub-barrier discrete levels and a continuum component for higher excitation energies. Level densities at the saddle points (or *transitional states*) then become important and need also be modelled in the calculations. Since no experimental data are available, these values are adjusted with experimental data on the final cross-section. For these calculations, it was reasonable to use the EGSM to describe the transitional state level densities for consistency, since the same model was used for the description of the normal states.

An optical model specific to ^{242}Pu (no. 411 from RIPL-3) [132] was used to describe transmission through multi-humped fission barriers, and Multi-Step Direct (MSD) and Multi-Step Compound (MSC) calculations were activated.

The results of the theoretical calculations are shown in Figure 4.4 for all studied reaction channels and compared to experimental data retrieved from EXFOR, where available. The barrier height and curvature values chosen for the inner (A) and outer (B) barrier were $V_A = 6.05$ MeV ($\hbar\omega_A = 0.80$ MeV) and $V_B = 5.45$ MeV ($\hbar\omega_B = 0.50$ MeV) for ^{243}Pu and $V_A = 6.35$ MeV ($\hbar\omega_A = 0.70$ MeV) and $V_B = 4.00$ MeV ($\hbar\omega_B = 0.60$ MeV) for ^{242}Pu. With the adjusted values for the fission barrier heights and widths, the fission cross-section is satisfactorily reproduced. At the same time, results on the (n,tot) and (n,inel) agree with experimental data, as do results on the (n,γ) channel, although only one data-point is available above 1 MeV. As mentioned earlier, no data exist on (n,xn) reactions. It seems reasonable, however, to assume that the (n,2n) cross-section is somewhat overestimated at the expense of the fission cross-section in the range of 9-12 MeV.

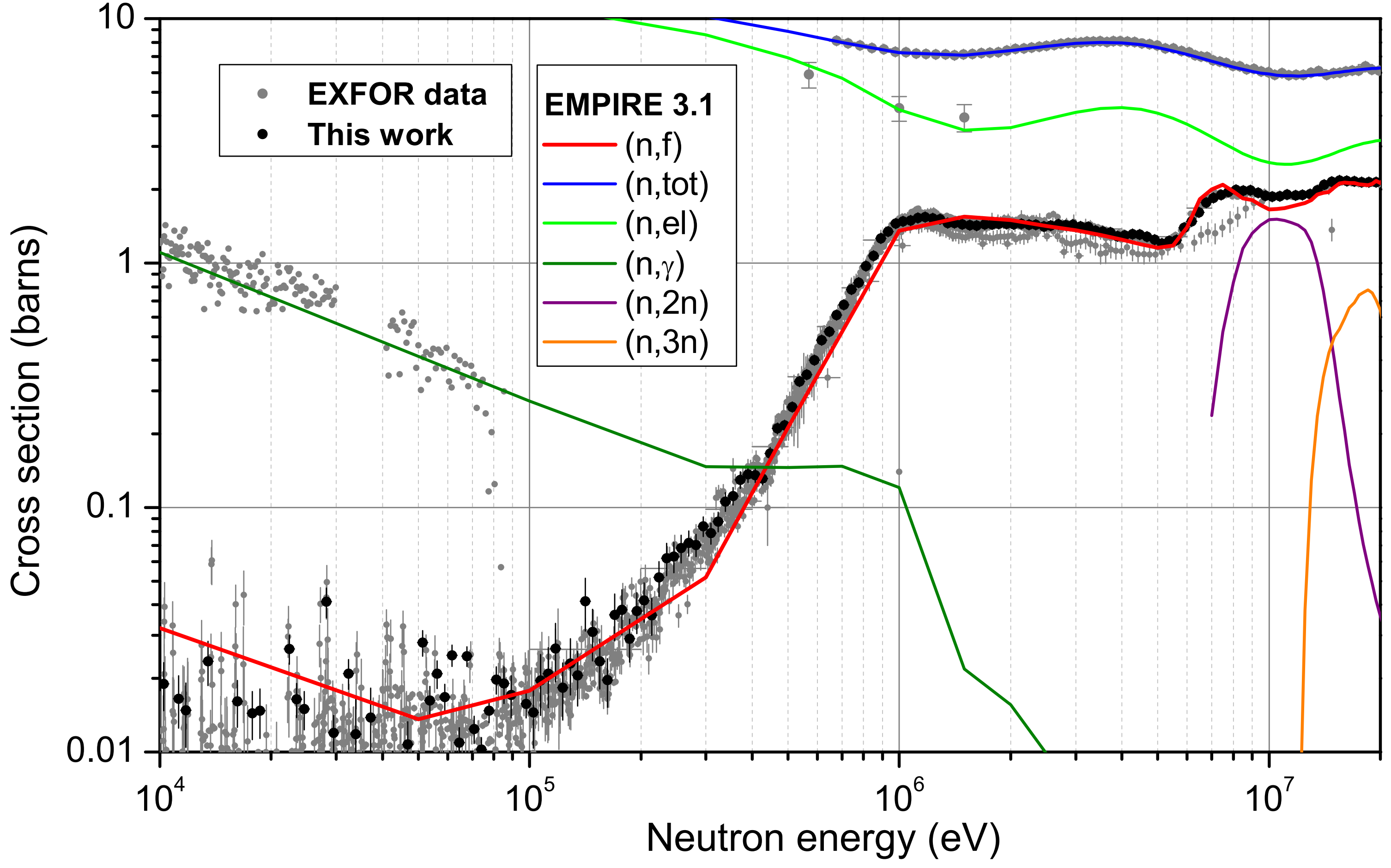

Figure 4.4: *Calculated cross-sections for fission and competing channels for* ^{242}*Pu, compared with experimental data retrieved from EXFOR, where available.*

Summary

The comprehensive theoretical description of the phenomenon of nuclear fission remains elusive over 70 years after its discovery. The development of theoretical models with satisfactory predictive capabilities relies on the availability of experimental data on various related quantities, such as fission fragment mass and energy distributions, prompt neutron emission etc. and, very importantly, neutron-induced fission cross-sections. At the same time, the development of advanced nuclear energy systems to replace ageing conventional reactors with safer, cleaner and more secure nuclear power plants also relies on the accurate knowledge of a variety of reaction cross-sections, most notably of neutron-induced fission of plutonium isotopes, minor actinides and several other isotopes found in nuclear waste. This information is not only essential for the design studies of future reactors, but also for the more efficient operation of reactors presently in use.

Within this framework, the measurement of the ^{240,242}Pu(n,f) reaction cross-sections relative to the ^{235}U(n,f) cross-section was performed at the CERN n_TOF facility in 2011-12. The experiment was performed at n_TOF's Experimental Area I (185 m neutron flight-path) using 'microbulk' Micromegas detectors and eight plutonium samples (4 $\times$ ^{240}PuO$_2$, 4 $\times$ ^{242}PuO$_2$) for a total mass of 3.1 mg of ^{240}Pu and 3.6 mg of ^{242}Pu, along with a 3.3 mg reference ^{235}U sample. Detailed Monte-Carlo simulations of the fission fragment detection setup were performed in order to estimate the detection efficiency and the correction associated with the amplitude threshold that was applied for the selection of fission events. The emission angle of fission fragments significantly affects the rise-time of the corresponding pulse and this effect was also studied in these simulations. Further detailed simulations of the neutron production, moderation and propagation were essential in determining the effective neutron moderation length and thus accurately estimating the neutron energy from the measured time-of-flight.

The analogue signals from the detectors were input into the n_TOF DAQ system based on flash-ADCs and digitised. The prompt 'γ-flash' causes an intense baseline oscillation of the detector signal which needs to be eliminated in order to obtain results above 1-2 MeV. This is achieved by means of the 'compensation' method, which consists in subtracting signals from adjacent detectors, thus cancelling the oscillation and leaving actual signals intact. The raw data were then processed off-line with a peak-search routine that stored information on each detected event, such as the signal amplitude and the measured time-of-flight. Amplitude thresholds are then applied to select fission events and reject signals caused by α-particles. The unexpected ageing observed in the detectors associated with the highly radioactive ^{240}Pu samples compromised that part of the experiment.

Once the fission events have been isolated, this information can then be used to cal-

culate the ^{242}Pu(n,f)/^{235}U(n,f) ratio and, using the evaluated ^{235}U(n,f) cross-section, the ^{242}Pu(n,f) cross-section was finally obtained. The energy range of interest was between 0.2-20 MeV, which is the range defined in the NEA Nuclear Data High Priority Request List. Nevertheless, several resonances were detected, ranging from 2.7 eV to 28.2 keV. The results above the fission threshold show general good agreement with respect to the most comprehensive and reliable past measurements, although differences of a few percent are found. Apart from the statistical uncertainty, which is between 1 and 3% above 600 keV, the main contribution to the systematic uncertainty relates to the overall normalisation of the results (detector efficiency and amplitude threshold correction).

To complement the cross-section measurement, theoretical cross-section calculations with the EMPIRE code were also performed. Satisfactory results for the fission cross-section of ^{242}Pu and for competing channels were obtained using a localised optical model potential and adjusting the height and width of the two humps of the fission barriers by around 5%. There are indications, however, that the code performs much better for even-even nuclei, such as ^{242}Pu, rather than even-odd nuclei, such as ^{237}Np.

The measurement of the ^{240}Pu(n,f) reaction cross-section remains a high-priority objective, especially in the light of recent unsuccessful attempts within the framework of the ANDES project. It is proposed to re-measure the ^{240}Pu fission cross-section, previously attempted in Experimental Area I (EAR-1), at n_TOF's new experimental area, EAR-2, taking advantage of the higher neutron flux and shorter flight-path (18 m), which will reduce the duration of the measurement, thus avoiding the degradation of the detector over the long period, observed in EAR-1. Furthermore, the shorter acquisition time in EAR-2 will substantially improve the signal-to-background ratio (since the background is related to the very large α-activity of the sample). In this manner, the two experimental obstacles encountered in the previous attempt will be eliminated.

Appendix A

Isolethargic units

It is not uncommon when confronted with the concepts of 'isolethargic units' or 'isolethargic spectra' for the first time to experience some confusion as to what is the meaning and usefulness of this representation, and how to convert quantities between isolethargic and 'natural' units. This short appendix attempts to offer a clear explanation.

Although the term 'isolethargic' finds its historical origin in neutronics, as explained later, it can be more generally used to describe any spectrum of a quantity $f(x)$ that is plotted as $df(x)/d\log x$ vs. $\log x$. This approach becomes very useful – one should say 'necessary' – when the spectrum extends over several orders of magnitude. This is usually true for a spectrum of moderated neutrons.

In our particular case, we wish to plot the neutron flux of the n_TOF beam or, in general, quantities related to the neutron energy. Since the neutron energy extends over 13 orders of magnitude, from thermal to tens of GeV, we naturally decide to plot it over $\log E$ rather than as $dn(E)/dE$ vs. E in order to observe the fine structure of the flux. It is therefore appropriate to make a variable change and plot $dn(E)/d\log E$ vs. $\log E$.

The time-integrated flux (fluence) in energy units is defined as:

$$\Phi(E) = \frac{dn(E)}{dE} = \frac{1}{E}\frac{dn(E)}{d\ln E} \tag{A.1}$$

since $d\ln E = dE/E$. We can then define the *isolethargic fluence* as:

$$\Phi_{iso}(E) \equiv \frac{dn(E)}{d\ln E} = E\cdot\Phi(E) = E\cdot\frac{dn(E)}{dE} = E\cdot\frac{\Delta n(E)}{E_{i+1}-E_i} \tag{A.2}$$

In the above equation, $dn(E)$ denotes the number of neutrons within the energy interval between E and $E + dE$ but, more generally, we can intend it to express the number of neutrons $\Delta n(E)$ in an energy bin with a lower and upper bin limit of E_i and E_{i+1} respectively. If E_{min} and E_{max} are the energy limits of the spectrum (e.g. $E_{min} = 10^{-3}$ eV and $E_{max} = 10^{10}$ eV) and N_{bins} is the number of bins in this interval (e.g. $N_{bins} = 130$), then the (logarithmic) bin width w is defined as:

$$w = \frac{\log E_{max} - \log E_{min}}{N_{bins}} \tag{A.3}$$

from which it follows that for a particular energy bin:

$$\log E_i + w = \log E_{i+1} \tag{A.4}$$

In our numerical example, $w = 0.1$, which would define a binning of 10 bins (of equal logarithmic width) per neutron energy decade between 1 meV and 10 GeV.

If we take E to be the mean energy of the bin, then (since we operate on a logarithmic scale):

$$\log E = \frac{\log E_i + \log E_{i+1}}{2} \Rightarrow E = 10^{\frac{\log E_i + \log E_{i+1}}{2}} = \sqrt{10^{\log E_i} \cdot 10^{\log E_{i+1}}} = \sqrt{E_i \cdot E_{i+1}} \tag{A.5}$$

which is the geometric mean of the bin limits. Using eq. A.4 this can be rewritten as:

$$E = \sqrt{10^{\log E_i} \cdot 10^{\log E_i + w}} = \sqrt{10^{\log E_i} \cdot 10^{\log E_i} \cdot 10^{w}} = 10^{\log E_i} \cdot \sqrt{10^{w}} \tag{A.6}$$

Similarly, the difference between the energy bin limits is:

$$\begin{aligned} E_{i+1} - E_i &= 10^{\log E_{i+1}} - 10^{\log E_i} \\ &= 10^{\log E_i + w} - 10^{\log E_i} \\ &= 10^{\log E_i} \cdot 10^{w} - 10^{\log E_i} \\ &= 10^{\log E_i} \cdot (10^{w} - 1) \end{aligned} \tag{A.7}$$

Substituting eqs. A.6 and A.7 into eq. A.2 we obtain:

$$\Phi_{iso}(E) = \frac{\sqrt{E_i \cdot E_{i+1}}}{E_{i+1} - E_i} \cdot \Delta n(E) = \frac{10^{\log E_i} \cdot \sqrt{10^{w}}}{10^{\log E_i} \cdot (10^{w} - 1)} \cdot \Delta n(E) = \frac{\sqrt{10^{w}}}{(10^{w} - 1)} \cdot \Delta n(E) \tag{A.8}$$

In practice, eq. A.8 shows how one can obtain the isolethargic flux in an energy bin by multiplying the number of neutrons in this bin by a factor that is a function of the logarithmic bin width w, and, conversely, how to calculate the number of neutrons from the isolethargic spectrum using the same factor. In other words, it is shown that the area subtended by the isolethargic curve between $\log E_i$ and $\log E_{i+1}$ is proportional to the integral of the real distribution between E_i and E_{i+1} and we have performed nothing more than a variable change, as we would in order to calculate an integral. Thus, the isolethargic spectrum can give us an immediate feeling of which energy region there are more or fewer neutrons in. Furthermore, the spectrum becomes independent of the particular energy units, since $\log E$ is dimensionless.

Historical background

As mentioned earlier and despite its more general application, the origin of the term 'isolethargic' is to be found in neutronics. Indeed, the average logarithmic energy loss ξ of a neutron after a collision with a nucleus of mass A is known as *neutron lethargy* and is given by:

$$\xi = \ln \frac{E_{ref}}{E} \tag{A.9}$$

where E_{ref} is some reference energy (it could be, for example, the initial energy of the neutron when entering the moderator in our ideal case). Lethargy is obviously dimensionless (hence the need for a reference energy) and it is clear from this equation that it increases as the neutron loses energy (justifying the use of a word that means 'deep sleep' in the original Greek). In a perfect moderator, where the capture probability is negligible, it can be shown [133] that, for $A >> 1$, lethargy is constant and equal to:

$$\xi \approx \frac{2}{A + {}^{2}\!/_{3}} \tag{A.10}$$

If neutrons lose the same amount of energy (logarithmically) in every collision, then plotting the differential neutron flux over the logarithm of the energy will yield a flat spectrum, at least up to a few hundred keV. For the system of the n_TOF spallation target and moderator, this holds largely true, as can be seen in figure 1.3.

Appendix B

Response function of a $CR - RC$ circuit

Let us assume a $CR - RC$ circuit like the one shown in figure B.1, where the two sub-circuits are connected through an ideal operational amplifier of unitary gain with infinite entrance impedance and zero exit impedance to ensure that the two parts do not interact.

We can then consider each of the two sub-circuits as a voltage divider, such as the one shown in figure B.2. In such a circuit, the output voltage is related to the input voltage and the generalised impedances Z_1 and Z_2 according to:

$$V_{out} = \frac{Z_2}{Z_1 + Z_2} \cdot V_{in} \tag{B.1}$$

Furthermore, it should be reminded that, moving from the time-domain to the s-domain, a resistance R remains unchanged, while a capacitance C becomes $\frac{1}{sC}$.

For the CR differentiator, the response function (or transfer function) $H_{CR}(s)$ will therefore be:

$$H_{CR}(s) \equiv \frac{V_{out}^{CR}(s)}{V_{in}^{CR}(s)} = \frac{R_1}{\frac{1}{sC_1} + R_1} = \frac{sR_1C_1}{1 + sR_1C_1} = \frac{\tau_1 s}{1 + \tau_1 s} \tag{B.2}$$

Similarly, for the RC integrator:

$$H_{RC}(s) \equiv \frac{V_{out}^{RC}(s)}{V_{in}^{RC}(s)} = \frac{\frac{1}{sC_2}}{R_2 + \frac{1}{sC_2}} = \frac{1}{1 + sR_2C_2} = \frac{1}{1 + \tau_2 s} \tag{B.3}$$

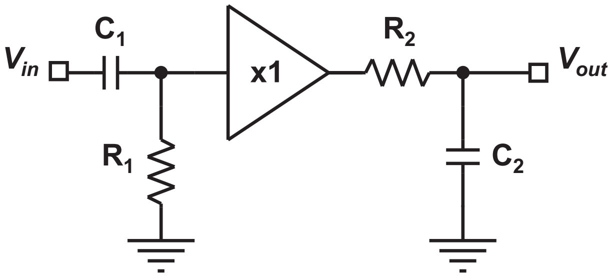

Figure B.1: *A CR – RC circuit.*

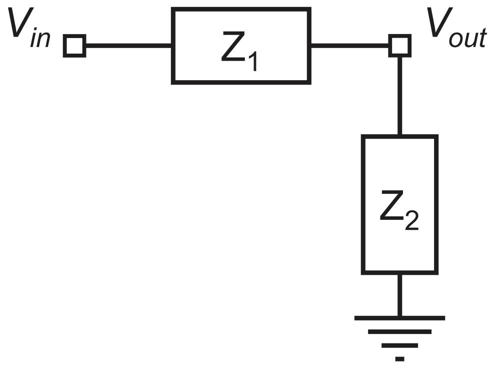

Figure B.2: *Schematic of a voltage divider, where Z_1 and Z_2 denote generalised impedances.*

From the above, it follows that the total response function $H(s)$ of the $CR - RC$ circuit will be:

$$H(s) = H_{CR}(s) \cdot H_{RC}(s) = \frac{\tau_1 s}{1 + \tau_1 s} \cdot \frac{1}{1 + \tau_2 s} \tag{B.4}$$

Given the circuit's response function, we can calculate its response to a step voltage of amplitude V_{in} at $t = 0$, knowing that the Laplace transform of the unitary step function $u(t)$ is $\mathscr{L}[u(t)] = 1/s$. We then have:

$$\begin{aligned} V_{out}(s) &= \frac{\tau_1 s}{1 + \tau_1 s} \cdot \frac{1}{1 + \tau_2 s} \cdot \frac{1}{s} = \frac{\tau_1}{(1 + \tau_1 s)(1 + \tau_2 s)} = \frac{1}{\left(s + \frac{1}{\tau_1}\right)(1 + \tau_2 s)} = \\ &= \frac{1}{\tau_2 \left(s + \frac{1}{\tau_1}\right)\left(s + \frac{1}{\tau_2}\right)} = \frac{1}{\tau_2}\left(\frac{a_1}{s + \frac{1}{\tau_1}} + \frac{a_2}{s + \frac{1}{\tau_2}}\right) \end{aligned} \tag{B.5}$$

The coefficients a_1 and a_2 for the partial fraction expansion can be calculated as:

$$a_1 = \lim_{s \to -\frac{1}{\tau_1}} \frac{s + \frac{1}{\tau_1}}{\left(s + \frac{1}{\tau_1}\right)\left(s + \frac{1}{\tau_2}\right)} = \lim_{s \to -\frac{1}{\tau_1}} \frac{1}{s + \frac{1}{\tau_2}} = \frac{1}{\frac{1}{\tau_1} - \frac{1}{\tau_2}} = \frac{\tau_1 \tau_2}{\tau_1 - \tau_2} \tag{B.6}$$

$$a_2 = \lim_{s \to -\frac{1}{\tau_2}} \frac{s + \frac{1}{\tau_2}}{\left(s + \frac{1}{\tau_1}\right)\left(s + \frac{1}{\tau_2}\right)} = \cdots = \frac{\tau_1 \tau_2}{\tau_2 - \tau_1} = -a_1 \tag{B.7}$$

Substituting in eq. B.5 we obtain:

$$V_{out}(s) = \frac{a_1}{\tau_2}\left(\frac{1}{s + \frac{1}{\tau_1}} + \frac{1}{s + \frac{1}{\tau_2}}\right) = \frac{\tau_1}{\tau_1 - \tau_2}\left(\frac{1}{s + \frac{1}{\tau_1}} + \frac{1}{s + \frac{1}{\tau_2}}\right) \tag{B.8}$$

Applying the inverse Laplace transform to eq. B.8 and since $\mathscr{L}^{-1}[\frac{1}{s+a}] = e^{at}$, we finally obtain the result of eq. 2.5:

$$V_{out}(t) = V_{in} \cdot \frac{\tau_1}{\tau_1 - \tau_2} \cdot \left(e^{-\frac{t}{\tau_1}} - e^{-\frac{t}{\tau_2}}\right) \tag{B.9}$$

References

[1] *ANDES: Accurate Nuclear Data for Nuclear Energy Sustainability (EURATOM FP7-249671)*, www.andes-nd.eu

[2] *ERINDA: European Research Infrastructures for Nuclear Data Applications (EURATOM FP7-269499)*, www.erinda.org

[3] Population Division of the Department of Economic and Social Affairs of the United Nations Secretariat, *World Population Prospects: The 2012 Revision*, esa.un.org/wpp

[4] The World Bank, *World Development Indicators*, data.worldbank.org/data-catalog/world-development-indicators

[5] The Intergovernmental Panel on Climate Change (IPCC), *Fifth Assessment Report (AR5)*, www.ipcc.ch/report/ar5/

[6] International Energy Agency (IEA), *Key World Energy Statistics (2013)*, www.iea.org/publications/freepublications/publication/KeyWorld2013.pdf

[7] Population Division of the Department of Economic and Social Affairs of the United Nations Secretariat, *World Urbanisation Prospects: The 2011 Revision*, esa.un.org/unup/

[8] *Generation-IV International Forum*, www.gen-4.org

[9] US Dep. of Energy, Nuclear Energy Research Advisory Committee and Generation-IV International Forum, *Technology Roadmap for Generation IV Nuclear Energy Systems* (2002), www.gen-4.org/gif/upload/docs/application/pdf/2013-09/genivroadmap2002.pdf

[10] Nuclear Energy Agency on bahalf of the Generation-IV International Forum, *Technology Roadmap Update for Generation IV Nuclear Energy Systems* (2014), www.gen-4.org/gif/upload/docs/application/pdf/2014-03/gif-tru2014.pdf

[11] *NEA Nuclear Data High Priority Request List*, www.nea.fr/html/dbdata/hprl

[12] *OECD/NEA WPEC Subgroup 26 Final Report: Uncertainty and Target Accuracy Assessment for Innovative Systems Using Recent Covariance Data Evaluations*, www.nea.fr/html/science/wpec/volume26/volume26.pdf

[13] *Experimental Nuclear Reaction Data (EXFOR)*, www-nds.iaea.org/exfor/exfor.htm

[14] O. Schwerer, *EXFOR Formats Description for Users (EXFOR Basics)*, Tech. Rep. IAEA-NDS-206, IAEA, Vienna (2008), www-nds.iaea.org/publications/iaea-nds/iaea-nds-0206.pdf

[15] *Evaluated Nuclear Data File (ENDF)*, www-nds.iaea.org/exfor/endf.htm

[16] M. Chadwick et al., *ENDF/B-VII.1 Nuclear Data for Science and Technology: Cross Sections, Covariances, Fission Product Yields and Decay Data*, Nucl. Data Sheets **112**(12), (2011) pp. 2887 – 2996, DOI: http://dx.doi.org/10.1016/j.nds.2011.11.002

[17] A. Santamarina et al., *The JEFF-3.1.1 Nuclear Data Library*, Tech. Rep. NEA No. 6807, NEA (2009), www.oecd-nea.org/dbdata/nds_jefreports/jefreport-22/nea6807-jeff22.pdf

[18] K. Shibata et al., *JENDL-4.0: A New Library for Nuclear Science and Engineering*, Journal of Nuclear Science and Technology **48**(1), (2011) pp. 1–30, DOI: 10.1080/18811248.2011.9711675

[19] H. Lemmel and P. McLaughlin, *BROND-2.2 Russian Evaluated Neutron Reaction Data Library Summary Documentation*, Tech. Rep. IAEA-NDS-90, IAEA, Vienna (1994), www-nds.iaea.org/publications/iaea-nds/iaea-nds-0090.pdf

[20] Z. Ge et al., *The Updated Version of Chinese Evaluated Nuclear Data Library (CENDL-3.1)*, J. Korean Phys. Soc. **59**(2), (2011) p. 1052, DOI: 10.3938/jkps.59.1052

[21] OECD/NEA Working Party on the Physics of Plutonium Fuels and Innovative Fuel Cycles (WPPR), *Plutonium Management in the Medium Term*, Tech. Rep. NEA-4451, OECD/NEA (2003), www.oecd-nea.org/science/docs/pubs/nea4451-plutonium.pdf

[22] Varii, *Fission cross section measurements for ^{240}Pu, ^{242}Pu: Deliverable 1.5 of the ANDES project*, European Commission, Joint Research Centre, Belgium (2013), DOI: 10.2787/81004

[23] A. Plompen, *Minor Actinides, Major Challenges: the Needs for and Benefits of International Collaboration*, Nucl. Data Sheets Proceedings of the Nuclear Data Conference

[24] C. Rubbia et al., *Conceptual design of a fast neutron operated high power energy amplifier*, Tech. Rep. CERN-AT-95-44 ET, CERN, Geneva (1995), cds.cern.ch/record/289551

[25] C. Rubbia, *A high gain energy amplifier operated with fast neutrons*, AIP Conf. Proc. **346**(1), (1995) pp. 44–53, DOI: 10.1063/1.49069

[26] A. Abánades et al., *Results from the TARC experiment: spallation neutron phenomenology in lead and neutron-driven nuclear transmutation by adiabatic resonance crossing*, Nucl. Instrum. Meth. A **478**(3), (2002) pp. 577 – 730, DOI: 10.1016/S0168-9002(01)00789-6

[27] J.-P. Revol, *The TARC experiment (PS211): neutron-driven nuclear transmutation by adiabatic resonance crossing*, CERN, Geneva (1999), DOI: 10.5170/CERN-1999-011

[28] C. Rubbia, *Resonance enhanced neutron captures for element activation and waste transmutation*, Tech. Rep. CERN-LHC-97-004-EET, CERN, Geneva (1997), cds.cern.ch/record/329843

[29] C. Rubbia et al., *A high resolution spallation driven facility at the CERN-PS to measure neutron cross sections in the interval from 1 eV to 250 MeV*, Tech. Rep. CERN-LHC-98-002-EET, CERN, Geneva (1998), cds.cern.ch/record/357112

[30] U. Abbondanno, *CERN n_TOF Facility: Performance Report*, Tech. Rep. CERN-SL-2002-053 ECT, CERN, Geneva (2002)

[31] C. Guerrero et al., *Performance of the neutron time-of-flight facility n_TOF at CERN*, Eur. Phys. J. A **49**(2), (2013) pp. 1–15, DOI: 10.1140/epja/i2013-13027-6

[32] E. Berthoumieux, *The neutron Time-Of-Flight facility, n_TOF, at CERN (I): Technical Description*, cds.cern.ch/record/1514680

[33] E. Chiaveri and the n_TOF Collaboration, *Proposal for n_TOF Experimental Area 2*, Tech. Rep. CERN-INTC-2012-029. INTC-O-015, CERN, Geneva (2012), cds.cern.ch/record/1411635

[34] A. Ferrari, C. Rubbia and V. Vlachoudis, *A comprehensive study of the n_TOF background*, Tech. Rep. SL-Note-2001-036-EET, CERN, Geneva (2002), cds.cern.ch/record/702671

[35] L. Zanini et al., *Study of the background in the measuring station at the n_TOF facility at CERN: sources and solutions*, Tech. Rep. SL-Note-2001-046-EET, CERN, Geneva (2001), cds.cern.ch/record/702679

[36] V. Vlachoudis et al., *n_TOF facility Safety File*, edms.cern.ch/document/934369/0.13, CERN EDMS No. 934369

[37] G. Lorusso et al., *Time–energy relation of the n_TOF neutron beam: energy standards revisited*, Nucl. Instrum. Meth. A **532**(3), (2004) pp. 622 – 630, DOI: 10.1016/j.nima.2004.04.247

[38] Y. Giomataris et al., *MICROMEGAS: a high-granularity position-sensitive gaseous detector for high particle-flux environments*, Nucl. Instrum. Meth. A **376**(1), (1996) pp. 29 – 35, DOI: 10.1016/0168-9002(96)00175-1

[39] Y. Giomataris, *Development and prospects of the new gaseous detector "Micromegas"*, Nucl. Instrum. Meth. A **419**(2–3), (1998) pp. 239 – 250, DOI: 10.1016/S0168-9002(98)00865-1

[40] A. Oed, *Micro pattern structures for gas detectors*, Nucl. Instrum. Meth. A **471**(1–2), (2001) pp. 109 – 114, DOI: 10.1016/S0168-9002(01)00966-4

[41] F. Sauli, *Micro-pattern gas detectors*, Nucl. Instrum. Meth. A **477**(1–3), (2002) pp. 1 – 7, DOI: 10.1016/S0168-9002(01)01903-9, 5th Int. Conf. on Position-Sensitive Detectors

[42] L. Shekhtman, *Micro-pattern gaseous detectors*, Nucl. Instrum. Meth. A **494**(1–3), (2002) pp. 128 – 141, DOI: 10.1016/S0168-9002(02)01456-0, Proceedings of the 8th International Conference on Instrumentation for Colliding Beam Physics

[43] M. Hoch, *Trends and new developments in gaseous detectors*, Nucl. Instrum. Meth. A **535**(1–2), (2004) pp. 1 – 15, DOI: 10.1016/j.nima.2004.07.265, Proceedings of the 10th International Vienna Conference on Instrumentation

[44] I. Giomataris, *MICROMEGAS: results and prospects*, ICFA Instrum. Bul. **19**, www.slac.stanford.edu/pubs/icfa/fall99/paper1/paper1a.html

[45] J. Pancin, *Détection de neutrons avec un détecteur de type Micromegas: de la Physique nucléaire à l'imagerie*, Ph.D. thesis, Saclay, SPhT (2004), cds.cern.ch/record/1474098

[46] S. Andriamonje et al., *Development and performance of Microbulk Micromegas detectors*, J. Instrum. **5**(02), (2010) p. P02001, DOI: 10.1088/1748-0221/5/02/P02001

[47] S. Andriamonje et al., *A Transparent Detector for n_TOF Neutron Beam Monitoring*, J. Korean Phys. Soc. **59**(23), (2011) p. 1597, DOI: 10.3938/jkps.59.1597

[48] M. Zabetakis, *Flammability characteristics of combustible gases and vapors*, Tech. Rep. Bulletin 627, Bureau of Mines, U.S. Dept. of the Interior, Washington, D.C. (1965), oai.dtic.mil/oai/oai?verb=getRecord&metadataPrefix=html&identifier=AD0701576

[49] G. Sibbens et al., *Preparation of* ^{240}*Pu and* ^{242}*Pu targets to improve cross-section measurements for advanced reactors and fuel cycles*, J. Radioanal. Nucl. Ch. **299**, (2013) pp. 1–6, DOI: 10.1007/s10967-013-2668-7

[50] C. Guerrero et al., *Safety manual for special use of plutonium radioactive sources for the MGAS detector at the CERN n_TOF facility* (2011), edms.cern.ch/document/1149614, CERN EDMS No. 1149614

[51] U. Abbondanno et al., *The data acquisition system of the neutron time-of-flight facility n_TOF at CERN*, Nucl. Instrum. Meth. A **538**(1–3), (2005) pp. 692 – 702, DOI: 10.1016/j.nima.2004.09.002

[52] *AGILENT digitisers website*, www.home.agilent.com/en/pc-1881370/pci-pcie-cpci-vme-digitizers

[53] *CASTOR: CERN Advanced STORage manager*, castor.web.cern.ch

[54] A. Ferrari et al., *FLUKA: A multi-particle transport code (program version 2005)*, CERN, Geneva (2005), DOI: 10.5170/CERN-2005-010

[55] G. Battistoni et al., *The FLUKA code: description and benchmarking*, in M. Albrow and R. Raja, eds., *Proceedings of the Hadronic Shower Simulation Workshop, Fermilab 6-8 September 2006, AIP Conference Proceeding*, AIP, Fermilab, USA (2007), vol. 896, (pp. 31–49), DOI: 10.1063/1.2720455

[56] L. Waters et al., *The MCNPX Monte Carlo radiation transport code*, in M. Albrow and R. Raja, eds., *Proceedings of the Hadronic Shower Simulation Workshop, Fermilab 6-8 September 2006, AIP Conference Proceeding*, AIP, Fermilab, USA (2007), vol. 896, (pp. 81–90), DOI: 10.1063/1.2720459

[57] *FLUKA-2011 Manual, Chapter 10 'Low-energy neutrons in FLUKA'*, www.fluka.org/content/manuals/fluka2011.manual

[58] M. Barbagallo et al., *High-accuracy determination of the neutron flux at n_TOF*, Eur. Phys. J. A **49**(12), (2013) pp. 1–11, DOI: 10.1140/epja/i2013-13156-x

[59] F. Belloni, Nucl. Data Sheets **119**, proceedings of the 2013 International Conference on Nuclear Data for Science and Technology (ND 2013)

[60] V. Vlachoudis, *FLAIR: A powerful but user friendly graphical interface for FLUKA*, in *Proceedings of the International Conference on Mathematics, Computational Methods and Reactor Physics*, American Nuclear Society, Saratoga Springs, New York (2009), (pp. 790–800), www.fluka.org/flair/Flair_MC2009.pdf

[61] *GEF code website*, www.cenbg.in2p3.fr/-GEF-

[62] K.-H. Schmidt and B. Jurado, *General model description of fission observables*, www.cenbg.in2p3.fr/IMG/pdf_final_efnudat_report2.pdf

[63] K.-H. Schmidt and B. Jurado, *Prompt-neutron and prompt-gamma emission from a general description of the fission process*, www.cenbg.in2p3.fr/IMG/pdf_jef_doc_1423.pdf

[64] *Stopping powers and ranges for protons and alpha particles*, ICRU, Washington, DC (1993)

[65] G. Knoll, *Radiation Detection and Measurement*, Wiley, 4th ed. (2010)

[66] L. G. H. Huxley and R. W. Crompton, *The diffusion and drift of electrons in gases*, Wiley series in plasma physics, Wiley, New York, NY (1974)

[67] R. Veenhof, *GARFIELD: Simulation of Gas Detectors*, garfield.web.cern.ch

[68] *ROOT: An Object-Oriented Data Analysis Framework*, root.cern.ch

[69] N. Colonna, M. Calviani and A. Tsinganis, *A software compensation technique for fission measurements at spallation neutron sources*, under preparation

[70] M. Mariscotti, *A method for automatic identification of peaks in the presence of background and its application to spectrum analysis*, Nucl. Instrum. Meth. **50**(2), (1967) pp. 309 – 320, DOI: 10.1016/0029-554X(67)90058-4

[71] A. Tsinganis et al., *Measurement of the ^{240}Pu(n,f) reaction cross-section at the CERN n_TOF facility EAR-2*, Tech. Rep. CERN-INTC-2014-051. INTC-P-418, CERN, Geneva (2014), cds.cern.ch/record/1706708

[72] P. Salvador-Castiñeira et al., *Highly accurate measurements of the spontaneous fission half-life of ^{240,242}Pu*, Phys. Rev. C **88**, (2013) p. 064611, DOI: 10.1103/PhysRevC.88.064611

[73] J. Ziegler, *SRIM-2003*, Nucl. Instrum. Meth. B **219–220**(0), (2004) pp. 1027 – 1036, DOI: 10.1016/j.nimb.2004.01.208

[74] J. Ziegler, *Stopping and Range of Ions in Matter, SRIM 2013*, www.srim.org

[75] J. Meadows and C. Budtz-Jørgensen, *Fission Fragment Angular Distributions and Total Kinetic Energies for 235U(n,f) from 0.18 to 8.83 MeV*, in K. Böckhoff, ed., *Nuclear Data for Science and Technology*, Springer Netherlands (1983), (pp. 740–743), DOI: 10.1007/978-94-009-7099-1_159

[76] C. Straede, C. Budtz-Jørgensen and H.-H. Knitter, *^{235}U(n,f) Fragment mass-, kinetic energy- and angular distributions for incident neutron energies between thermal and 6 MeV*, Nuclear Physics A **462**(1), (1987) pp. 85 – 108, DOI: 10.1016/0375-9474(87)90381-2

[77] J. Simmons, R. Perkins and R. Henkel, *Anisotropy of Fragments in the Neutron-Induced Fission of Pu-240, Pu-242, and Pu-241*, Phys. Rev. **137**, (1965) pp. B809–B813, DOI: 10.1103/PhysRev.137.B809

[78] Varii, *International Evaluation of Neutron Cross-Section Standards*, IAEA, Vienna (2007), www-pub.iaea.org/MTCD/Publications/PDF/Pub1291_web.pdf

[79] E. Fomushkin and E. Gutnikova, *'Cross sections and angular distributions of fragments in the fission of ^{238}Pu, ^{242}Pu, and ^{241}Am by neutrons of energy 0.45–3.6 MeV*, Sov. J. Nucl. Phys. **10**, (1970) p. 529

[80] J. W. Meadows, *The Fission Cross Sections of Plutonium-239 and Plutonium-242 Relative to Uranium-235 from 0.1 to 10 MeV*, Nucl. Sci. Eng. **68**(3), (1978) pp. 360–363, www.ans.org/pubs/journals/nse/a_27315

[81] J. W. Behrens, R. S. Newbury and J. W. Magana, *Measurements of the Neutron-Induced Fission Cross Sections of ^{240}Pu, ^{242}Pu, and ^{244}Pu Relative to ^{235}U from 0.1 to 30 MeV*, Nucl. Sci. Eng. **66**(3), (1978) pp. 433–441, www.ans.org/pubs/journals/nse/a_27227

[82] V. Kupriyanov et al., *Measurement of the* ^{240}*Pu/*^{235}*U and* ^{242}*Pu/*^{235}*U fission cross-section ratios for 0.127–7.4 MeV neutrons*, Sov. Atom. Energy **46**(1), (1979) pp. 35–39, DOI: 10.1007/BF01119949

[83] F. Manabe et al., *Measurements of neutron induced fission cross section ratios of* ^{232}*Th,* ^{233}*U,* ^{234}*U,* ^{236}*U,* ^{238}*U,* ^{237}*Np,* ^{242}*Pu and* ^{243}*Am Relative to* ^{235}*U around 14 MeV*, Tech. Rep. of the Tohoku University **52**(2), (1988) pp. 97–126

[84] J. Meadows, *The fission cross sections of* ^{230}*Th,* ^{232}*Th,* ^{233}*U,* ^{234}*U,* ^{236}*U,* ^{238}*U,* ^{237}*Np,* ^{239}*Pu and* ^{242}*Pu relative to* ^{235}*U at 14.74 MeV neutron energy*, Ann. Nucl. Energy **15**(8), (1988) pp. 421 – 429, DOI: 10.1016/0306-4549(88)90038-2

[85] T. Iwasaki et al., *Measurement of Fast Neutron Induced Fission Cross Section Ratios of Pu-240 and Pu-242 Relative to U-235*, Nucl. Sci. Tech. **27**(10), (1990) pp. 885–898, DOI: 10.1080/18811248.1990.9731269

[86] P. Staples and K. Morley, *Neutron-Induced Fission Cross-Section Ratios for* ^{239}*Pu,* ^{240}*Pu,* ^{242}*Pu, and* ^{244}*Pu Relative to* ^{235}*U from 0.5 to 400 MeV*, Nucl. Sci. Eng. **129**(2), (1998) pp. 149–163, www.ans.org/pubs/journals/nse/a_1969

[87] D. K. Butler, *Fission Cross Section of Plutonium-242*, Phys. Rev. **117**, (1960) pp. 1305–1306, DOI: 10.1103/PhysRev.117.1305

[88] G. James, *Fission components in* ^{242}*Pu resonances*, Nucl. Phys. A **123**(1), (1969) pp. 24–26, DOI: 10.1016/0375-9474(69)90886-0

[89] G. F. Auchampaugh, J. A. Farrell and D. W. Bergen, *Neutron-induced fission cross sections of* ^{242}*Pu and* ^{244}*Pu*, Nucl. Phys. A **171**(1), (1971) pp. 31 – 43, DOI: 10.1016/0375-9474(71)90360-5

[90] D. W. Bergen and R. R. Fullwood, *Neutron-induced fission cross section of* ^{242}*Pu*, Nucl. Phys. A **163**(2), (1971) pp. 577 – 582, DOI: 10.1016/0375-9474(71)90510-0

[91] N. A. Khan et al., *A new approach to measure reaction parameters in the 14.8 meV neutron induced fission of* ^{240}*Pu and* ^{241}*Pu*, Nucl. Instrum. Meth. **173**(1), (1980) pp. 137 – 142, DOI: 10.1016/0029-554X(80)90578-9

[92] M. Cance and G. Grenier, *Absolute Measurement of the* ^{240}*Pu(n,f),* ^{242}*Pu(n,f) and* ^{237}*Np(n,f) Cross Sections at 2.5 MeV Incoming Neutron Energy*, in *Conf. on Nucl. Data for Sci. and Technol.*, Antwerp, Belgium (1982), (p. 51)

[93] I. Alkhazov et al., *Absolute measurements of the fission ccross sections for some heavy isotopes by the neutrons with energies 2.6, 8.4, 14.7 MeV*, in *Proc. of the 3rd All-Union Conference on the Neutron Radiation Metrology at Reactors and Accelerators*, Moscow (1983), vol. 2, (p. 201)

[94] H. Weigmann, J. Wartena and C. Bürkholz, *Neutron-induced fission cross section of* ^{242}*Pu*, Nucl. Phys. A **438**(2), (1985) pp. 333 – 353, DOI: 10.1016/0375-9474(85)90379-3

[95] K. Gul et al., *Measurements of Neutron Fission Cross Sections of* ^{237}*Np,* ^{240}*Pu,* ^{241}*Pu,* ^{242}*Pu,* ^{244}*Pu, and* ^{241}*Am at 14.7 MeV*, Nucl. Sci. Eng. **94**(1), (1986) pp. 42–45

[96] F. Tovesson et al., *Neutron induced fission of* ^{240,242}*Pu from 1 eV to 200 MeV*, Phys. Rev. C **79**, (2009) p. 014613, DOI: 10.1103/PhysRevC.79.014613

[97] C. Wagemans, *The nuclear fission process*, CRC Press, Boca Raton, FL (1991)

[98] R. Vandenbosch and J. R. Huizenga, *Nuclear fission*, Academic Press, New York, NY (1973)

[99] A. Cole, *Statistical Models for Nuclear Decay: From Evaporation to Vaporization*, Series in Fundamental and Applied Nuclear Physics, Taylor & Francis (2000)

[100] H. Krappe and K. Pomorski, *Theory of nuclear fission*, Lecture Notes in Physics, Springer Berlin Heidelberg, Berlin (2012), DOI: 10.1007/978-3-642-23515-3

[101] J. Chadwick, *Possible Existence of a Neutron*, Nature **129**, (1932) pp. 312–312, DOI: 10.1038/129312a0

[102] J. Chadwick, *The Existence of a Neutron*, P. Roy. Soc. A - Math. Phy. **136**(830), (1932) pp. 692–708, DOI: 10.1098/rspa.1932.0112

[103] E. Fermi, *Radioactivity Induced by Neutron Bombardment*, Nature **133**, (1934) pp. 757–757, DOI: 10.1038/133757a0

[104] E. Fermi et al., *Artificial Radioactivity Produced by Neutron Bombardment*, P. Roy. Soc. A - Math. Phy. **146**(857), (1934) pp. 483–500, DOI: 10.1098/rspa.1934.0168

[105] O. Hahn and F. Strassmann, *Über die Entstehung von Radiumisotopen aus Uran durch Bestrahlen mit schnellen und verlangsamten Neutronen*, Naturwissenschaften **26**(46), (1938) pp. 755–756, DOI: 10.1007/BF01774197

[106] O. Hahn and F. Strassmann, *Über den Nachweis und das Verhalten der bei der Bestrahlung des Urans mittels Neutronen entstehenden Erdalkalimetalle*, Naturwissenschaften **27**(1), (1939) pp. 11–15, DOI: 10.1007/BF01488241

[107] L. Meitner and O. Frisch, *Disintegration of Uranium by Neutrons: a New Type of Nuclear Reaction*, Nature **143**, (1939) pp. 239–240, DOI: 10.1038/143239a0

[108] L. Meitner and O. Frisch, *Products of the Fission of the Uranium Nucleus*, Nature **143**, (1939) pp. 471–472, DOI: 10.1038/143471a0

[109] O. Frisch, *Physical Evidence for the Division of Heavy Nuclei under Neutron Bombardment*, Nature **143**, (1939) pp. 276–276, DOI: 10.1038/143276a0

[110] F. Joliot, *Preuve expérimentale de la rupture explosive des noyaux d'uranium et de thorium sous l'action des neutrons*, Comptes Rendus de l'Académie des Sciences **208**, (1939) pp. 341–343, gallica.bnf.fr/ark:/12148/bpt6k3160g/f323.image.langFR

[111] E. Amaldi, *From the discovery of the neutron to the discovery of nuclear fission*, North-Holland, Amsterdam (1984)

[112] L. A. Turner, *Nuclear Fission*, Rev. Mod. Phys. **12**, (1940) pp. 1–29, DOI: 10.1103/RevModPhys.12.1

[113] N. Bohr and J. A. Wheeler, *The Mechanism of Nuclear Fission*, Phys. Rev. **56**, (1939) pp. 426–450, DOI: 10.1103/PhysRev.56.426

[114] E. Rutherford et al., *Discussion on the Structure of Atomic Nuclei*, P. Roy. Soc. A - Math. Phy. **123**(792), (1929) pp. 373–390, DOI: 10.1098/rspa.1929.0074

[115] G. Gamow, *Mass Defect Curve and Nuclear Constitution*, P. Roy. Soc. A - Math. Phy. **126**(803), (1930) pp. 632–644, DOI: 10.1098/rspa.1930.0032

[116] V. Strutinsky, *Shell effects in nuclear masses and deformation energies*, Nucl. Phys. A **95**(2), (1967) pp. 420 – 442, DOI: 10.1016/0375-9474(67)90510-6

[117] S. Bjørnholm and J. E. Lynn, *The double-humped fission barrier*, Rev. Mod. Phys. **52**, (1980) pp. 725–931, DOI: 10.1103/RevModPhys.52.725

[118] P. Möller et al., *Nuclear fission modes and fragment mass asymmetries in a five-dimensional deformation space*, Nature **409**, (2001) pp. 785–790, DOI: 10.1038/35057204

[119] P. Möller et al., *Heavy-element fission barriers*, Phys. Rev. C **79**, (2009) p. 064304, DOI: 10.1103/PhysRevC.79.064304

[120] U. Brosa, S. Grossmann and A. Müller, *Nuclear scission*, Phys. Rep. **197**(4), (1990) pp. 167 – 262, DOI: 10.1016/0370-1573(90)90114-H

[121] M. Duijvestijn, A. Koning and F.-J. Hambsch, *Mass distributions in nucleon-induced fission at intermediate energies*, Phys. Rev. C **64**, (2001) p. 014607, DOI: 10.1103/PhysRevC.64.014607

[122] M. P. and N. J.R., *Calculation of fission barriers*, in *Proceedings of the Third IAEA Symposium on the Physics and Chemistry of Fission, Rochester, New York, 13 - 17 August 1973*, Vienna (1974), vol. 1, (p. 103)

[123] *EMPIRE Nuclear Reaction Model Code*, www.nndc.bnl.gov/empire/main.html

[124] M. Herman et al., *EMPIRE: Nuclear Reaction Model Code System for Data Evaluation*, Nucl. Data Sheets **108**, (2007) p. 2655, DOI: 10.1016/j.nds.2007.11.003

[125] Y. Gangrskiy, B. Markov and T.Nagy, *Measurement of cross-sections of production of spontaneously-fissionable isomers in reaction with neutrons*, Proc. All-Union Conf. on Neutron Phys., Kiev, 9-13 June 1975 **5**, (1975) p. 245

[126] A. D'Arrigo et al., *Semi-empirical determination of the shell correction temperature and spin dependence by means of nuclear fission*, J. Phys. G Nucl. Partic. **20**(2), (1994) p. 365, DOI: 10.1088/0954-3899/20/2/015

[127] A. Ignatyuk, K. Istekov and G. Smirenkin, *Role of collective effects in the systematics of nuclear level densities*, Sov. J. Nucl. Phys. **29**, (1979) p. 450

[128] A. V. Ignatyuk et al., *Density of discrete levels in Sn116*, Phys. Rev. C **47**, (1993) pp. 1504–1513, DOI: 10.1103/PhysRevC.47.1504

[129] H. Bethe, *Nuclear Physics B. Nuclear Dynamics, Theoretical*, Rev. Mod. Phys. **9**, (1937) pp. 69–244, DOI: 10.1103/RevModPhys.9.69, link.aps.org/doi/10.1103/RevModPhys.9.69

[130] R. Capote et al., *RIPL – Reference Input Parameter Library for Calculation of Nuclear Reactions and Nuclear Data Evaluations*, Nucl. Data Sheets **110**(12), (2009) pp. 3107 – 3214, DOI: 10.1016/j.nds.2009.10.004

[131] M. Sin et al., *Fission of light actinides: ^{232}Th(n,f) and ^{231}Pa(n,f) reactions*, Phys. Rev. C **74**, (2006) p. 014608, DOI: 10.1103/PhysRevC.74.014608

[132] C. Lagrange, *Results of Coupled Channels Calculations for the Neutrons Cross Sections of a set of Actinide Nuclei*, Tech. Rep. INDC(FR)-56 / NEANDC(E)228, Commissariat à l'énergie atomique (CEA) (1986), www-nds.iaea.org/publications/indc/indc-fr-0056/

[133] K. Beckhurts and K. Wirtz, *Neutron Physics*, Springer-Verlag, New York (1964)